

Study of correlation between flow harmonics in
Heavy Ion collisions at $\sqrt{s_{NN}} = 2.76$ TeV with
ALICE at LHC

Myunggeun Song

The Graduate School
Yonsei University
Physics Department

Study of correlation between flow harmonics in
Heavy Ion collisions at $\sqrt{s_{NN}} = 2.76$ TeV with
ALICE at LHC

A Ph.D Thesis
Submitted to the Physics Department
and the Graduate School of Yonsei University
in partial fulfillment of the
requirements for the degree of

Myunggeun Song

November 11, 2016

Contents

List of Figures	iv
List of Tables	xi
Abstract	xi
Chapter 1. Introduction	1
1.1 Quantum Chromo Dynamics (QCD)	1
1.2 Quark Gluon Plasma (QGP).....	2
1.3 Heavy ion collision.....	3
1.4 Flow	6
1.4.1 Event Plane method.....	13
1.4.2 Scalar product method	16
1.4.3 Cumulants method.....	18
1.5 Jet quenching	23
1.6 Correlation between flow harmonics	26
Chapter 2. Experimental setup	30
2.1 Large Hadron Collider	30
2.2 The ALICE experiment	32
2.2.1 ITS	33
2.2.2 TPC.....	34
2.2.3 VZERO	35
2.2.4 Other detectors	38
2.2.5 Analysis Framework	39

Chapter 3. Data analysis	41
3.1 Data selection.....	41
3.1.1 Default cuts and settings	41
3.1.2 Data QA.....	43
3.2 Analysis strategy.....	45
3.3 Systematics.....	51
3.3.1 Systematics from Non uniform phi distribution	51
3.3.2 Systematics from Event selection	53
3.3.3 Systematics from Track selection.....	55
3.3.4 Overall systematic uncertainty	57
Chapter 4. Results	60
4.1 $SC(m, n)$ Results.....	60
4.1.1 $SC(3, 2)$ and $SC(4, 2)$	60
4.1.2 Model Comparison	63
4.2 Higher order flow harmonics results.....	71
4.3 p_T dependence of $SC(m, n)$ and normalized $SC(m, n)$	75
4.4 Method comparison	80
Chapter 5. Conclusion and Outlook	87
Appendices	90
Chapter A. Toy MC simulation.....	91
A.0.1 Toy Monte Calro simulation	91
A.0.2 Test non-flow effects by impose jets from PYTHIA into ToyMC .	97
Chapter B. Choosing weight for event average	102
Chapter C. Jet energy loss as function of path-length	105
C.1 Basic motivation.....	105
C.2 Analysis	105
C.2.1 Inclusive R_{AA}	105
C.2.2 Elliptic flow.....	106
C.2.3 R_{AA} as function of $\Delta\phi$	106
C.2.4 Path-length calculation with Glauber model	107

C.3	Result	108
C.3.1	$R_{AA}(p_T, \Delta\phi)$	108
C.3.2	Convert $\Delta\phi$ to path-length.....	109
C.3.3	Path-length dependence of R_{AA}	109
C.4	Summary	113
Chapter D.	Software and Data Information	114
D.0.1	Software Information	114
D.0.2	Data Information	114
References	115	

List of Figures

Figure 1.1 A schematic phase diagram of QCD matter [1]	4
Figure 1.2 Schematic light cone diagram of the evolution of a high energy heavy ion collision	5
Figure 1.3 Schematic sketch of transverse projectile view of the non-central collision [2]. The matter created in the collision (red) is called the participant region. The nucleons in the blue region are called spectators. The grey plane in the left figure is called the reaction plane.	11
Figure 1.4 The created initial transverse energy density profile and its time dependence in coordinate space for a non-central heavy-ion collision [3] As shown in the bottom figure, the anisotropy of space(ϵ_x) coordinate becomes smaller over time, while the momentum anisotropy of momentum space (ϵ_p) increases as system expand as time goes.	13
Figure 1.5 The illustration of the elliptic flow development in the two extreme cases: a large and small mean free path among the produced particles in the left and right images, respectively [4].	14
Figure 1.6 The transverse profile in a single event simulated using the Monte Carlo Glauber model [5, 6] (a) Green circles are the positions of the nucleon-nucleon collisions. The 2nd harmonic event plane is slightly inclined around the reaction plane. (b) It also has a non-zero triangle anisotropy. The azimuthal angle of the triangle anisotropy, i.e., the 3rd event plane angle Ψ_3 is not correlated to the reaction plane.....	15
Figure 1.7 The published results of flow with ALICE Pb + Pb $\sqrt{S_{NN}} = 2.76\text{TeV}$ with various measurement methods [7].	23

Figure 1.8 Transverse momentum dependence of nuclear modification factor R_{AA} for charged particles produced in heavy ion collisions at SPS, RHIC, and LHC [8].....	24
Figure 1.9 The two event plane correlators by using two subevent groups by ATLAS collaboration. $\langle \sum \Phi \rangle \equiv \langle jk(\Phi_n - \Phi_m) \rangle$. Results from the AMPT model calculation via the SP method(solid line) and the EP method(dashed line) for represent for comparison [9].....	28
Figure 1.10 Measurement of v_4 with different methods as a function of p_T for the indicated centrality bins. The event plane method with its own event plane(red circle) and the event plane method with 2nd order event plane (blue diamonds) are drawn together.[10]	29
Figure 2.1 Schematic view of Large Hadron Collider.....	31
Figure 2.2 Schematic view of ALICE detector [11].....	32
Figure 2.3 ALICE Inner Tracking System(ITS), includes Silicon Pixel Detector(SPD) and Silicon Drift Detector(SDD) and Silicon Strip Detector(SSD)	33
Figure 2.4 ALICE Time Projection Chamber	36
Figure 2.5 ALICE VZERO detectors on both side of TPC	37
Figure 2.6 Picture of general schema of the AliRoot architecture [12]	40
Figure 3.1 Ratio of $dN/d\eta$ for flip over +/- η region(left) and χ^2/NDF for ϕ flatness as function of RunID	43
Figure 3.2 χ^2/NDF for ϕ flatness for $\eta < 0$ (left) and $\eta > 0$ (right).....	44
Figure 3.3 Results of $SC(3, 2)$ (left) and $SC(4, 2)$ before auto (self)-correlation correction(open makers) and after correction(closed markers)	50
Figure 3.4 Scaled ratio of $dN/d\phi$ distribution of ALICE LHC10h dataset to flat distribution (AMPT True). The reconstructed AMPT, and LHC11h with TPC only track cut, and LHC10h with Global SSD track cut were also drawn together for comparison.	52
Figure 3.5 Z-vertex distribution of ALICE Pb + Pb $\sqrt{S_{NN}} = 2.76$ TeV with minimum bias triggered events	54

Figure 3.6 The 2-dim distribution of TPC multiplicity and Global multiplicity. Left is the before exclude outlier(left) and right figure is after exclude outlier(right) events.	55
Figure 3.7 χ/NDF of $dN/d\varphi$ distribution from ALICE LHC10h data with TPC only track selection filter and Global SDD filter.	56
Figure 3.8 Tracking efficiency of single particle reconstruction as a function of p_T (left) and contamination of single particle as a function of p_T (right) for ALICE with various track selection filter.	58
Figure 4.1 The results of $SC(3, 2)$ (blue) and $SC(4, 2)$ (red) with ALICE Pb+Pb $\sqrt{S_{NN}} = 2.76\text{TeV}$ as function of collision centrality (Top). The $NSC(m, n)$ results which scaled with $\langle v_m^2 \rangle \langle v_n^2 \rangle$ were placed in Bottom. The dashed lines are hydrodynamic prediction from H. Niemi with various η/s parametriza- tions [13]	61
Figure 4.2 Result of SC(3,2) and SC(4,2) with HIJING simulations. Defaults($0.2 <$ $p_T < 5.0\text{GeV}/c$) are drawn as full square with blue color, and different minimum cut conditions are listed in legend. A small shifts along the x axis were applied for better visibility.....	62
Figure 4.3 Normalized $SC(m, n)$ (red) with the comparison to MC-Glauber mod- els using wounded nucleon (WN) and binary collisions (BC) weigths.....	65
Figure 4.4 Result of $SC(3, 2)$ and $SC(4, 2)$ with LHC10h data and comparison to various AMPT simulations with different settings. The upper figures are the result of $SC(m, n)$ and the lower figures are the result of nor- malized $SC(m, n)$	67

Figure 4.5 Result of $SC(3, 2)$ (left) and $SC(4, 2)$ (right) with LHC10h data and various VISH2+1 calculation with different settings. The three initial conditions from AMPT, KLN, and Glauber simulations are drawn as a different color. Furthermore, the hydrodynamic properties of η/s are shown as line style, the small share viscosity ($\eta/s=0.08$) are shown as solid line, and large share viscosity ($\eta/s=0.2$ for KLN and Glauber, 0.16 for AMPT) is drawn as dashed line. Upper figures are the result of $SC(m, n)$ and lower figures are results of normalized $SC(m, n)$	69
Figure 4.6 The result of $SC(m, n)$ (upper figure) and $NSC(m, n)$ (bottom figure) with higher order up to 5th flow harmonics with q-Cumulants method from ALICE Pb+Pb $\sqrt{S_{NN}} = 2.76\text{TeV}$. Note that The lower order $SC(m, n)$ are scaled down. Both $SC(m, n)$ and $NSC(m, n)$ with lower orders are drawn as colored band and statistical and systematical errors were quadratically merged.	72
Figure 4.7 Result of higher order $NSC(m, n)$ and comparison to MC-Glauber models and prediction from J.Y Ollitraults[14]	73
Figure 4.8 Result of $SC(5, 2)$, $SC(5, 3)$ and $SC(4, 3)$ and comparison to various AMPT simulations with different settings. Upper figures are the results of $SC(m, n)$ and the lower figures are the results of $NSC(m, n)$	74
Figure 4.9 Result of $SC(5, 2)$, $SC(5, 3)$ and $SC(4, 3)$ with ALICE data and comparison to various VISH2+1 calculation with different settings. The configurations are same as Fig.4.5	75
Figure 4.10 The results of $SC(3, 2)$ and $SC(4, 2)$ with various minimum p_T cut conditions(Top) and results of $NSC(3, 2)$ and $NSC(4, 2)$ (Middle). The ratio of $NSC(m, n)$ results with various minimum p_T cut conditions to default($0.2 < p_T < 5.0\text{GeV}/c$) are shown in bottom figure.	77
Figure 4.11 The results of $SC(3, 2)$ and $SC(4, 2)$ with various minimum p_T cut conditions(Top) and results of $NSC(3, 2)$ and $NSC(4, 2)$ (Middle). The ratio of $NSC(m, n)$ results with various minimum p_T cut conditions to default($0.2 < p_T < 5.0\text{GeV}/c$) are shown in bottom figure.	78

Figure 4.12 $NSC(3, 2)$ (Top) and $NSC(4, 2)$ (Bottom) as a function of minimum p_T cuts with ALICE Pb+Pb $\sqrt{S_{NN}} = 2.76\text{TeV}$. The AMPT simulation results are drawn together as colored band for comparison. The corresponding AMPT configurations are shown in legend.	79
Figure 4.13 Comparison of $SC(m, n)$ (Top) and normalized $SC(m, n)$ (Bottom) results for $SC(3, 2)$ (blue) and $SC(4, 2)$ (red) with the SP and QC method up to 60% centralities. The different ratios are shown in lower pads, and systematic uncertainty is drawn as a band around 1	82
Figure 4.14 Result of higher order $SC(m, n)$ and $NSC(m, n)$ with two different method QC and SP. Along x-axis offset was applied for better visibility. For the QC method $ \eta < 0.8$ cut was applied, while SP method takes $0.4 < \eta < 0.8$	83
Figure 4.15 $SC(m, n)$ and $NSC(m, n)$ with SP method with default cuts (0.2 ; p_T ; 5.0 GeV/c) and various minimum p_T cuts up to 0.7 GeV/c	84
Figure 4.16 $SC(m, n)$ and $NSC(m, n)$ with SP method with default cuts (0.2 ; p_T ; 5.0 GeV/c) and various minimum p_T cuts up to 1.5 GeV/c 85	
Figure 4.17 The ratio of $NSC(m, n)$ with SP method to the default cuts	86
Figure A.1 Flow measurement with ALICE at $\sqrt{S_{NN}} = 2.76\text{TeV}/c$ and $5.02\text{TeV}/c$ with various measurement methods, also hydrodynamic predictions are drawn as bands	95
Figure A.2 Results of ToyMC simulation for SC(3,2) with random uniform distribution of v_n with various multiplicity. The left figure is the result from 50 to 450 multiplicity, and right figure is the result from 500 to 1800 multiplicity. Both Q-cumulatns(QC) and Scalar Product(SP) mehtods are tested and drawn with red and blue color marker. Also ratio to input values are drawn in bottom pad, and the ratio of SP / QC methods are drawn with green marker	96

Figure A.3 Results of ToyMC simulation for SC(4,2) with random uniform distribution of v_n with various multiplicity. The left figure is the result from 50 to 450 multiplicity, and right figure is the result from 500 to 1800 multiplicity. Both Q-cumulatns(QC) and Scalar Product(SP) mehtods are tested and drawn with red and blue color marker. Also ratio to input values are drawn in bottom pad, and the ratio of SP / QC methods are drawn with green marker	97
Figure A.4 Event by Event Flow harmoics distributions from Bessel Gaussian function based on [?].....	98
Figure A.5 Results of ToyMC simulation for SC(m,n) with Bessel Gaussian like distribution, Both SP and QC results were performed and the ratio of two different methods are show in bottom pad	99
Figure A.6	100
Figure A.7 The ToyMC results of SC(3,2) (left) and SC(4,2) (right) from 400 to 1800 multiplicity. The input values are drawn as green line. Closed markers are the results with SP and QC results without jet implementation(as same as previous results) and open markers are the results after PYTHIA jet embedding. The ratio to the input values are drawn in bottom pad	101
Figure C.1 Basic concept of definition of path-length for given angle $\Delta\phi$ (top), and results for centrality 00-10% and 40-50%(bottom). Open symbols are path-length which is calculated from Eq.C.7. Closed symbols are length from center to edge of region.....	108
Figure C.2 R_{AA} versus $\Delta\phi$ for LHC experiment for given p_T bins. Statistical errors and systematical errors are evaluated quadratic.	110

Figure C.3 Geometrical simulation result of path length calculation vs angle with respect to reaction plane by using TGlauber simulation for ALICE(open symbols) and PHENIX(closed symbols), plotted for the six centralities as shown in legend. The angle respect to reaction plane, $\Delta\phi$ is for the center of the bins(7.5, 22.5, 37.5, 52.5, 67.5 and 82.5) and centrality dependent offset is introduced for visual clarity	111
Figure C.4 R_{AA} versus Path-length correspond to $\Delta\phi$ for LHC experiment for given p_T bins. Statistical errors and systematical errors are evaluated quadratic.	112
Figure C.5 Comparison of R_{AA} as function of path length for ALICE and PHENIX with 7~8 GeV/ c p_T bin	113

List of Tables

Table 3.1	ALICE Track selection filter conditions	56
Table 3.2	Systematic uncertainties of $SC(m, n)$. Overall systematics are quadratically merged results of each individual systematic error	59
Table 3.3	Systematic uncertainties of $NSC(m, n)$. Overall systematics are quadratically merged results of each individual systematic error	59
Table 4.1	Configurations of AMPT simulation dataset which correspond to ALICE LHC10h data with Pb+Pb $\sqrt{S_{NN}} = 2.76\text{TeV}$	68
Table D.1	List of AMPT datasets and configuration.....	115

ABSTRACT

Study of correlation between flow harmonics in Heavy Ion collisions at $\sqrt{s_{NN}} = 2.76 \text{ TeV}$ with ALICE at LHC

Myunggeun Song

Physics Department

The Graduate School, Yonsei University, Seoul, Korea

How did the universe begin? Relativistic heavy-ion collisions can answer this simple question since it can produce an extreme state of very hot and dense system similar to the state just after the Big Bang.

The existence of QGP at extreme conditions such as high temperature and energy density were proved by the Relativistic Heavy Ion Collider (RHIC) at BNL and Large Hadron Collider (LHC) at CERN. One of the most important probes to assess the properties of QGP is collectivity behavior of particle production in transverse direction. This phenomena were analyzed with Fourier's series transformations. Each order of Fourier harmonics is called "flow"(v_n). This flow provides not only evidence of existence of QGP matter, but also hints of the properties of created medium.

The large v_2 (also known as "elliptic flow") discovered at RHIC energies (and also found at LHC energy of 2.76TeV) were explained by pressure effect of the almond-like shape of the collision overlap region. It also demonstrated that the QGP behaves like a

strongly coupled liquid with a very small ratio of the share viscosity-to-entropy density (η/s). In this thesis the recent results of studies about flow and the few representative methods to measure flow are presented.

The other harmonics, such as odd and higher harmonics were explained as the result of fluctuation of initial geometry. However, this simple geometrical flow approach cannot explain the possible relation between two different flow harmonics. To measure and quantify the correlation between flow harmonics, new observable *SymmetricCumulants* have been introduced without biases originating from non-flow effects and any dependence on event planes.

The results from Pb + Pb collisions at ALICE with $\sqrt{s_{NN}} = 2.76\text{TeV}$ correlation between flow harmonics up to 5th order are discussed, and the transverse momentum dependences of correlations are analyzed. Data from this study also are compared to model simulations from viscous hydrodynamics, AMPT, and HIJING models.

Together with existing measurements of individual flow harmonics, this analysis of heavy-ion collisions aims to better determine the initial conditions and η/s as the transport properties of the system produced.

Key words : LHC, ALICE, Flow, Correlation, Fluctuation, elliptic flow(v_2), $SC(m, n)$

¹ Chapter 1

² Introduction

³ One of the main goals of relativistic heavy ion collision experiments is to discover
⁴ the confinement state, which is often called *Quark – Gluon – Plasma* (QGP). Study of
⁵ the properties of QGP status, such as equation of state, temperature, order of the phase
⁶ transition, transport coefficient, and chemical evolution leads to a deeper understand-
⁷ ing of dominant physics of heavy ion collision experiments. In this chapter, the basic
⁸ motivation of heavy ion collision experiments and the measurement of the azimuthal
⁹ correlation are introduced.

¹⁰ 1.1 Quantum Chromo Dynamics (QCD)

¹¹ *Quantum chromodynamics* (QCD) is a fundamental theory relating to strong in-
¹² teractions between the quarks and gluons. QCD was developed as an extension of quan-
¹³ tum electrodynamics(QED) by the imposition of a local SU(3) symmetry in “color”
¹⁴ space. The color confinement refers to the fact that quarks and gluons cannot be isolated
¹⁵ and therefore cannot be observed directly. Quarks are confined within colorless particles
¹⁶ called hadrons. Mesons are composed of quarks and anti-quarks ($q\bar{q}$), and baryons are
¹⁷ composed of three quarks (qqq or $q\bar{q}q$). The Strong interaction is governed by

$$V(r) = -\frac{4}{3}\frac{\alpha_s}{r} + kr, \quad (1.1)$$

¹⁸ Where α_s is the coupling strength, and k is the string tension. The second term in Eq.1.1
¹⁹ shows that as the distance increases the attractive force increases, this force prevents the

isolation of quarks. Therefore, all quarks are confined within hadrons, and not one can be observed as a free quark in nature. For example, when the distance between a quark-antiquark pair in a meson is increased by inserting more and more energy in the system, at some point it becomes more energetically favorable to produce a new quark-antiquark pair from the vacuum, which will then with the original quark-antiquark pair combine and form two new mesons, preventing in turn the quarks and antiquarks from original meson to be deconfined and to be found isolated.

The most important difference between QCD and QED is that QCD is a non-Abelian gauge theory and self-interacts with gluon as a consequence. The QCD interactions among quarks and gluons become weaker at high energy (called “asymptotic freedom”), while the quarks and gluons are confined inside the hadrons at low energy [15, 16]. The strong coupling constant α_s can be expressed as a function of the momentum transfer Q^2 , as follows:

$$\alpha_s(Q^2) \sim \frac{12\pi}{(33 - 2N_f) \ln(Q^2/\lambda_{QCD}^2)} \quad (1.2)$$

33

where N_f is the number of quarks flavors and $\lambda_{QCD} \sim 0.2\text{GeV}$ is a typical QCD scale. When the momentum transfer Q^2 is large enough when compared with λ_{QCD}^2 , the α_s becomes small enough to allow the use of the perturbative method for QCD calculation (pQCD) as like in the QED [17]. On the other hand, when Q^2 is not large enough, QCD remains in a non-perturbative regime.

39 1.2 Quark Gloun Plasma (QGP)

According to the “Standard Model” quarks interact via a strong nuclear force which is carried by other elementary particles called gluons. The physical quantity for the strong interaction is ‘color’, which comes in three instances: red, blue and green, and the corresponding negative units (“anti-red”, “anti-blue”, and “anti-green”). Quarks carry only a single positive (negative) unit of color, while gluons carry the set of colors, i.e., they carry one positive and one negative unit of color. Since the strong interaction be-

46 tween quarks is transmitted via gluons, which carry only a discrete number of colors
47 (gluons, for instance, do not have mass, charge, or flavor), the strong interaction only
48 can change the color of the interacting quarks. For this reason the underlying fundamen-
49 tal theory of strong nuclear reaction is called “*Quantum Chromodynamics*” (QCD).

50 At ordinary temperatures and energy densities, normal matter is confined within a
51 radius that corresponds to the QCD scale. However, at a sufficiently high temperature
52 (or energy density), the color confinement can be broken. This phase transition from the
53 confined nuclear matter to a deconfined state is the main subject of heavy ion collision
54 physics.

55 In relativistic heavy ion collision, the hadrons start to “melt” into deconfined quarks
56 and gluons. These transitions are predicted by Lattice QCD calculations [18] and pro-
57 duce Quark Gluon Plasma (QGP) as the state of matter consisting of deconfined quarks
58 and gluons (And Plasma is a general term used for physical system in which charges are
59 screened due to the presence of other mobile charges). This QGP status is considered
60 to have existed in the early universe, a few microseconds after the Big Bang [19, 20].
61 The Lattice QCD calculation predicts that the phase transition to a QGP state occurs at a
62 critical temperature T_c around $150 \sim 200$ MeV [21]. This phase transition temperature
63 might be reached in heavy-ion collisions currently delivered at RHIC with Au-Au colli-
64 sions at a center of mass energy of 200 GeV per nucleon pair, and at LHC with Pb-Pb
65 collision at a center of mass energy of 2.76 TeV per nucleon pair. The schematic phase
66 diagram of QGP matter is illustrated in Fig.1.1, where the horizontal axis is the baryon
67 density and the vertical axis is the temperature.

68 **1.3 Heavy ion collision**

69 As mentioned above, the universe started from a single point at approximately 14
70 billion years ago(Big Bang), and expanded and cooled down. During this expansion
71 a transition from a QGP phase to a hadronic phase happen, which allowed for the
72 formation of hadrons. To study this procedures, we collide heavy-ions at ultra-relativistic
73 energies, where one creates QGP matter in the laboratory under controlled conditions.

74 In the LHC experiment, the heavy ions are accelerated up to almost the speed of

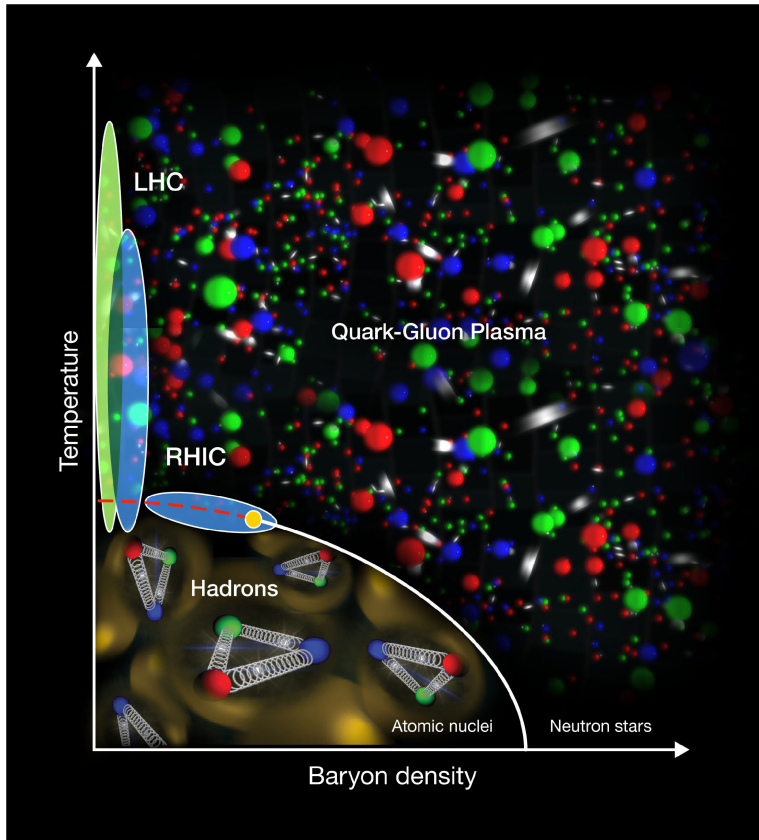


Figure 1.1: A schematic phase diagram of QCD matter [1]

75 light and collide with each other. In this relativistic heavy ion collision, the initial energy
 76 density participating in the collision is expected to be well above the threshold for the
 77 QGP formation [22]. In a canonical picture of the collision [3] the system evolution can
 78 be divided into several stages, as shown in Figure.1.2

- 79 1. Initial state
- 80 2. thermalized QGP
- 81 3. hadronic gas
- 82 4. chemical freeze-out
- 83 5. kinetic freeze-out(free streaming)

84 At first, the two nuclei traveling at relativistic speeds become longitudinal Lorentz-
 85 contracted disks. A large number of the collisions between participants in target and
 86 projectile nuclei occur, and it is expected that the produced partons are strongly coupled
 87 with each other and thermalized into the QGP phase rapidly within a short time (less
 88 than a few fm/c). After $\sim 20\text{fm}/c$ the temperature of the expanding medium drops down
 89 below the critical temperature T_c [23]. The quarks and gluons become confined into
 90 hadrons. Afterward, the expansion (and the temperature fall) leads to a reduction of
 91 the inelastic processes among hadrons, until the relative abundance of hadron species
 92 is fixed (chemical freeze-out), and then to the stop of any interaction which fixes the
 93 kinetic spectra (kinetic freeze-out).

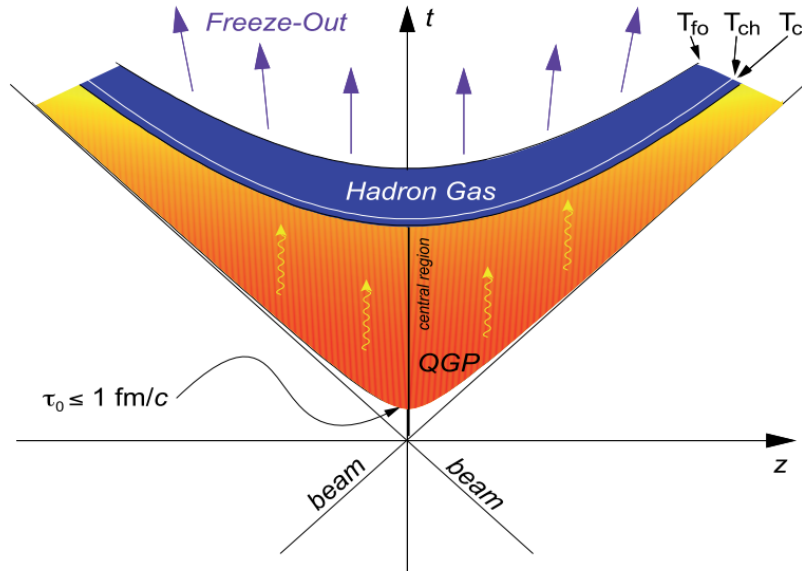


Figure 1.2: Schematic light cone diagram of the evolution of a high energy heavy ion collision

94 To verify the existence of the phase transition and the formation of QGP in heavy ion
 95 collisions, physics observables should be identified for each stage of dynamical evolution
 96 of the produced medium. Ordered in sequence of their formation in the course of the
 97 dynamics, the most relevant observables are characterized as follows:

- 98 • Suppression of heavy quarkonia production by Devye screening in the QGP
 - 99 • Suppression of di-jets by losing their energy in the medium, so the undisturbed
 - 100 parton form a jet while the other one is absorbed in the medium and not detected
 - 101 (or distorted)
 - 102 • High- p_T particles produced in primordial $\hat{q}q, \hat{g}g, \hat{q}\bar{q}$ reactions with high momen-
 - 103 tum transfer are attenuated by gluonic bremsstrahlung in QGP medium
 - 104 • Hydrodynamics collective motion develops with the onset of thermal equilibrium
 - 105 • Hadronic chemical freeze-out fixes the abundance ratios of the species
 - 106 • Two particle Bose-Einstein-Correlations (the HBT effect of quantum optics) re-
 - 107 sulted from the kinetic freeze out stage
- 108 Notably, the QGP matter collectively expand both in the longitudinal and the trans-
- 109 verse direction. The transverse expansion leads the collectivity motion of system, which
- 110 is often called the flow. The produced particles gain the momentum and energy from the
- 111 radial flow of the QGP matter, and a final distribution of the transverse momentum is
- 112 modified from the superposition of the independent nucleon-nucleon collisions [24].

113 1.4 Flow

114 Introduction

115 In previous section, the phase transition is expected to occur at $T_c \sim 150$ MeV, corre-

116 sponding to an energy density of $\epsilon_c \simeq 0.15 - 0.5 \text{GeV}/fm^3$ [25], which could be already

117 be achieved at RHIC or LHC energies. Thus, experimental measurements in relativis-

118 tic heavy ion collisions could shed light on the properties of the QGP. The main goal

119 of studying relativistic heavy ion collisions is to discover and understand its properties

120 of created matter. The system produced in relativistic heavy ion collisions dynamically

121 evolves within a time duration of the order of fm/c . Therefore one has to describe the

122 space-time evolution of thermodynamic variables to fill the large gap between the static

123 aspects of QGP properties and the dynamical aspects of heavy ion collisions, and hydro-
124 dynamics plays an important role in connecting them. Hydrodynamics is thus applied to
125 matter under local equilibrium in the intermediate stage.

126 Also by using hydrodynamics, we can remove QCD Lagrangian density

$$\mathcal{L} = \bar{\psi}_i (i\gamma_\mu D_{ij}^\mu - m\delta_{ij})\psi_j - \frac{1}{4} F_{\mu\nu\alpha} F^{\mu\nu\alpha} \quad (1.3)$$

127

128 where ψ_i is a quark field, γ are Dirac matrices, D is a covariant derivative, m is a
129 quark mass, δ is the Kronecker delta symbol, and F is the field strength of the gluons.
130 In spite of simple looking of QCD Lagrangian form, it is very difficult to make any
131 predictions directly from QCD due to its complexity which mainly arises from the non-
132 linearity of the interactions of the gluons, the strong coupling, the dynamical many body
133 system and confinement. In hydrodynamics, however, as a phenomenological theory, we
134 can express the equation of state as follows:

$$P = P(e, n) \quad (1.4)$$

135

136 which expresses the pressure P as a function of energy density e and the baryon
137 density n . Such an equation can be obtained by performing numerical simulations of
138 QCD on the lattice. To calculate the above equation of the states, it is also necessary
139 to use additional transport coefficients such as shear viscosity η , bulk viscosity ζ , heat
140 conductivity λ , etc.

141 Hydrodynamics can also produce outputs, such as local temperature or energy den-
142 sity, that could be useful in describing the dynamics for other observables. For instance,
143 in the current formalism of jet quenching, one needs information regarding parton den-
144 sity or energy density along a trajectory of an energetic parton.

145 Hydrodynamics also provides information regarding bulk matter. Therefore we can
146 say that, in the context of relativistic heavy ion collisions, hydrodynamics is the heart
147 of the dynamical modeling since it not only describes expansion and collective flow of

148 matter, but also provides important information about the intermediate stage for other
149 phenomena.

150 **Formal definitions**

151 The particle azimuthal distribution($r(\varphi)$) is a periodic quantity (over 0 to 2π in polar
152 coordinate), and it can be expand with customary expressed in a Fourier series [4, 26],

$$r(\varphi) = \frac{x_0}{2\pi} + \frac{1}{\pi} \sum_{n=1}^{\infty} [x_n \cos(n\varphi) + y_n \sin(n\varphi)] \quad (1.5)$$

153

154 where, Fourier coefficient x_n, y_n is defined as

$$x_n = \int_0^{2\pi} r(\varphi) \cos(n\varphi) d\varphi \quad (1.6)$$

155

$$y_n = \int_0^{2\pi} r(\varphi) \sin(n\varphi) d\varphi \quad (1.7)$$

156

157 For our case, the multiplicity is finite, therefore x_n and y_n are changed into finite
158 sum as like

$$x_n = \sum_{\nu} r_{\nu} \cos n\phi_{\nu} \quad (1.8)$$

159

$$y_n = \sum_{\nu} r_{\nu} \sin n\phi_{\nu} \quad (1.9)$$

160

161 r_{ν} is weight for particle, and usually it takes unity($r_{\nu} = 1$) for inclusive flow mea-
162 surement. If there is no flow effect and fluctuation, the azimuthal distribution $r(\varphi)$
163 should be const. i.e. isotropic multiplicity for all angles, and all the coefficient of sin
164 and cos terms will be vanished. On the other hand, if there are any anisotropic effect,
165 coefficient x_n and y_n will survive.

166 If we define the v_n , and ψ_n for each corresponding Fourier's harmonics in the fol-
167 lowing way:

$$v_n \equiv \sqrt{x_n^2 + y_n^2} \quad (1.10)$$

$$0 \leq \psi_n \leq \frac{2\pi}{n} \quad (1.11)$$

168

169

we can now express azimuthal particle distribution with v_n and ψ_n instead of x_n and y_n .

$$x_n = v_n \cos n\psi_n \quad (1.12)$$

$$y_n = v_n \sin n\psi_n \quad (1.13)$$

173

If we put back x_n and y_n into original Eq.1.5 then

$$\frac{dN}{d\phi} = \frac{x_0}{2\pi} + \frac{1}{\pi} \sum_{n=1} (v_n \cos n\psi_n \cos n\phi + v_n \sin n\psi_n \sin n\phi) \quad (1.14)$$

$$= \frac{x_0}{2\pi} + \frac{1}{2\pi} \sum_{n=1} (2v_n \cos n(\phi - \psi_n)) \quad (1.15)$$

175

From Eq.1.14 to 1.15, the sinus terms were vanished because of symmetry of the collision. As illustrated in Fig.1.3, if the colliding nuclei are the same, the probability for a produced particles to be emitted in direction φ and $-\varphi$ is equal. As defined in Eq.1.9, y_n is average of $\langle \sin(n\varphi) \rangle$, and this average of sinus term will be canceled each other of any angle φ with its symmetries

$$\sin(n\varphi) + \sin(n(-\varphi)) = \sin(n\varphi) - \sin(n\varphi) = 0 \quad (1.16)$$

From Eq.1.15, harmonics v_n can be related explicitly to the origin azimuthal distribution $r(\varphi)$ in the following way:

$$\langle \cos(n\varphi) \rangle \equiv \frac{\int_0^{2\pi} \cos(n\varphi) r(\varphi) d\varphi}{\int_0^{2\pi} r(\varphi) d\varphi} \quad (1.17)$$

$$= \frac{\frac{1}{\pi} v_n \int_0^{2\pi} \cos^2(n\varphi) d\varphi}{v_0} \quad (1.18)$$

$$= \frac{v_n}{v_0} \quad (1.19)$$

183 Using a normalized distribution $r(\varphi)$, for which $v_0 = \int_0^{2\pi} r(\varphi) d\varphi = 1$, the above
 184 equation leads to:

$$v_n = \langle \cos(n\varphi) \rangle \quad (1.20)$$

185
 186 The harmonic v_1 is often called “directed flow”, and v_2 called “elliptic flow”, and
 187 v_3 is “triangular flow”. When we consider the polar coordinate with (r, φ) , then the
 188 distribution for ellipse-like is determined by the following equation.

$$r(\varphi) = \frac{a(1 - \varepsilon^2)}{1 + \varepsilon \cos \varphi} \quad (1.21)$$

189
 190 where ε is the eccentricity defined as

$$\varepsilon^2 \equiv 1 - \frac{b^2}{a^2} \quad (1.22)$$

191 with definition of a is major, and b is minor axis. With this parameterization, v_n can
 192 be calculated analytically in a closed form, as like

$$v_n = 2\pi b(-1)^n \left(\frac{a-b}{a+b}\right)^{\frac{n}{2}} \quad (1.23)$$

193 The methods that attempt to explain the azimuthal distribution of particles produced
 194 with customized Fourier’s expansion have been succeeded in relativistic heavy ion col-
 195 lision, especially in RHIC and LHC, by studying about strong collective and anisotropic
 196 flow in the transverse plane driven by the pressure gradients with more particles emitted

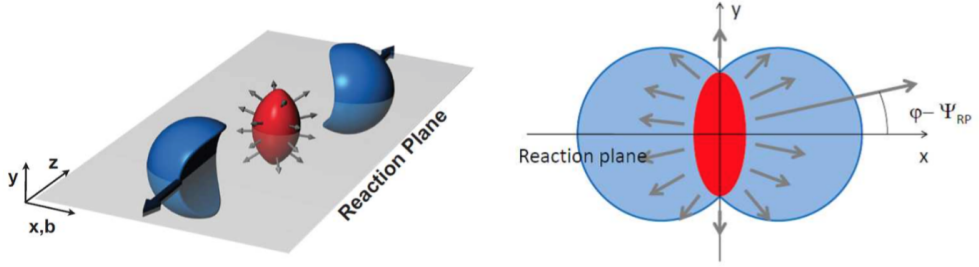


Figure 1.3: Schematic sketch of transverse projectile view of the non-central collision [2]. The matter created in the collision (red) is called the participant region. The nucleons in the blue region are called spectators. The grey plane in the left figure is called the reaction plane.

197 in the direction of the largest gradients. The large elliptic flow discovered at RHIC en-
 198 ergies [27] continuous to increase also in LHC energies [7, 28]. This has been predicted
 199 by calculations utilizing viscous hydrodynamics [29, 24, 30, 31, 32, 33].

200 These calculations also demonstrated that the shear viscosity to the entropy density
 201 ratio (η/s) of strongly interacting matter is close to a universal lower bound $1/4\pi$ [34]
 202 in heavy ion collisions at RHIC and LHC energies.

203 The temperature dependence of the η/s has some generic features that most of the
 204 known fluids obey. One such general behavior is that the ratio typically reaches its
 205 minimum value close to the phase transition region [35]. It was shown, using kinetic
 206 theory and quantum mechanical considerations [36] that $\eta/s > 1/15$ would be an order
 207 of magnitude for the lowest possible shear viscosity to entropy ratio in nature. Later it
 208 was found that one can calculate an exact lower bound $(\eta/s)_{\min} = 1/4\pi \approx 0.08$ using
 209 the AdS/CFT correspondence [34]. Hydrodynamical simulations supports as well the
 210 view that the QGP matter indeed is close to that limit [32].

211 In relativistic collision, each collision is characterized by the impact parameter, de-
 212 fined as the distance between the center of two nuclei points. Collisions with the short
 213 impact parameter are called central collisions and collisions with the long impact pa-
 214 rameter are called peripheral collisions. This geometry of the collision moments with
 215 non-central collision has ellipticity in the transverse plane and is shown in Fig.1.3

216 The initial spatial anisotropy in the azimuthal direction is transformed to the anisotropy
217 of the final particle momentum distributions due to the collective expansion of the pro-
218 duced system. During evolution of the almond-shaped interaction volume, the anisotropy
219 in coordinate space is transformed to anisotropy in momentum space (shown in Fig.1.4).
220 Therefore, these momentum anisotropies of the hydrodynamic matter lead to the anisotropic
221 azimuthal distribution of the produced particles.

222 However, the transverse expansion of system volume is insufficient to explain the
223 anisotropy of azimuthal particle distribution. As shown in Fig.1.5, if there is no inter-
224 action between particles (or the mean free path among the produced particles is much
225 longer than the typical size of the system), the azimuthal distribution of the particles
226 does not depend on azimuthal angle on average due to symmetry of the production pro-
227 cess. On the other hand, when the mean free path is very small compared to the typical
228 system size, hydrodynamics can be applied to describe the space-time evolution of the
229 system. Furthermore, the pressure gradient along the horizontal axis is much longer than
230 the vertical axis due to the geometry.

231 The origin of large v_2 cannot explain other harmonics especially odd number har-
232 monics like v_3, v_5 , etc. The impact parameter vector b (the vector connecting the centers
233 of two colliding nuclei) changes event-by-event, which in turn yields a random reaction
234 plane angle ψ_R (the plane spanned by the impact parameter and the beam axis). Due to
235 these random fluctuations, it is not trivial to set up for each event the coordinate system.
236 Because of the random geometry of participant nucleon in colliding nuclei, the overlap
237 region shape is not a perfect almond shape, but rather a complex shape as shown in
238 Figure.1.6. As a result of this random fluctuation and the complex shape of the energy
239 density profile of the system, the flow harmonics v_n are defined with their own event
240 plane ψ_n , not with respect to reaction plane ψ_R . Although the 2nd harmonics symmetry
241 plane(ψ_2) roughly corresponds to the reaction plane($\psi_2 \sim \psi_R$), their azimuthal angles
242 are slightly inclined event-by-event. In the following section, methods to calculate flow
243 will be discussed.

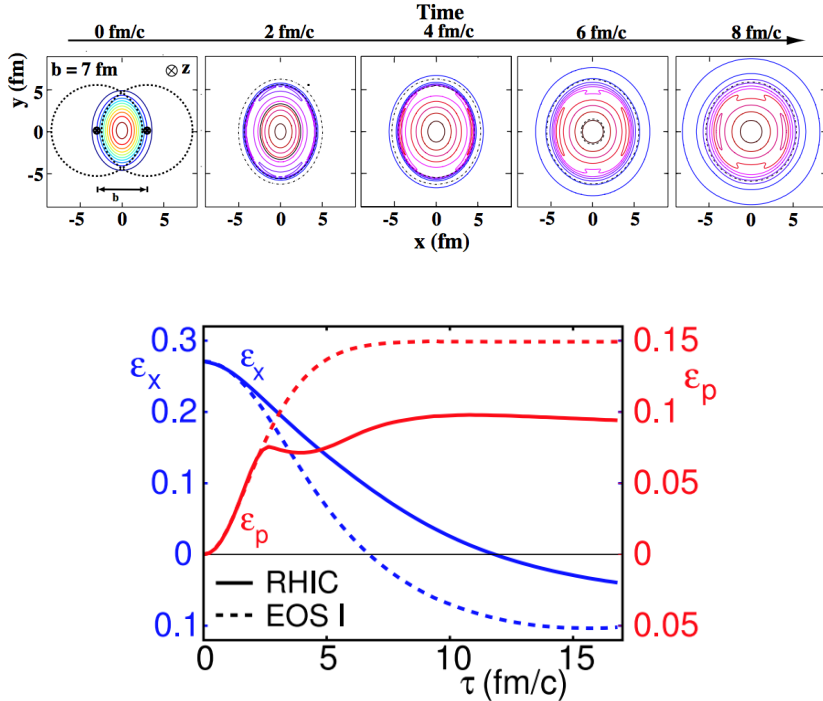


Figure 1.4: The created initial transverse energy density profile and its time dependence in coordinate space for a non-central heavy-ion collision [3]. As shown in the bottom figure, the anisotropy of space (ϵ_x) coordinate becomes smaller over time, while the momentum anisotropy of momentum space (ϵ_p) increases as system expand as time goes.

244 1.4.1 Event Plane method

245 The event plane method (EP) is the most commonly used method to measure anisotropic
 246 flow. Using this method, the event plane is estimated and all particles' azimuthal angles
 247 are correlated to this estimated plane in order to obtain the flow harmonics v_n . From the
 248 Eq.1.13 we can easily calculate event plane angles with the following way:

$$\frac{y_n}{x_n} = \frac{v_n \sin n\psi_n}{v_n \cos n\psi_n} = \tan n\psi_n \quad (1.24)$$

$$\psi_n = (\arctan \frac{y_n}{x_n})/n \quad (1.25)$$

250 and by using Fourier's coefficient relation:

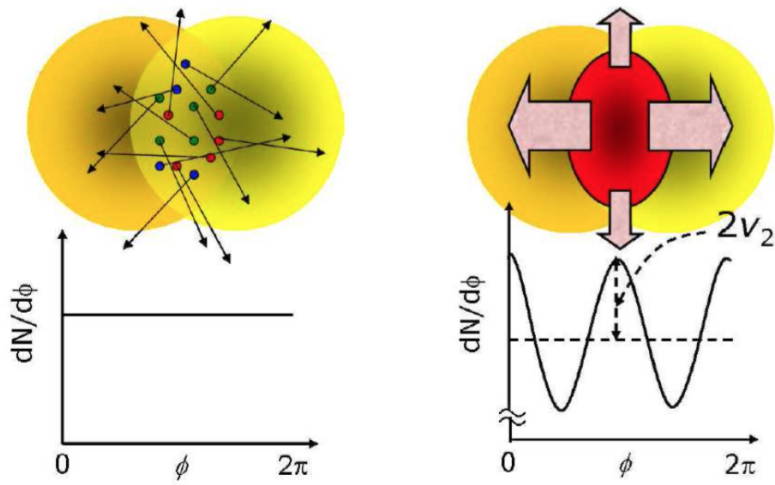


Figure 1.5: The illustration of the elliptic flow development in the two extreme cases: a large and small mean free path among the produced particles in the left and right images, respectively [4].

$$v_n = \langle \cos n(\phi_\nu - \psi_n) \rangle \quad (1.26)$$

251

252 However, in practice, since each event has a finite number of created particles, the
 253 results for the event plane angle will be affected by a limited resolution. This can be
 254 corrected for by estimating the event plane resolution:

$$v_n^{measured} = \langle \cos n(\phi - \psi_n^{measured}) \rangle \quad (1.27)$$

255

256 where, $\psi_n^{measured} = \psi_n + \psi_n^{err}$

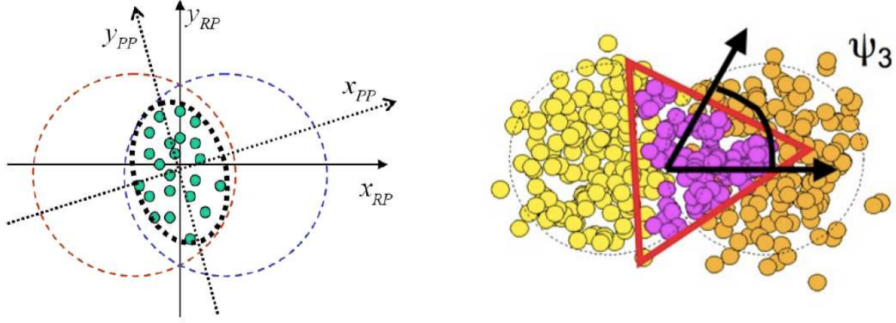


Figure 1.6: The transverse profile in a single event simulated using the Monte Carlo Glauber model [5, 6] (a) Green circles are the positions of the nucleon-nucleon collisions. The 2nd harmonic event plane is slightly inclined around the reaction plane. (b) It also has a non-zero triangle anisotropy. The azimuthal angle of the triangle anisotropy, i.e., the 3rd event plane angle Ψ_3 is not correlated to the reaction plane

$$v_n^{measured} = \langle \cos n(\phi - \psi_n - \psi_n^{err}) \rangle \quad (1.28)$$

$$= \langle \cos n(\phi - \psi_n) \cos n(\psi_n^{err}) + \sin n(\phi - \psi_n) \sin n(\psi_n^{err}) \rangle \quad (1.29)$$

$$= \langle \cos n(\phi - \psi_n) \cos n(\psi_n^{err}) \rangle + \langle \sin n(\phi - \psi_n) \sin n(\psi_n^{err}) \rangle \quad (1.30)$$

$$= \langle \cos n(\phi - \psi_n) \rangle \langle \cos n(\psi_n^{err}) \rangle \quad (1.31)$$

$$= v_n \langle \cos n(\psi_n^{err}) \rangle \quad (1.32)$$

257 Finally, we get

$$v_n = v_n^{measured} / \langle \cos n(\psi_n^{err}) \rangle \quad (1.33)$$

258

259 We assume that event angle error(ψ_n^{err}) is independent of $\phi - \psi_n$, and the expectation
 260 value of $\sin n(\psi_n^{err})$ is zero. The estimated event plane resolution can be obtained by
 261 two or more independent subevents.[37] The advantage of the event plane method is
 262 that it is less sensitive to the number of particles for analysis, and can therefore be used
 263 to measure flow of rare particles. Furthermore, this method can be used to estimate an

264 event plane, especially the 2nd order event plane which is expected to be similar to the
 265 reaction plane $\psi_2 \sim \psi_R$. This 2nd event plane also can be used for jet or other analysis.
 266 The main disadvantage of this method occurs when the event plane resolution is affected
 267 by correlations which do not stem from a genuine correlation of all particles with the
 268 true event plane. While event plane resolution can fix errors from multiplicity, it cannot
 269 fix errors originating from non-flow (e.g., jet, detector smearing, etc.).

270 1.4.2 Scalar product method

271 The original idea behind the event plane method is that the direction of Ψ_n of the
 272 flow vector in a reference frame provides an estimation of the corresponding angle Φ_n
 273 in the underlying probability distribution. Because a finite sample of particles is used,
 274 statistical fluctuation causes Ψ_n to differ from Φ_n . This dispersion is characterized by
 275 the “resolution”, defined as

$$R \equiv \langle e^{in(\Psi_n - \Phi_n)} \rangle \quad (1.34)$$

$$= \left\langle \frac{Q_n}{|Q_n|} e^{-in\Phi_n} \right\rangle \quad (1.35)$$

276 For the fixed v_n , the above equation can be written in the form of

$$R(v_n) \equiv \left\langle e^{in(\Psi_n - \Phi_n)} \right\rangle_{|vn} \quad (1.36)$$

$$= \left\langle \frac{Q_n}{|Q_n|} e^{-in\Phi_n} \right\rangle_{|vn} \quad (1.37)$$

277 where $\langle \dots \rangle_{|vn}$ indicates an average over a large number of event with the same under-
 278 lying v_n . From the Eq.1.26, we can see underlying probability distribution (Eq.1.5) de-
 279 pends on the relative magnitude of the anisotropy v_n to the statistical dispersion $1/\sqrt{N}$.
 280 In the limit $v_n \gg 1/\sqrt{N}$ (large number of multiplicity), easily reconstruct the underly-
 281 ing event plane so that $\Phi_n = \Psi_n$, (i.e. $R(v_n) \sim 1$, and conversely, when the $v_n \sqrt{N} \ll 1$
 282 (low multiplicity) the Resolution $R(v_n) \sim kv_n$, where k is independent of v_n and scale
 283 as $k \sim \sqrt{N}$.

284 Generally, the value falls somewhere between these limits [38], and this nonlinear
 285 dependence of the resolution on the underlying flow is the origin of the difficulties of the
 286 event plane method.

287 When we obtain the event plane resolution from subevents A and B, the resolution
 288 $R(v_n)$ is a factorization like the below definition:

$$\left\langle \frac{Q_{nA}}{|Q_{nA}|} \frac{Q_{nB}}{|Q_{nB}|} \right\rangle = \left\langle \frac{Q_{nA}}{|Q_{nA}|} e^{-in\Phi_n} \right\rangle \left\langle \frac{Q_{nB}}{|Q_{nB}|} e^{-in\Phi_n} \right\rangle^* \quad (1.38)$$

$$= \left| \left\langle \frac{Q_{nA}}{|Q_{nA}|} e^{-in\Phi_n} \right\rangle_{|v_n} \right|^2 \quad (1.39)$$

$$= R(v_{nA})^2 \quad (1.40)$$

289 The Eq.1.37 is used for the second line to third line of the above equation. The event-
 290 plane methods is thus defined as:

$$v_n\{EP\} \equiv \frac{\left\langle Q_n \frac{Q_{nA}^*}{|Q_{nA}|} \right\rangle}{\sqrt{\left\langle \frac{Q_{nA}}{|Q_{nA}|} \frac{Q_{nB}}{|Q_{nB}|} \right\rangle}} \quad (1.41)$$

291

292 Since the measurement has been taken with the average of all events in a given
 293 centrality class, Eq.1.41 changes as term of v_n as like

$$v_n\{EP\} = \frac{\langle v_n R(v_{nA}) \rangle_{v_n}}{\sqrt{\langle R(v_{nA})^2 \rangle_{v_n}}} \quad (1.42)$$

294

295 Note that $\langle R(v_{nA})^2 \rangle \neq \langle R(v_{nA}) \rangle^2$. Resolution correction is no longer a simple
 296 projection of the measured event plane Ψ_n onto the “true” event plane Φ_n .

297 In the limit of infinite multiplicity (i.e. $R(v_n) \sim 1$), $v_n\{EP\}$ does indeed measure
 298 the event averaged mean v_n from Eq.1.5. But in reality, the resolution is not perfect and
 299 the result is usually even closer to the low resolution limit [39], and in this case, the
 300 event-plane measurement thus yields a root-mean-square value. In other words, what
 301 we measure with the event plane method is some values between root-mean-square and

302 mean of v_n depends on the resolution (i.e. Event multiplicity or the performance and
303 acceptance of detector)

$$v_n\{EP\} \simeq \langle v_n \rangle \quad (\text{high resolution limit}) \quad (1.43)$$

$$v_n\{EP\} \simeq \sqrt{\langle v_n^2 \rangle} \quad (\text{low resolution limit}) \quad (1.44)$$

304
305 However, in the scalar product method, which is a slight variant of the event plane
306 method, consists of removing the factor of $|Q_n|$ before taking the average in the numer-
307 ator and denominator of Eq.1.41

$$v_n\{SP\} \equiv \frac{\langle Q_n Q_{nA}^* \rangle}{\sqrt{\langle Q_n Q_{nA}^* \rangle}} \quad (1.45)$$

308 Then, by calculating the scalar product in numerator, the fluctuation term (Resolution
309 related terms) are removed.

$$v_n\{SP\} = \frac{\langle v_n v_{nA} \rangle_{v_n}}{\sqrt{\langle v_n v_{nA} \rangle_{v_n}}} = \sqrt{\langle v_n^2 \rangle} \quad (1.46)$$

310
311 As a result, the scalar product method always yields the root-mean-square v_n , re-
312 gardless of the details of the analysis and makes for a superior measurement.

313 1.4.3 Cumulants method

314 Multi particle correlations

315 Because of the disadvantage of the event plane method (or the scalar product method)
316 in estimating the event plane, the cumulants method (often called the multi-particle cor-
317 relation method) was proposed in order to reduce this bias. This method does not require
318 the event plane estimation event-by-event. Instead, these multi-particle correlations can
319 be calculated by looping over all possible multiplets. If we assume that all the particles
320 have azimuthal correlations which originated from flow harmonics only, then 2- and 4-
321 particle azimuthal correlations can be expressed in the following way:

$$\langle 2 \rangle \equiv \langle e^{in(\phi_1 - \phi_2)} \rangle \equiv \frac{1}{\binom{M}{2} 2!} \sum_{i,j=1, i \neq j}^M e^{in(\phi_i - \phi_j)} \quad (1.47)$$

322

$$\langle 4 \rangle \equiv \langle e^{in(\phi_1 + \phi_2 - \phi_3 - \phi_4)} \rangle \equiv \frac{1}{\binom{M}{4} 4!} \sum_{i \neq j \neq k \neq l}^M e^{in(\phi_i + \phi_j - \phi_k - \phi_l)} \quad (1.48)$$

323

324 where the brackets denote the particle average in a single event. The i, j, k, l denote
 325 identical particles, and ϕ_i is the azimuthal angle of the i -th particle measured in labora-
 326 tory frame. To prevent contribution of self(auto) correlation, the constraints $i \neq j$ and
 327 $i \neq j \neq k \neq l$ have been enforced. When we extend the above equation for event
 328 average, then 2- and 4- particle azimuthal correlations are as follows :

$$\langle \langle 2 \rangle \rangle \equiv \langle \langle e^{in(\phi_1 - \phi_2)} \rangle \rangle \equiv \frac{\sum_{i=1}^N (W_{\langle 2 \rangle})_i \langle 2 \rangle_i}{\sum_{i=1}^N (W_{\langle 2 \rangle})_i} \quad (1.49)$$

329

$$\langle \langle 4 \rangle \rangle \equiv \langle \langle e^{in(\phi_1 + \phi_2 - \phi_3 - \phi_4)} \rangle \rangle \equiv \frac{\sum_{i=1}^N (W_{\langle 4 \rangle})_i \langle 4 \rangle_i}{\sum_{i=1}^N (W_{\langle 4 \rangle})_i} \quad (1.50)$$

330

331 where, N is the number of events, and $W_{\langle 2 \rangle}$ and $W_{\langle 4 \rangle}$ are the event weights. The
 332 selecting event weight is explained in Appendix B. The benefit of using multi-particle
 333 azimuthal correlation is to measure flow harmonics v_n without requiring the event plane
 334 ψ_n ,

$$\langle \langle 2 \rangle \rangle \equiv \langle \langle e^{in(\phi_1 - \phi_2)} \rangle \rangle = \langle \langle e^{in(\phi_1 - \psi_n - \phi_2 + \psi_n)} \rangle \rangle \quad (1.51)$$

$$= \langle \langle e^{in(\phi_1 - \psi_n)} \rangle \langle e^{-in(\phi_2 - \psi_n)} \rangle \rangle = \langle v_n^2 \rangle \quad (1.52)$$

335 In cases when only flow correlations exist in the system, the correlation among any
 336 two particles is induced through the correlation of each particle with the same event
 337 plane ψ_n [40, 41]. Each of these single particle azimuthal distributions is related to the
 338 flow harmonics via Eq.1.15. Therefore we can show that :

$$\langle \langle 4 \rangle \rangle = \langle v_n^4 \rangle \quad (1.53)$$

339

$$\langle\langle 6 \rangle\rangle = \langle v_n^6 \rangle \quad (1.54)$$

340

$$\langle\langle 8 \rangle\rangle = \langle v_n^8 \rangle \quad (1.55)$$

341 and so on, in a similar manner. Crucially, even in an ideal case when there is an
 342 absence of non-flow effects, the cumulants method will be systematically biased due to
 343 flow fluctuation.

$$\langle v_n \rangle^k \neq \langle v_n^k \rangle \quad (1.56)$$

344

345 Flow fluctuation

346 The measuring of flow harmonics is paramount to the measuring of the power of
 347 average values of flow harmonics with multi-particle correlation. However, these two
 348 values are not exactly equivalent even in the ideal case, i.e., when there is no non-flow
 349 effect scenario due to unavoidable flow fluctuations. In the following section methods for
 350 quantifying various powers of flow harmonics will be discussed. For better convention,
 351 v_n will be denoted as simply v .

352 First, let's consider the Taylor expansion for arbitrary functions around mean μ_x up
 353 to second order

$$h(x) = h(\mu_x) + (x - \mu_x)h'(\mu_x) + \frac{(x - \mu_x)^2}{2!}h''(\mu_x) \quad (1.57)$$

354

355 If we take the average of given function $h(x)$ then the Taylor expansion can be
 356 expressed as:

$$\langle h(x) \rangle = h(\mu_x) + (\langle x \rangle - \mu_x)h'(\mu_x) + \frac{\sigma_x^2}{2}h''(\mu_x) \quad (1.58)$$

$$= h(\mu_x) + (\mu_x - \mu_x)h'(\mu_x) + \frac{\sigma_x^2}{2}h''(\mu_x) \quad (1.59)$$

$$= h(\mu_x) + \frac{\sigma_x^2}{2}h''(\mu_x) \quad (1.60)$$

357 where,

$$\sigma_x^2 = \int_{-\infty}^{\infty} (x - \mu_x) f(x) dx$$

358

359 As seen in this equation, the expectation value of linear term(first order) in Taylor's
360 expansion of $h(x)$ around mean μ_x always vanishes. Then we can now estimate the
361 average of various powers of v from Eq.???. For example, in the case $h(v) = v^2$, it
362 follows that :

$$\langle v^2 \rangle = \langle v \rangle^2 + \sigma_v^2 \quad (1.61)$$

363 By using the definition of multi- particle correlation (Eq.1.52 to 1.55), we have

$$v\{2\} = \langle v^2 \rangle^{1/2} \quad (1.62)$$

364 Furthermore, by applying the Taylor expansion above (Eq.1.60) for the case $h(v) \equiv$
365 v^2 , it follows that:

$$\langle v^2 \rangle = (\langle v \rangle^2 + \sigma_v^2)^{1/2} \quad (1.63)$$

$$= \langle v \rangle \left(1 + \frac{\sigma_v^2}{\langle v \rangle^2} \right)^{1/2} \quad (1.64)$$

$$\simeq \langle v \rangle \left(1 + \frac{1}{2} \frac{\sigma_v^2}{\langle v \rangle^2} \right) \quad (1.65)$$

366 For the constraint with:

$$\sigma_v \ll \langle v \rangle \quad (1.66)$$

367 Then we have general results:

$$(1 + x)^n \simeq 1 + nx, \quad (1.67)$$

368 valid for $x \simeq 0$, and the final equation can be expressed as like

$$v\{2\} \simeq \langle v \rangle + \frac{1}{2} \frac{\sigma_v^2}{\langle v \rangle} \quad (1.68)$$

369 From this result, we can conclude that the flow estimation with the 2nd order cumu-
 370 lant will be always systematically biased with positive signature due to flow fluctuations.

371 In addition, the four-particle cumulant can be defined similarly. From the definitions

$$v\{4\} = (-\langle v^4 \rangle + 2\langle v^2 \rangle^2)^{1/4} \quad (1.69)$$

372 with Talyer expansion (Eq.1.60) for the case $h(v) \equiv v^4$ we have up to second order
 373 in σ_v as

$$\langle v^4 \rangle = \langle v \rangle^4 + 6\sigma_v^2\langle v \rangle^2 \quad (1.70)$$

374 as same as 2-particle cumulants, it follows that:

$$v\{4\} = \left[-\langle v \rangle^4 - 6\sigma_v^2\langle v \rangle^2 + 2(\langle v \rangle^2 + \sigma_v^2)^2 \right]^{1/4} \quad (1.71)$$

$$= [\langle v \rangle^4 - 2\sigma_v^2\langle v \rangle^2 + \mathcal{O}(\sigma_v^4)]^{1/4} \quad (1.72)$$

$$= \langle v \rangle \left(1 - 2 \frac{\sigma_v^2}{\langle v \rangle^2} \right)^{1/4} \quad (1.73)$$

$$\simeq \langle v \rangle \left(1 - \frac{1}{2} \frac{\sigma_v^2}{\langle v \rangle^2} \right) \quad (1.74)$$

$$(1.75)$$

375 so, as like $v\{2\}$, the final form is

$$v\{4\} \simeq \langle v \rangle - \frac{1}{2} \frac{\sigma_v^2}{\langle v \rangle} \quad (1.76)$$

376
 377 with this final form, we can conclude that the 4- particle cumulant flow results will be
 378 always systematically biased with negative signature due to statistical flow fluctuations.
 379 This is an opposite trend when compared with 2- particle cumulant results (Eq.1.68).
 380 Due to this reason, the $v_n\{2\} < v_n\{EP\} < v_n\{4\}$ and explain the difference between
 381 different flow measurement methods as shown in Fig.1.7.

382 The higher-order cumulants like 6-particle or 8-particle correlation can be calculated
 383 in the same way.

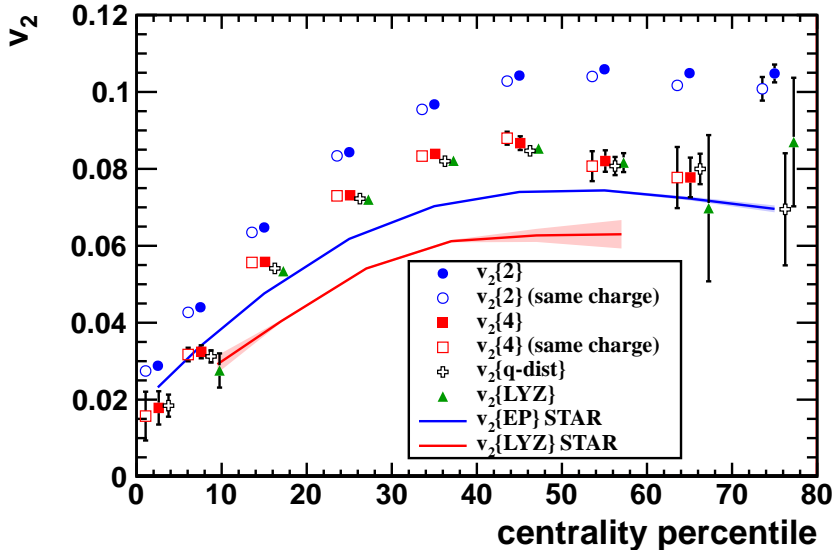


Figure 1.7: The published results of flow with ALICE Pb + Pb $\sqrt{S_{NN}} = 2.76\text{TeV}$ with various measurement methods [7].

384 1.5 Jet quenching

385 In p - p collisions, hard scattered partons fragment into hadrons with high transvers
 386 momentum, also called as jets. However in heavy-ion collisions, the hard scattering
 387 occurs before the formation of QGP, and the scattered partons will experience the en-
 388 tire evolution of the system created in these collisions [42]. These partons will interact
 389 strongly with the created medium and loss their energy, and these features are known
 390 as “jet quenching” [43]. This “jet quenching” is the another strong evidence of the ex-
 391 istence of the QGP, because energy loss in a deconfined matter is believed to be much
 392 stronger than in hadronic matter [43]. “Jet quenching” is usually observed with the sup-
 393 pression of high p_T particles yields though the nuclear modification factor R_{AA} , defined
 394 as like

$$R_{AA}(p_T) = \frac{dN_{ch}^{AA}(p_T)/dp_T}{\langle N_{coll} \rangle dN_{ch}^{pp}(p_T)/dp_T} \quad (1.77)$$

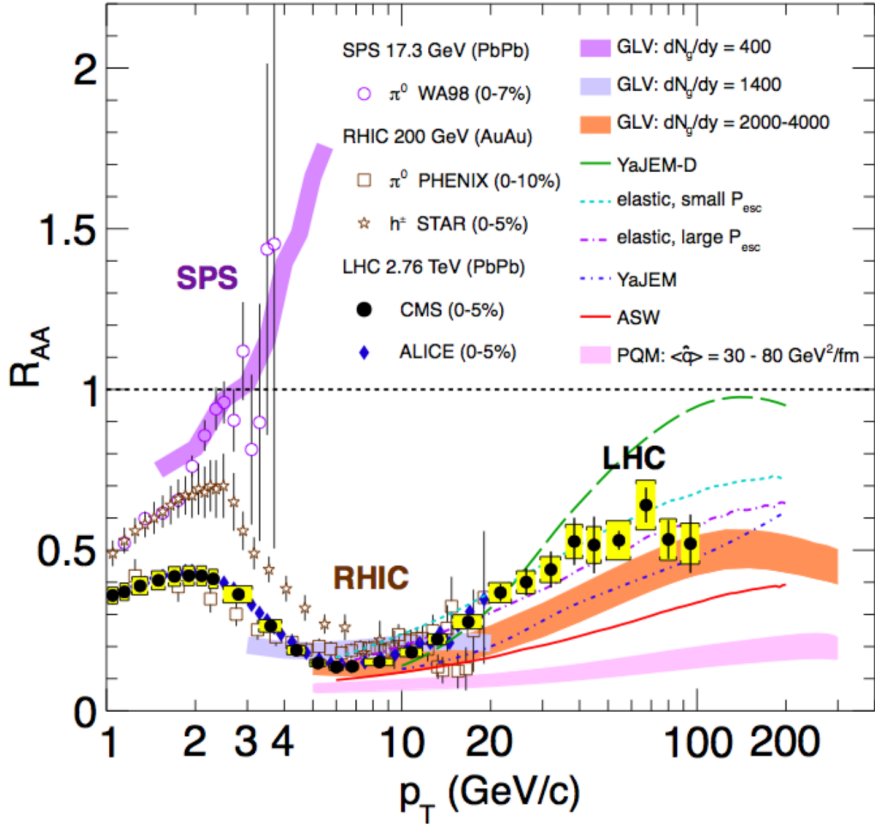


Figure 1.8: Transverse momentum dependence of nuclear modification factor R_{AA} for charged particles produced in heavy ion collisions at SPS, RHIC, and LHC [8].

395 where AA denotes heavy-ion collisions and pp for the p - p collisions. the $dN_{ch}(dp_T)$
 396 refer the number of charged particle produced in each collisions as a function of trans-
 397 verse momentum. The number of binary collisions N_{coll} has been used to compare the
 398 yield of charged particle produced in AA and p - p collisions as scaling factor. This N_{coll}
 399 were calculated by Glauber model, which provide a proper normalization for a given AA
 400 centrality. If there are not any medium effects on AA collisions, the heavy-ion collision
 401 can be regarded as a just simple superposition of nucleon-nucleon collisions (as like p - p)
 402 and nuclear modification factor R_{AA} will be unity. Otherwise, any deviation from unity
 403 of R_{AA} will indicate a certain medium effect of heavy ion collisions.

404 At the energy of SPS, the R_{AA} was slightly lower than unity for $2 < p_T < 3$
405 GeV/c and almost unity for above p_T [44]. However, at RHIC energy, R_{AA} increase
406 monotonically up to $p_T \sim 3$ GeV/c and then start to decrease. Hadron production for
407 $6 < p_T < 8$ GeV/c is suppressed by a factor of 5 in central Au-Au collision when
408 compare to p-p collisions [45, 46].

409 Also, at ALICE energy, R_{AA} published in 2010 with the p_T spectra up to 20 GeV/c
410 shows a slightly stronger suppression (about a factor of 7 observed for the p_T range
411 around 6~8 GeV/c) than previous results was reported. This observation was confirmed
412 by CMS Collaborations, which extended to p_T range up to 100 GeV/c. The R_{AA} mea-
413 surements exhibit a clear increasing trend up to $p_T \sim 40$ GeV/c and then seems to
414 saturate with a value of about 0.5.

415 In addition, the parton energy loss in created medium is increase as the path-length.
416 The path-length which hard scattered parton travels are related to local geometry of
417 create medium. Since in non-central collision the shape of collision regions are formed
418 as like ellipse, the path-length will depend on the azimuthal angles respect to reaction
419 plane angle. For instance, the parton travels along the minor-axis direction (in plane
420 direction) have shorter path-length than the parton emit to the direction of major-axis
421 (out of plane direction). As the results, at high p_T , v_2 is expected to be due to “jet
422 quenching” reflecting the azimuthal asymmetry of the path-length [47].

423 The study of jet energy loss in created medium as function of path-length are per-
424 formed by utilizing $R_{AA}(p_T)$ and $v_2(p_T)$. The path-length as the function of centrality
425 and azimuthal angle respected to 2nd event plane (\sim reaction plane) were estimated from
426 Glauber simulation and details can be found in Appendix C.

427 1.6 Correlation between flow harmonics

428 Since the early 1990s the second order flow(v_2) was studied as one of the most
429 interesting results at RHIC, with Au+Au $\sqrt{S_{NN}} = 200$ GeV collisions. This large signal
430 of the second order “elliptic flow” are explained by the almond shape of the collision
431 overlap region in initial state, and it indicated that a perfect liquid had been made in the
432 early stage of collision. Also detailed studies about flow study report that the fluctuation
433 over event-by-event leads odd number harmonics flow.

434 The anisotropic flow is understood as hydrodynamic response to spatial deformation
435 of the initial density profile. This profile fluctuates event to event due to quantum fluctu-
436 ations of the positions of the constituents inside the colliding nuclei, which implies that
437 the flow also fluctuates [48, 49]. The recognition of the importance of flow fluctuation
438 has led to triangular flow and higher harmonics [50, 51] as well as the correlations be-
439 tween different Fourier harmonics [9]. As the result from ATLAS experiments, it shows
440 that higher order harmonics are sensitive to the η/s [52]. And the v_n distributions carry
441 detailed information about the initial density profile [53, 54].

442 However, difficulties on extracting the shear viscosity in heavy ion has been realized
443 since it strongly depends on the specific choice of the initial conditions [29, 52, 55]. The
444 viscous effects reduce the magnitude of the elliptic flow. Furthermore, the magnitude of
445 η/s used in these calculations should be considered as an average over the temperature
446 history of the expanding fireball while as it is known that η/s of other fluids depends on
447 temperature. In addition, part of the elliptic flow also can originate from the hadronic
448 phase [56, 57, 58]. Therefore, knowledge of both the temperature dependence and the
449 relative contributions from the partonic and hadronic phases should be understood better
450 to quantify η/s of the partonic fluid.

451 The higher harmonics ($n > 3$) are understood as superpositions of linear and nonlin-
452 ear responses, through which they are correlated with lower-order harmonics [59, 60].
453 When the harmonic order is large, the nonlinear response contribution in viscous hydro-
454 dynamics is dominant [59, 60]. The magnitude of the viscous corrections as a function
455 of p_T for v_4 and v_5 are sensitive to ansatz used for the viscous distribution function,
456 δf , a small correction for the equilibrium distribution at hadronic freeze-out when QGP

457 phase has become cool and dilute [61]. Hence the studies of the higher order ($n > 3$) to
 458 lower order (v_2 or v_3) harmonic correlations and their p_T dependence can help to understand
 459 the viscous correction to the momentum distribution at hadronic freeze-out which
 460 is probably the least understood part of hydrodynamic calculations [59, 13].

461 Although there have been detailed studies of single flow harmonics in recent decades,
 462 only a few studies discussed correlation between two different flow harmonics. The difficult
 463 part of studying flow correlation is that there are two kinds of correlation between
 464 flows: the correlation between two flow magnitudes ($v_n - v_m$), and the correlation between
 465 two flow directions. i.e., event plane angles correlation for two different flow
 466 harmonics ($\psi_n - \psi_m$).

467 ATLAS Collaboration measured the correlation between different order event plane
 468 angles with two plane or three correlators by using two (three) subevents symmetric
 469 around $\eta = 0$ with a gap in between. With this method, we can expect the same resolution
 470 for each subevent groups and it provides its own estimate of the event plane
 471 (Fig.1.9). As a result they found a positive correlation between event plane angles as a
 472 function of centrality.

473 CMS Collaboration also reported the correlation between different order event plane
 474 angles by using event plane methods [10], which measure higher-order flow (like v_4, v_5, v_6)
 475 with its own event plane angle, and also with the event plane angle which are measured
 476 from lower harmonics. For example, Fig.1.10 compares the v_4 with its own event plane
 477 angle Ψ_4 (i.e. $v_4\{\Psi_4\}$) and v_4 with 2nd order flow event plane angle Ψ_2 (i.e. $v_4\{\Psi_2\}$).

478 Despite several approaches in studying flow correlations, it is still a challenge to
 479 measure only “direction” and “magnitudes” correlations independently. One observable
 480 proposed by H. Niemi et al. [62] can be used to study the event-by-event fluctuations
 481 and also can measure the correlations between different v_n which directly related to ϵ_n .
 482 They define the linear correlation coefficients $c(a, b)$ as :

$$c(a, b) = \left\langle \frac{(a - \langle a \rangle_{ev})(b - \langle b \rangle_{ev})}{\sigma_a \sigma_b} \right\rangle_{ev} \quad (1.78)$$

483

484 where σ_a is the standard deviation of the quantity a . This correlation function is

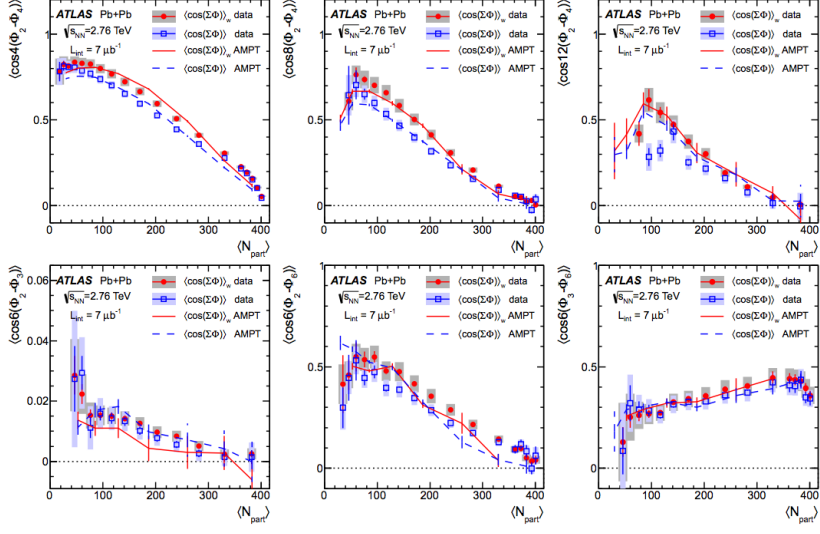


Figure 1.9: The two event plane correlators by using two subevent groups by ATLAS collaboration. $\langle \sum \Phi \rangle \equiv \langle jk(\Phi_n - \Phi_m) \rangle$. Results from the AMPT model calculation via the SP method(solid line) and the EP method(dashed line) for represent for comparison [9].

485 1 (or -1) if a and b are linearly (anti-linearly) correlated and zero in the absence of
486 correlation. From this calculation with hydrodynamic models, correlation between flow
487 harmonics was found. The result indicates that the correlation not only depends on
488 η/s , but is also strongly sensitive to the other properties of the QGP, such as decoupling
489 temperature. Otherwise, the correlation v_2 and v_3 seems sensitive to the initial conditions
490 but insensitive to η/s . Also clear p_T dependence on correlation $c(v_2, v_3)$ was expected.

491 Recently we measured for the first time the new multiparticle observables, the Sym-
492 metric 2-harmonic 4-particle Cumulants (SC), which quantify the relationship between
493 event-by-event fluctuations of two different flow harmonics [63]. The new observ-
494 ables are particularly robust against few-particle non-flow correlations and they provide
495 orthogonal information to recently analysed symmetry plane correlators [64]. It was
496 demonstrated that they are sensitive to the η/s of the expending medium and simultane-
497 ous descriptions of different order harmonic correlations would constrain both the initial

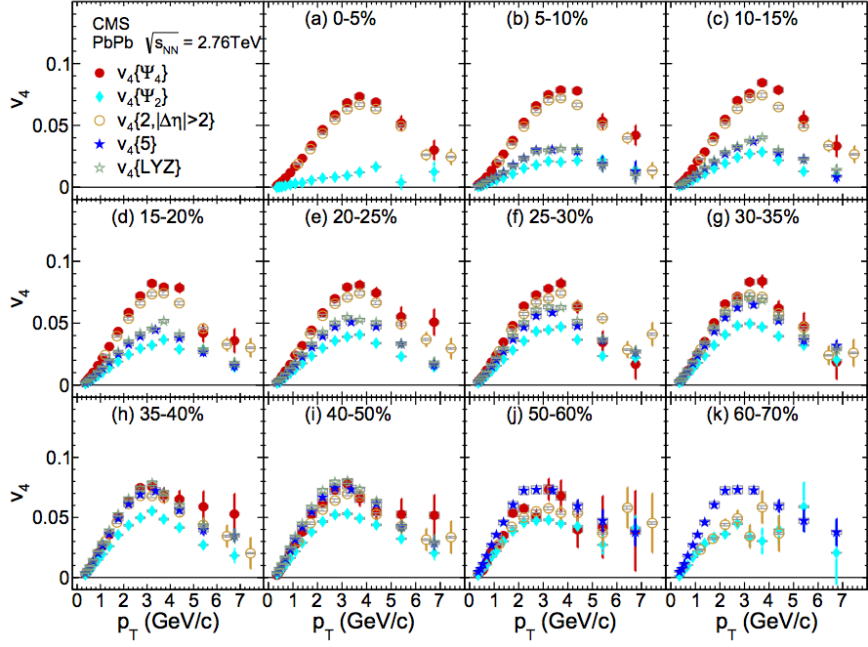


Figure 1.10: Measurement of v_4 with different methods as a function of p_T for the indicated centrality bins. The event plane method with its own event plane (red circle) and the event plane method with 2nd order event plane (blue diamonds) are drawn together.[10]

498 conditions and the medium properties. In this article, we have extended the analysis to
499 higher order Fourier harmonic (up to 5th order) correlations as well as p_T dependence
500 of correlations for the lower order harmonic (v_3-v_2 and v_4-v_2). We also include a sys-
501 tematic comparison to hydrodynamic and AMPT models.

502 From these studies, we can understand that the flow harmonics fluctuate event-by-
503 event due to the fluctuations in the initial matter distribution, including contributions
504 from fluctuations in the positions of the participating nucleons in the nuclei, the partic-
505 ipant plane, determined by the participating nucleons. In addition, such event-by-event
506 fluctuations of the spatial asymmetry generate additional harmonics, which are more
507 sensitive to η/s , because the effect of share viscosity reduces all anisotropic flow coeffi-
508 cients, with a larger decrease for higher order coefficients.

509 **Chapter 2**

510 **Experimental setup**

511 **2.1 Large Hardon Collider**

512 The Large Hadron Collider is the biggest accelerator in the world which was built
513 between 2002 and 2009 at CERN. This powerful particle accelerator was installed in the
514 27km long circular underground tunnel across the border between France and Swiss. It
515 has 16 RF(radio frequency) accelerating cavities and over 1600 superconducting mag-
516 nets. With this accelerator, we can collide protons with a centre-of mass energy up to 14
517 TeV and Pb ions with a centre-of mass energy per nucleon up to 5.5 TeV [65].

518 The protons are first accelerated in linear accelerator LINAC and injected into the
519 BOOSTER at an energy of 50 MeV. The BOOSTER accelerates them to 1.4 GeV before
520 they are sent to the Proton Synchrotron (PS), which further accelerates the protons to
521 25 GeV. From the PS they are sent to the Super Proton Syncrotron (SPS), where they
522 yet again are accelerated, this time to 450 GeV. Finally they are transferred to the LHC
523 ring. At Maximum the 2808 bunches of the protons travel the ring either clockwise or
524 counter-clockwise.

525 Procedures for operating the LHC with lead ions are similar, though with some dif-
526 ferences. The lead ions are produced by heating a highly purified lead sample up to
527 around 550° . This creates a number of charge states, with Pb^{27+} being the dominant
528 one. The ions are accelerated in LINAC 3 to 4.2 MeV per nucleon. Afterwards they are
529 sent through a carbon foil, which strips them to Pb^{54+} . The Pb^{54+} beam is led to the
530 Low Energy Ion Ring (LEIR), where it is accelerated to 72 meV per nucleon, before be-

531 ing transferred to the PS. At the PS, the ions are accelerated up to 5.9 GeV per nucleon.
 532 The ions once again are sent through the foil, stripping them to Pb^{82+} , which is the final
 533 ionization used for collisions. After the PS the now fully stripped ions arrive at the SPS,
 534 where they are accelerated to 177 GeV per nucleon, before being sent into the LHC ring
 535 for acceleration to their collision energy ($0.999999991c$ at $\sqrt{s_{NN}} = 7\text{TeV}$). As in the
 536 proton case, the ion bunches are sent either clockwise or counter-clockwise around the
 537 ring. The collision of lead ions only occur at 3 of the experiment sites, namely ALICE
 538 [66], ATLAS [67], and CMS [68]. The ATLAS and CMS experiments are general pur-
 539 pose detectors used to look for signs of new physics, including the origins of the mass
 540 of elementary particles and extra dimensions. The ALICE detector is designed to study
 541 the properties of the so called quark gluon plasma (QGP) which is believed to have been
 542 created in the first microseconds after the Big Bang. Details will be discussed in the
 543 following chapter.

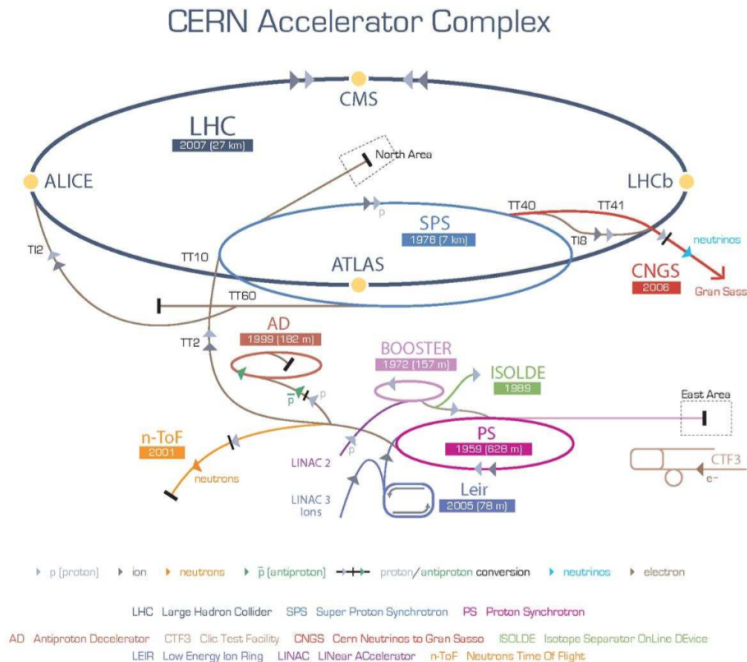


Figure 2.1: Schematic view of Large Hadron Collider

544 2.2 The ALICE experiment

545 ALICE (A Large Ion Collider Experiment) is one of the experiments placed in LHC.
546 The collaboration involves more than a thousand scientists and engineers from 116 insti-
547 tutes and 33 countries. It was designed to study the properties of QCD and to characterize
548 the Quark-Gluon Plasma (QGP). It is the only experiment at LHC which was optimized
549 for the heavy ions collisions.

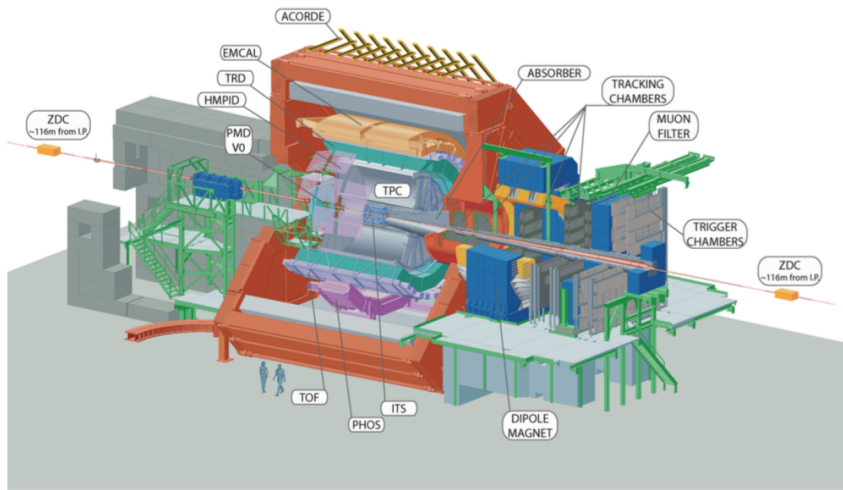


Figure 2.2: Schematic view of ALICE detector [11]

550 The detector is placed in the solenoid magnet from the L3 experiment. This pro-
551 vides a relatively low magnetic field of 0.5 T, which allows to measure low momentum
552 particles corresponding to the so-called soft QCD, as well as more energetic particles
553 from hard processes. Because of the extremely high multiplicity expected in nucleus-
554 nucleus collisions at LHC energies, the design of ALICE was optimized for a multiplicity
555 $dN_{ch}/dy = 8000$. ALICE has an efficient and robust tracking system over a large
556 momentum range, from tens of MeV/c (soft physics) to over 100 GeV/c (jet physics). As
557 some of the tracking detectors are based on drift technologies, they are slower than the
558 detectors operated by the other LHC experiments but can work at the nominal LHC ion
559 beam rate of 10 kHz. A specificity of the ALICE detector over the other LHC experi-

560 ments is its emphasis on hadron and lepton identification (PID). It is achieved over much
561 of the momentum range using most known PID techniques, such as dE/dx energy loss,
562 time-of-flight, transition and Cherenkov radiation, electromagnetic calorimetry, muon
563 filters, and topological decay reconstruction.

564 The detectors in the ALICE experiment are arranged in a classical layered structure
565 around the interaction point as Shown in Figure.2.2. Here is a short description of the
566 main detectors which used in this analysis. Most of description here are taken from the
567 ALICE Technical Design Report (ALICE TDR) [69], and more detail information can
568 be found in CERN document system (CDS) [11].

569 **2.2.1 ITS**

570 The Inner Tracking System (ITS) consists of six layers of silicon detectors with radii
571 few cm as shown Figure.2.5

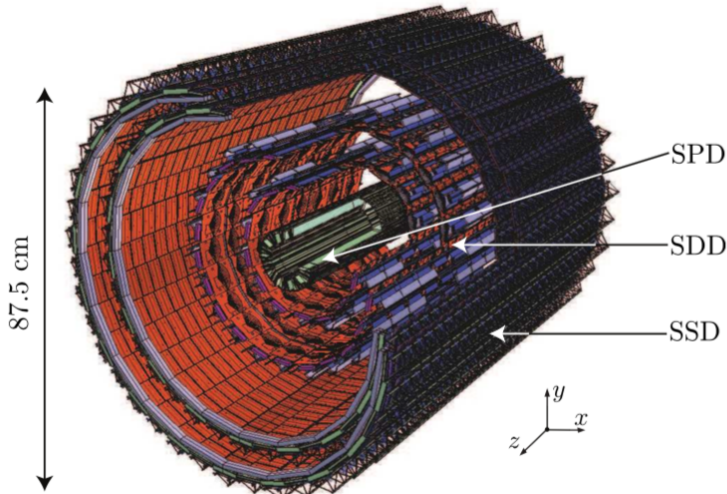


Figure 2.3: ALICE Inner Tracking System(ITS), includes Silicon Pixel Detector(SPD)
and Silicon Drift Detector(SDD) and Silicon Strip Detector(SSD)

572 The main purpose of the ITS is the reconstruction of the primary vertex of the col-
573 lision as well as the reconstruction of secondary vertexes with a resolution better than
574 100 μm in transverse direction. The ITS stand-alone tracking can provide the tracking

575 information for low-momentum particles that do not reach the TPC. The p_T cut-off at
576 nominal field for the two innermost layers is about 35 MeV/c.

577 The two innermost layers, Silicon Pixel Detector (SPD) [70], are based on hybrid
578 silicon pixels which consist of silicon detector diodes with a thickness of 200 μm . The
579 first layer and the second layer are placed at 3.9 cm and 7.6 cm with an acceptance of
580 $|\eta| < 2.0$ and $|\eta| < 1.4$, respectively. The SPD has approximately 10 million channels.
581 The pixel readout chip (ALICE1LHCb) is a mixed- signal ASIC for the readout of 8192
582 pixels. Each pixel cell contains a preamplifier-shaper with leakage current compensa-
583 tion, followed by a discriminator. A signal above threshold results in a logical 1 which
584 is propagated through a delay line during the 6 μs latency time until the arrival of the L1
585 trigger signal. Upon arrival of the L1 trigger, the logical level present at the end of the
586 delay line is stored in the first available buffer location. The outputs of the discriminators
587 in the pixel cells of the ALICE1LHCb chip provide a fast-OR digital pulse when one or
588 more pixels are hit on the chip.

589 The third and forth layer, Silicon Drift Detector (SDD) [71], consist of a 300 μm
590 thick layer of homogeneous high-resistivity silicon. The readout of the SDD is analog,
591 therefore particle identification can be conducted using the information of energy-loss.
592 The SDD has 133,000 channels.

593 The two outermost layers, Silicon Strip Detector (SSD) [72], consist of sensors
594 equipped on both sides with silicon micro-strips. These are arranged under a stereo angle
595 of 35 mrad allowing for a two-dimensional measurement of the track position together
596 with an energy-loss measurement for particle identification. The SSD has approximately
597 2.6 million channels [73].

598 2.2.2 TPC

599 The Time Projection Chamber (TPC) [74] is the main tracking device of the ALICE
600 experiment. It is a large cylindrical gas chamber detector with $\sim 88\text{m}^3$ volume in 0.5
601 T solenoidal magnetic filed parallel to the E field.

602 This detector is designed to have dE/dx resolution better than 5% and a relative
603 p_T resolution better than 1% for momenta of $\sim 1\text{GeV}/c$ and better than 2.5% for mo-

604 ments of $4\text{GeV}/c$, and two track resolution capable of separating tracks with a relative
605 momentum difference of $< 5\text{MeV}$.

606 The TPC is separated by two volumes with the Central Electrode (CE) made of single
607 stretched Mylar foil, and secondary electrons drift toward the end-caps.

608 Volumes are filed with Ne-CO₂-N₂ (90%-10%-5%) gas which is optimized for drift
609 speed, ion mobility, and low diffusion of electrons. Since, Ne-CO₂-N₂ gas have de-
610 pendence of drift velocity on temperature, TPC is aiming for a thermal stability with
611 $\Delta T < 0.1\text{K}$ in the drift volume over the running period.

612 As the gas detector, the TPC field cage has to be operated at very high voltage gra-
613 dients, of about 400V/cm, with a high voltage of 100kV at the central electrode which
614 results in a maximum drift time of about $90\mu\text{s}$.

615 The TPC covers a pseudo-rapidity range of $|\eta| < 0.9$ for full track length within
616 the TPC volume. Also it provides 0 to 2π azimuthal coverage except for the dead zones
617 in the TPC, and it makes the TPC an ideal detector for anisotropic flow analysis, since
618 these inefficiencies in the azimuthal acceptance would result in non-negligible system-
619 atic biases for the azimuthal angle correlations analysis.

620 2.2.3 VZERO

621 The VZERO detectors(also often called V0) [75] are designed with a much larger
622 acceptance, in order to perform as a minimum bias trigger in both proton-proton and
623 Pb-Pb collisions. Furthermore, it is also used, together with the timing information of
624 the collision, for the rejection of beam-gas interactions. The VZERO is also used to
625 determine the event centrality and many of ALICE analyses use centrality determination
626 from VZERO.

627 This consists of two separate arrays of scintillator counters and V0A and V0C,
628 placed on different sides of the central barrel detectors along the beam line. V0A/C
629 are placed asymmetrically with respect to the interaction point. V0A is located 340 cm
630 from the interaction point on the side opposite to the muon arm, while V0C is placed 90
631 cm from the interaction point on the opposite side from V0A. Because of this asymmetry,
632 V0A and V0C have different pseudo-rapidity coverage. The V0A covers pseudo-rapidity

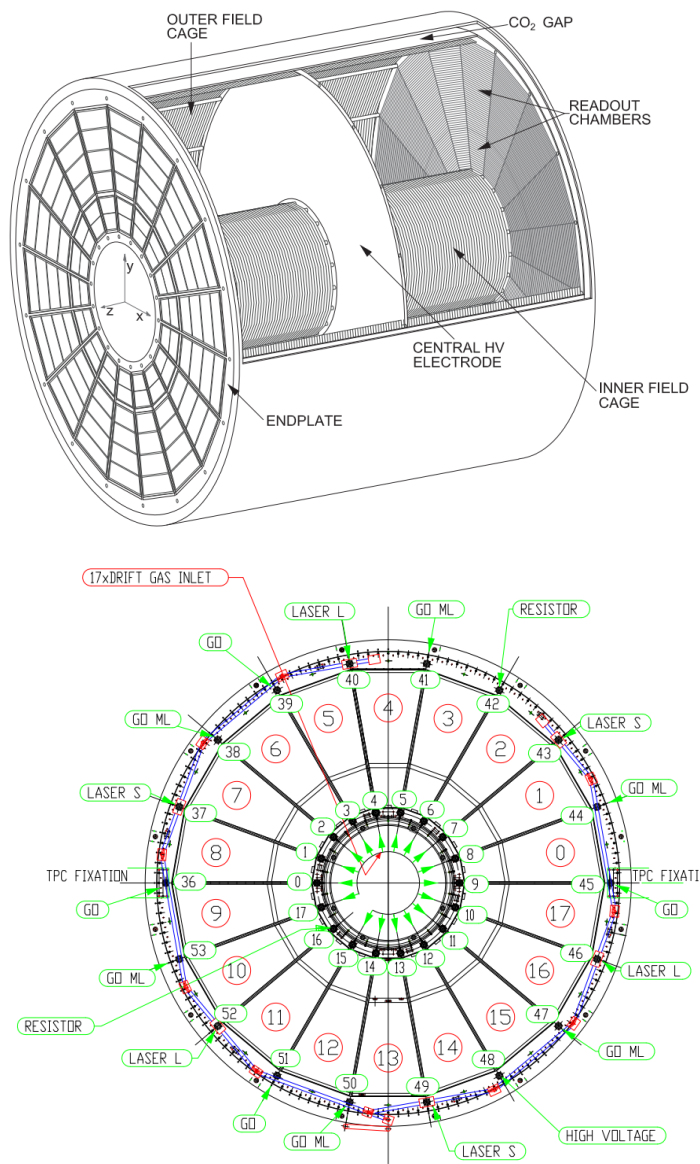


Figure 2.4: ALICE Time Projection Chamber

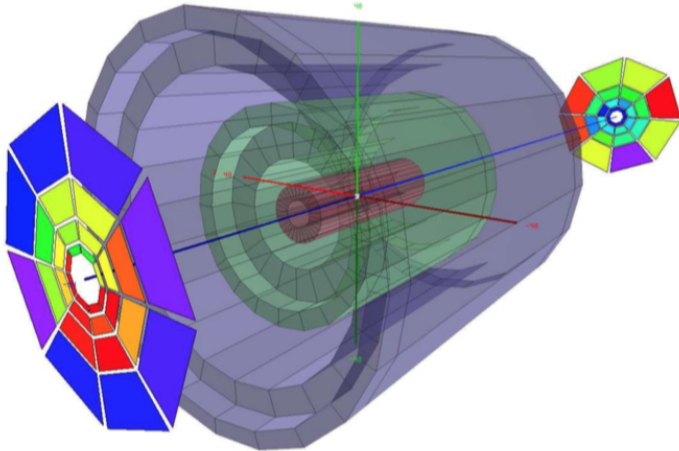


Figure 2.5: ALICE VZERO detectors on both side of TPC

633 range $2.8 < \eta < 5.1$, while V0C covers $-3.7 < \eta < -1.7$.

634 The V0A/V0C are segmented into 32 elementary counters distributed in four rings.
 635 Each ring covers 0.4-0.6 unit of pseudo-rapidity. The rings are divided into eight sectors
 636 of 45° . The elementary counter consists of scintillator material with embedded Wave-
 637 Length Shifting (WLS) fibers. The light from the WLS is collected by clear fibers and
 638 transported to PhotoMultiplier (PM) installed at 3-5 m from the detectors, inside the L3
 639 magnet. The time resolution of each individual counter will be better than 1 ns.

640 Signals from each PMT are sent to an electronics circuit, which delivers two signals.
 641 The first one is sent to a threshold discriminator for the generation of the V0 event
 642 triggers. It is amplified by a factor of about 10. If at least one discriminator is fired
 643 during the time window around the timing of the beam crossing (after 3 ns for V0A, 11
 644 ns for V0C), the V0 event trigger is issued.

645 **2.2.4 Other detectors**

646 **TRD**

647 Transition Radiation Detector (TRD) [76] is placed from 2.9 to 3.8 m from the in-
648 teraction point. It discriminates electrons from pions with high efficiency for momenta
649 about 1 GeV/c by the identification of the transition radiation photons from electrons.
650 Also this detector can provide the trigger signals for electron

651 **TOF**

652 Time Of Flight (TOF) [77] is made of Multigap Resistive Plate Chamber strips
653 (MRPC), which are made by a ten layer double-stack detector with a time resolution
654 of about 40 ps. By measuring the time particles take to reach it, and combined with
655 the tracking information of the TPC, it allows for the identification of pions, kaons and
656 protons

657 **HMPID**

658 High Momentum Particle Identification Detector (HMPID) [78] consists of an array
659 of proximity-focusing Ring Imaging CHerenkov counters (RICH) and covers a pseudo-
660 rapidity range of $|\eta| < 0.6$ and 58° of azimuthal angle. The HMPID discriminates
661 pions and kaons in the range $1 < p_T < 3\text{GeV}/c$ and protons and kaons in the range
662 $2 < p_T < 5\text{GeV}/c$ by means of their Cherenkov rings.

663 **PHOS**

664 PHOton Spectrometer (PHOS) [79] is placed partially opposite to the EMCAL and
665 made of highly segmented electromagnetic calorimeter of lead-tungstenate (PbWO₄ ,
666 PbWO) crystals with a radiation length of $20X_0$. It is used for neutral mesons and direct
667 photon measurements.

668 **EMCAL**

669 ElectroMagnetic Calorimeter (EMCAL) [80] is a lead scintillator sampling calorime-
670 ter that covers an azimuthal angle range of 107° in the rapidity interval $|\eta| < 0.7$ at a

671 radial distance of about 4.5 m from the vacuum tube. The EMCAL is designed for the
672 study of jet-physics and can provide trigger signals for hard jets, photons and electrons.

673 **Muon Spectrometer**

674 Muon Sepctrometer is situated in the forward($-4 < \eta < -2.5$) region on one side
675 of the experiment. It track muons with momentum $p > 4\text{GeV}/c$. And used for the
676 analaysis of quarkonia decaying to the $\mu\mu$.

677 **TZERO**

678 TZERO (T0) [81] detector is designed to determine the collision time. T0 consists of
679 two units, one on each side of the interaction point. Each T0 unit is comprised of quartz
680 Cherenkov radiators glued to photo multiplier tubes. A coincidence between signals in
681 both sides is used for both vertex and time determination

682 **Zero Degree Calorimeter**

683 The Zero Degree Calorimeters (ZDC) [82] are positioned at extremely forward an-
684 gles. Their role is to measure the spectator nucleons from heavy ion collisions, in order
685 to estimate the number of participants, and hence the centrality. Furthermore they are
686 also used to determine the event plane.

687 **2.2.5 Analysis Framework**

688 The ROOT system is an object-oriented framework (written in C++) developed at
689 CERN in the 90's and used by various collaborations worldwide as a starting framework
690 on top of which the specific framework needed for particular collaboration is being built.
691 It provides a full set of features needed for event generation, detector simulation, event
692 reconstruction, data acquisition and data analysis. All features are encoded in a set
693 of about 650 classes grouped in about 40 libraries. A vast majority of ROOT classes
694 inherit from the common base class called TObject, which provides default behavior and
695 protocol (e.g. protocol for the object I/O, error handling, sorting, inspection, printing,
696 drawing, etc.) for all objects in the ROOT system, but the standalone classes which can
697 be used as built-in types are also implemented.

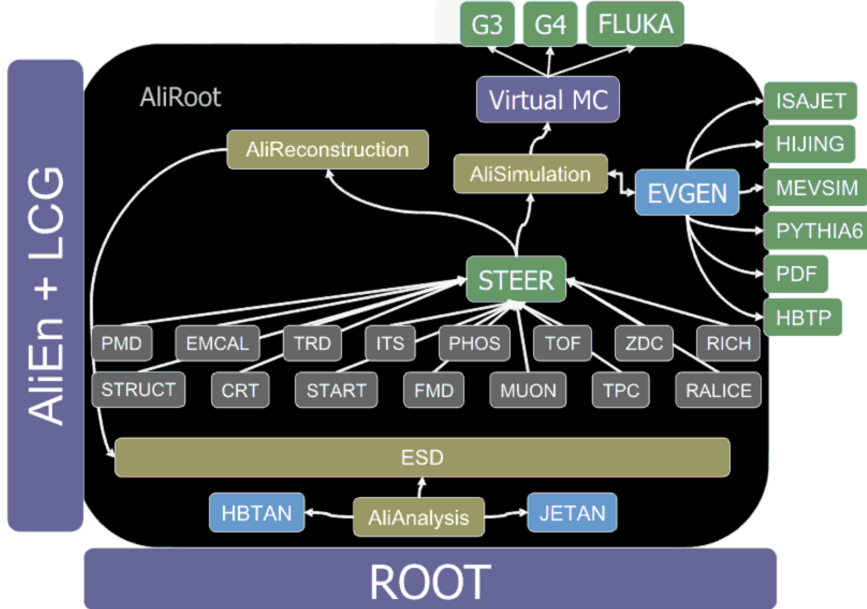


Figure 2.6: Picture of general schema of the AliRoot architecture [12]

698 The AliRoot is the specific version of framework which built on the ROOT system.
 699 It's optimized for ALICE simulation, alignment, calibration, reconstruction, visualization,
 700 quality assurance, and analysis. Most of codes are written in C++ and some parts
 701 are written in Fortran.

702 Also for the large consumption of CPU power, the ALICE analysis framework pro-
 703 vides several distributed computing systems, including the parallel computing (PROOF)
 704 or, Grid. Because of the huge amount of data produced by the ALICE detector ($\sim 2\text{PB}$
 705 per year) [83], the reconstructed events are saved into a worldwide computing center.
 706 The computing center has a distributed hierarchy with Tier 0 to Tier 3, and the ALICE
 707 Virtual Organization (ALICE VO) is made of more than 80 sites. Each site provides
 708 large computing power with physical machines where the software programs can be run.
 709 By using JDL(Job Description Language) and XML(eXecutable Machine Language),
 710 users can use codes with AliRoot over 1500 CPUs at the same time.

711 Chapter 3

712 Data analysis

713 3.1 Data selection

714 In this chapter, we outline the selection criteria applied for this analysis. Basically,
715 we used LHC10 data with pass 2 reconstruction which marked as “good run”. The period
716 of data taking is LHC10h and it is only data sets from heavy ion collisions from 2010.

717 3.1.1 Default cuts and settings

718 The data sample recorded by ALICE during the 2010 heavy-ion run at the LHC
719 is used for this analysis. Detailed procedure of the ALICE data taking can be found
720 in [84, 85, 86]. The Time Projection Chamber (TPC) was used to reconstruct charged
721 particle tracks and measure their momenta with full azimuthal coverage in the pseudo-
722 rapidity range $|\eta| < 0.8$. Two scintillator arrays (V0) which cover the pseudo-rapidity
723 ranges $-3.7 < \eta < -1.7$ and $2.8 < \eta < 5.1$ were used for triggering, and the de-
724 termination of centrality [87]. The trigger conditions and the event selection criteria
725 are identical to those described in [7, 87]. Approximately 10^7 minimum-bias Pb-Pb
726 events with a reconstructed primary vertex within ± 10 cm from the nominal interaction
727 point in the beam direction are used for this analysis. Charged particles reconstructed
728 in the TPC in $|\eta| < 0.8$ and $0.2 < p_T < 5$ GeV/c were selected. The charged track
729 quality cuts described in [7] were applied to minimize contamination from secondary
730 charged particles and fake tracks. The charged particle track reconstruction efficiency
731 and contamination were estimated from HIJING Monte Carlo simulations [88] com-

bined with a GEANT3 [89] detector model, and found to be independent of the collision centrality. The reconstruction efficiency increases from 70% to 80% for particles with $0.2 < p_T < 1 \text{ GeV}/c$ and remains constant at $80 \pm 5\%$ for $p_T > 1 \text{ GeV}/c$. The estimated contamination by secondary charged particles from weak decays and photon conversions is less than 6% at $p_T = 0.2 \text{ GeV}/c$ and falls below 1% for $p_T > 1 \text{ GeV}/c$. With this choice of low p_T cut-off ($p_T > 0.2 \text{ GeV}/c$) we are reducing event-by-event biases from smaller reconstruction efficiency at lower p_T , while the high p_T cut-off ($p_T < 5.0 \text{ GeV}/c$) was introduced to reduce the contribution to the anisotropies from jet particles.

The default estimator for centrality determination in ALICE is obtained from the measurement multiplicity in the VZERO detectors.

Centrality(%)	0-5	5-10	10-20	20-30	30-40	40-50	50-60	60-70
b(fm) AMPT	0.00-3.72	3.72-5.23	5.23-7.31	7.31-8.88	8.88-10.20	10.20-11.38	11.38-12.47	12.47-13.50
b(fm) HIJING	0.00-3.60	3.60-5.09	5.09-7.20	7.20-8.83	8.83-10.20	10.20-11.40	11.40-12.49	12.49-13.49
b(fm) ALICE	0.00-3.50	3.50-4.94	4.94-6.98	6.98-	-9.88	9.81-	-12.09	12.09-

<https://twiki.cern.ch/twiki/bin/viewauth/ALICE/CentStudies>

Also, even though the Inner tracking System (ITS) and the Time Projection Chamber (TPC) were used as the main tracking devices for ALICE experiment, ITS does not have uniform acceptance. On the other hand, corrections for TPC are negligible due to its uniform acceptance. Because of this, we are going to use TPC only cuts in this analysis, in which the tracks are required to have at least 70 reconstructed space point out of the maximum 159 in the TPC and a $\langle \chi^2 \rangle$ per TPC cluster ≤ 4 (with 2 degrees of freedom per cluster)

Only tracks with a transverse distance of closest approach (DCA) to the primary vertex less than 3 mm , both in longitudinal and transverse direction, are accepted to reduce the contamination from secondary tracks (for instance the charged particles produced in the detector material, particles from weak decays, etc.). Tracks with kinks (the tracks that appear to change direction due to multiple scattering, K^\pm decays) were rejected.

756 **3.1.2 Data QA**

757 **η distribution QA**

758 In principle, the multiplicity in each η region should be similar (i.e. $N_{A\text{side}} \sim$
 759 $N_{C\text{side}}$). To confirm this similarity of multiplicity in each η set, we check η distribution
 760 for each centrality bins. Also the multiplicity in $\eta < 0$ region and $\eta > 0$ is compared as
 761 ratio. The ratio between number of multiplicity in $\eta > 0$ subgroup and $\eta < 0$ subgroups,
 762 was fitted with 0th order polynomial function with unity parameter(i.e $y = 1$) run by run.
 763 After fitting, χ^2/NDF was calculated to check for the same multiplicity in both sub-
 764 set groups for each run, each centralities. Fig.3.1 are the η distribution for run number
 765 137135 and the χ^2/NDF test results over all run. The Run number corresponding Run
 766 ID information can be found in Appendix D.0.2

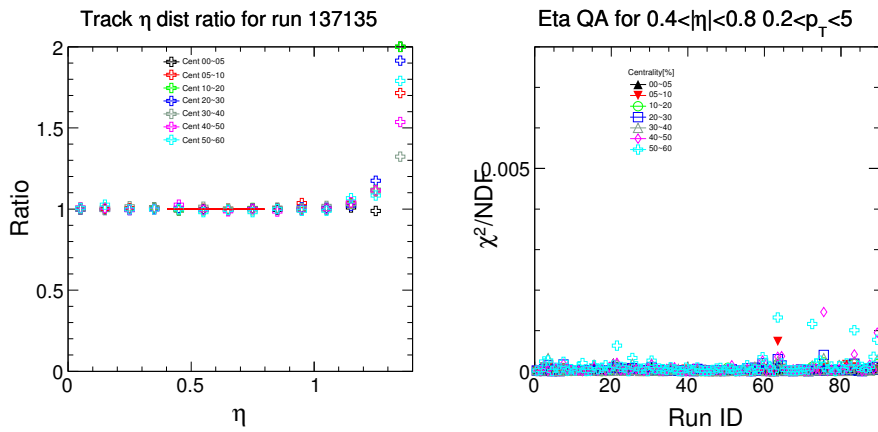


Figure 3.1: Ratio of $dN/d\eta$ for flip over +/- η region(left) and χ^2/NDF for ϕ flatness as function of RunID

767 QA result looks quite good across the runs as shown in figure. χ^2/NDF was lower
 768 than 0.002 for all runs and all centralities. As the results, we might simply assume that
 769 number of multiplicity in each subgroups are same.

770 **ϕ distribution QA**

771 ϕ flatness QA was performed on the ϕ distributions with the data. We fit the distributions with 0th-order polynomial. The distribution was fitted run by run. χ^2/NDF of each run were taken to estimate the flatness of distribution as like η QA method. The fit results are shown in Fig.3.2

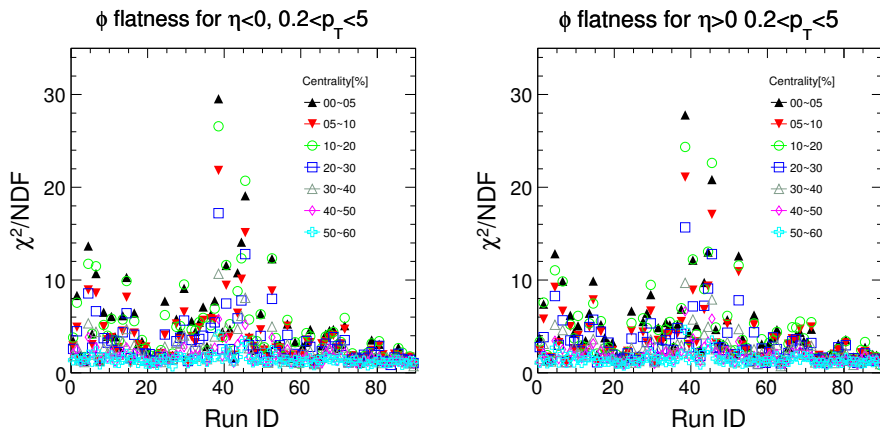


Figure 3.2: χ^2/NDF for ϕ flatness for $\eta < 0$ (left) and $\eta > 0$ (right)

775 As shown in the figure, the flatness (χ^2/NDF of ϕ) of some runs is worse than
776 others. This is considered as a detector effect, and might be affect on our analysis.
777 The effect of these non-uniform ϕ distribution will be treated as systematics and will be
778 covered in systematic chapter.

779 **3.2 Analysis strategy**

780 While from existing measurements an estimate can be placed on the average value
781 of QGP's η/s , both at RHIC and LHC energies, what remains completely unknown is
782 how the η/s of QGP depends on temperature (T). This study has been just initiated
783 by the theorists in Ref. [13], where the first (and only rather qualitative) possibilities
784 were investigated (see Fig. 1 therein). The emerging consensus of late is that it is
785 unlikely that the study of individual flow harmonics v_n will reveal the details of $\eta/s(T)$
786 dependence. In fact, it was demonstrated already in the initial study [13] that different
787 $\eta/s(T)$ parameterizations can lead to the same centrality dependence of individual flow
788 harmonics. In Ref. [90] new flow observables were introduced by the theorists, which
789 quantify the degree of correlation between two different harmonics v_m and v_n . The
790 initial success of these new observables was attributed to their potential to discriminate
791 for the first time the two respective contributions to anisotropic flow development—from
792 initial conditions and from the transport properties of the QGP [90]. Therefore their
793 measurement in turn would enable the experimental verification of theoretical predictions
794 for individual stages of heavy-ion evolution independently. Besides this advantage, it
795 turned out that correlations of different flow harmonics are sensitive to the details of
796 $\eta/s(T)$ dependence [64], to which individual flow harmonics are nearly insensitive [13].

797 For technical reasons, discussed in detail in Refs. [64, 91], the correlations between
798 different flow harmonics cannot be studied experimentally with the same set of observ-
799 ables introduced by the theorists in Ref. [90]. Instead, in [91] the new flow observables
800 obtained from multiparticle correlations, so-called *Symmetric Cumulants (SC)*, were in-
801 troduced to quantify in the most reliable way (i.e. nearly insensitivity to nonflow) the
802 correlation of amplitudes of two different flow harmonics. The technical details are
803 elaborated in Ref. [91], while the first measurements of *SC* observables were recently
804 released by ALICE Collaboration in Ref. [64]. For the convention, we will denote *Sym-*
805 *metric Cumulants* for m th order and n th order as $SC(m, n)$ from now on. This new
806 observable are based on 4-particle cumulant, and defined as

$$SC(m, n) = \langle\langle \cos(m\varphi_1 + n\varphi_2 - m\varphi_3 - n\varphi_4) \rangle\rangle \quad (3.1)$$

$$= \langle v_n^2 v_m^2 \rangle - \langle v_n^2 \rangle \langle v_m^2 \rangle \quad (3.2)$$

807 where double angular brackets indicates that the averaging has been extended from single to all events. Due to the condition that $m \neq n$, a lot of terms which appear in
 808 the general cumulant expansion are non-isotropic and therefore, average to zero for a
 809 detector with uniform acceptance when the averaging is extended to all events.
 810

811 These values can be obtained by multi-particle correlation with q-Cumulants such as

$$\langle\langle 2 \rangle\rangle \equiv \langle\langle e^{in(\phi_1-\phi_2)} \rangle\rangle \equiv \frac{\sum_{i=1}^N (W_{\langle 2 \rangle})_i \langle 2 \rangle_2}{\sum_{i=1}^N (W_{\langle 2 \rangle})_i} \quad (3.3)$$

$$\langle\langle 4 \rangle\rangle \equiv \langle\langle e^{in(\phi_1+\phi_2-\phi_3-\phi_4)} \rangle\rangle \equiv \frac{\sum_{i=1}^N (W_{\langle 4 \rangle})_i \langle 4 \rangle_i}{\sum_{i=1}^N (W_{\langle 4 \rangle})_i} \quad (3.4)$$

812
 813
 814 The choice for the event weights in above equations is not arbitrary and we will
 815 outline in Appendix D. It has a physical meaning which will render the number of com-
 816 binations (i.e. number of distinct 2- and 4-particle combinations one can form for an
 817 event with multiplicity M) as the only correct event weight.

818 For fixed value of v_n and v_m over all events, the $SC(m, n)$ which defined as like
 819 Eq.3.2, is zero by definition. Moreover we can obtain the result in the last line of above
 820 equation not only when v_m and v_n are fixed for all events, but also when event-by-event
 821 fluctuations of v_m and v_n are correlated(or anti-correlated).

822 This $SC(m, n)$ is very efficient observables for measuring flow “magnitude” corre-
 823 lation because it’s free from event-plane which is directly related to “direction” corre-
 824 lation. (Any dependence on the event plane ψ_n and ψ_m is canceled by definition)

825 As a result, the Eq.3.2 holds, the correlation between flow harmonics, and we can
 826 concluded whether finding v_m larger than $\langle v_m \rangle$ in an event will enhance(or reduce) the
 827 probability of finding v_n larger than $\langle v_n \rangle$ in that event.

828 In this analysis, we are going to show $SC(m, n)$ results which can be calculated for
 829 correlation between flow harmonics by using 4- particle cumulants. In addition, we will
 830 show not only $SC(m, n)$ but also going to show *normalized* $SC(m, n)$ (also denote as
 831 $NSC(m, n)$)

$$NSC(m, n) = \frac{SC(m, n)}{\langle v_n^2 \rangle \langle v_m^2 \rangle} \quad (3.5)$$

832
 833 *Normalized symmetric cumulants* (NSC) reflect only the degree of the correlation
 834 which is expected to be insensitive to the magnitudes of v_m and v_n , while $SC(m, n)$
 835 contains both the degree of the correlation and individual v_n harmonics. In Eq.3.5 the
 836 products in the denominator are obtained with two-particle correlations and using a pse-
 837 dorapidity gap of $|\Delta\eta| > 1.0$ to suppress biases from few-particle nonflow correlations.
 838 On the other hand, in the two two-particle correlations which appear in the definition of
 839 $SC(m, n)$ the psedorapidity gap is not needed, since nonflow is suppressed by construc-
 840 tion in SC observable, as the study based on HIJING model has clearly demonstrated in
 841 Ref. [64].

842 However, note that the following Eq.3.6 and 3.7 are not held in this analysis because
 843 of the difference between products $\langle v_m^2 \rangle \langle v_n^2 \rangle$ for denominator and numerator. For the
 844 numerator, since nonflow is suppressed by construction in $SC(m, n)$ we do not apply
 845 any pseudorapidity(η) gap for calculate 4- particle cumulants for all the particles in $|\eta| <$
 846 0.8. But for the denominator, these products were obtained in ALICE with 2- particle
 847 correlations separately with using a pseudorapidity gap of $|\Delta\eta| > 1.0$ to suppress biases
 848 from few particle non-flow correlations. However, other theoretical studies [14] use both
 849 Eq.3.5 and 3.7 for the $NSC(m, n)$

$$\begin{aligned} NSC(m, n) &= \frac{SC(m, n)}{\langle v_n^2 \rangle \langle v_m^2 \rangle} \\ &= \frac{\langle v_n^2 v_m^2 \rangle - \langle v_n^2 \rangle \langle v_m^2 \rangle}{\langle v_n^2 \rangle \langle v_m^2 \rangle} \end{aligned} \quad (3.6)$$

$$= \frac{\langle v_n^2 v_m^2 \rangle}{\langle v_n^2 \rangle \langle v_m^2 \rangle} - 1 \quad (3.7)$$

850 The $SC(m, n)$ provide orthogonal information to recently measured symmetry plane
851 correlators in Refs. [51, 92, 9]. This statement does not exclude the possibility that
852 both set of observables can be sensitive to the same physical mechanisms. In the recent
853 theoretical study [14] it was pointed out that the mechanism giving rise to symmetry
854 plane correlations (nonlinear coupling) can also contribute to symmetric cumulants. As
855 a concrete example it was discussed that the existing correlation due to hydrodynamic
856 evolution between V_4 and V_2^2 (which are vectors in the transverse plane) implies that
857 both the angles and the magnitudes are correlated [14].

858 Interpretation of flow results obtained with multiparticle correlation techniques in
859 small colliding systems, like pp and p–Pb at LHC, remains a challenge. The underlying
860 difficulty stems from the fact that when anisotropic flow harmonic v_n is estimated
861 with k -particle correlator, the statistical spread of that estimate scales to leading order
862 as $\sigma_{v_n} \sim \frac{1}{\sqrt{N}} \frac{1}{M^{k/2}} \frac{1}{v_n^{k-1}}$, where M is the number of particles in an event (multiplicity)
863 and N is total number of events. This generic scaling ensures that multiparticle
864 correlations are precision method only in heavy-ion collisions, characterized both with
865 large values of multiplicity and flow. To leading order the measurements in small sys-
866 tems [93, 94, 95, 96, 97] and the measurements in heavy-ion collisions resemble the
867 same features, which can be attributed to collective anisotropic flow in both cases. How-
868 ever, such interpretation is challenged by the outcome of recent Monte Carlo study [98]
869 for e^+e^- systems in which collective effects are not expected. Nonetheless, in this
870 study to leading order multiparticle correlations exhibit yet again the similar universal
871 trends first seen in heavy-ion collisions, both for elliptic and triangular flow. Therefore,
872 it seems unlikely that the analysis of individual flow harmonics with multiparticle tech-
873 niques will answer whether collective effects can develop and QGP be formed in small
874 systems—instead new observables, like SC, might provide the final answer due to their
875 better sensitivity [90, 64].

876 **Measuring $SC(m, n)$ with Scalar Product method**

877 In this analysis, we are going to show that $SC(m, n)$ also can be calculated by the
878 Scalar Product(SP) method via measuring moments [99] with single η gap. By introduc-

879 ing single η gap between two different sub-event group can avoid auto (self)-correlation
 880 and can suppress non-flow effects. To calculate $SC(m,n)$ with the SP method, we need
 881 to define the (normalized) flow Q -vector such as

$$Q_n = \frac{1}{N} \sum e^{in\varphi} \quad (3.8)$$

882 Then, the flow magnitude can be easily obtained with Q -vector calculation.

$$\langle v_n^{2k} \rangle = \langle V_n^{k*} V_n^k \rangle = \langle Q_{nA}^{*k} Q_{nB}^k \rangle \quad (3.9)$$

883 To avoid self-correlation when calculating v_n^2 , we divide particles into 2 sub event
 884 groups and introduced single η gap between sub event group to suppress non-flow effect.
 885 So main difference between original method and this method is that calculate correlation
 886 with full-particle Q -vector or divided-particle Q -vector, and existence of η gap around
 887 0.

$$\langle v_m^2 v_n^2 \rangle - \langle v_m^2 \rangle \langle v_n^2 \rangle = \langle V_n V_n^* V_m V_m^* \rangle - \langle V_n^k V_n^* \rangle \langle V_m^k V_m^* \rangle \quad (3.10)$$

$$= \langle Re(Q_{An} Q_{Bn}^* Q_{Am} Q_{Bm}^*) \rangle - \langle Re(Q_{An} Q_{Bn}^*) \rangle \langle Re(Q_{Am} Q_{Bm}^*) \rangle \quad (3.11)$$

888 In this analysis, we take denotation “A” for sub-event group which have negative η
 889 range ($-0.4 > \eta > -0.8$) and “B” for positive η range ($0.4 < \eta < 0.8$). Because we
 890 divided into 2 sub groups, particles will not count twice when calculating $Q_{An} Q_{Bn}^*$, but
 891 there are still possible of auto (self) correlation when calculating “ $Q_{An} Q_{Bn}^* Q_{Am} Q_{Bm}^*$ ”,
 892 this effect is probably small but can be corrected with the analytical method.

$$v_n^{2k} v_m^{2l} = \langle Q_{nA}^{*k} Q_{nB}^k Q_{mA}^{*l} Q_{mB}^l \rangle \quad (3.12)$$

893 The auto correlation during above the equation happens because there is a η gap
 894 between $Q_{nA}^{*k} Q_{nB}^k$, and $Q_{mA}^{*l} Q_{mB}^l$ but not between $Q_{nA}^{*k} Q_{mA}^{*k}$ nor $Q_{nB}^k Q_{mB}^l$, the auto
 895 (self) correlation effect can be corrected by changing equation of $SC(m,n)$ from

$$\langle Re(Q_{An}Q_{Bn}^*Q_{Am}Q_{Bm}^*) \rangle - \langle Re(Q_{An}Q_{Bn}^*) \rangle \langle Re(Q_{Am}Q_{Bm}^*) \rangle \quad (3.13)$$

896 to

$$\begin{aligned} & \langle Re(Q_{An}Q_{Bn}^*Q_{Am}Q_{Bm}^*) - \frac{1}{M_B} Re(Q_{Bm+n}^*Q_{Am}Q_{An}) \\ & - \frac{1}{M_A} Re(Q_{Am+n}Q_{Bn}^*Q_{Bm}^*) + \frac{1}{M_A M_B} Re(Q_{Am+n}Q_{Bm+n}^*)) \rangle \\ & - \langle Re(Q_{An}Q_{Bn}^*) \rangle \langle Re(Q_{Am}Q_{Bm}^*) \rangle \end{aligned} \quad (3.14)$$

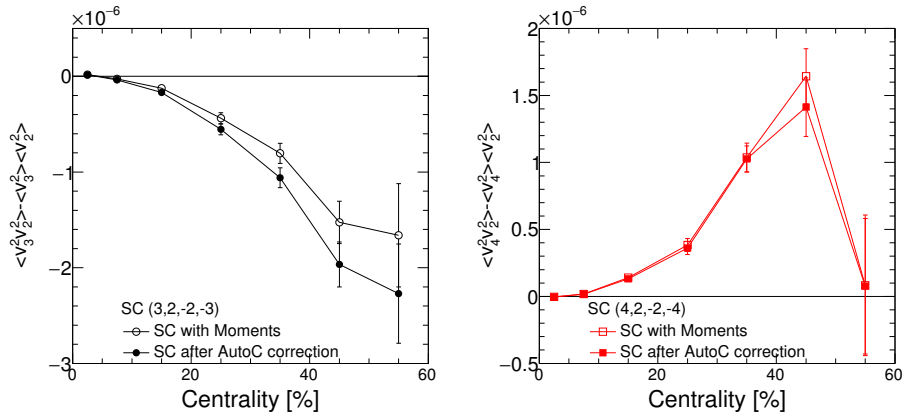


Figure 3.3: Results of $SC(3, 2)$ (left) and $SC(4, 2)$ before auto (self)-correlation correction(open makers) and after correction(closed markers)

897 The detailed results of $SC(m, n)$ and normalized $SC(m, n)$ with various flow har-
 898 monics, and comparison with hydrodynamic calculations and MC simulations, and also
 899 the p_T dependence of $SC(m, n)$ and $NSC(m, n)$ and the difference between two dif-
 900 ferent measuring method (QC vs SP) will be covered in the results chapter.

901 **3.3 Systematics**

902 In this section, the systematic uncertainties of $SC(m, n)$ and $NSC(m, n)$ will be
903 presented. The systematic uncertainties were estimated by varying the event and track
904 selection criteria. All systematic checks described here are performed independently.
905 Each results of $SC(m, n)$ (and also $NSC(m, n)$) with a selected criterion are compared
906 to ones from the default event and track selection described in the previous chapter.
907 The differences between the default results and the ones obtained from the variation
908 of the selection criteria are taken as systematic uncertainty of each individual source.
909 The different ratio were fitted with a 0-th order polynomial as function of centrality
910 to suppress point-to-point statistical fluctuations and to extract the overall systematics.
911 The contributions from different sources were then merged in quadrature to obtain the
912 final value of the systematic uncertainty. The detailed conditions varying for systematics
913 studies were described in the following.

914 **3.3.1 Systematics from Non uniform phi distribution**

915 This section is about systematics uncertainty from the non-uniform efficiency of de-
916 tector performance. In principle, the ϕ distribution of produced particle should be flat
917 over all events unless detector effect. But in our data, as seen in the previous section in
918 data QA (see figure.3.2), the distribution of the transverse angle of particle produced is
919 not perfectly uniform due to detector effects like inefficiency or dead-zone area. And
920 these non-uniform ϕ distributions vary run-by-run, and it is not easily corrected by sim-
921 ple weight correction for specific ϕ angle.

922 This non-uniform ϕ distribution might change the final results of $SC(m, n)$ and
923 should be taken into systematic uncertainty. The simplest and basic approach to check
924 the effect of non-uniform distribution is categorize run groups into two sub groups to
925 have good ϕ distribution, and for the other group to have bad ϕ distribution. Then
926 measure the $SC(m, n)$ values with each sub groups independently and calculated the
927 difference between them as the systematic uncertainty. However, to use this methods,
928 we need to have almost same number of events for each groups. Even though we have
929 similar number of events for each groups, we are going to have larger statistical error

930 because of half of events in this way.

931 In this analysis, to check systematic uncertainties from non-uniform ϕ distribution,
932 we use AMPT simulation which has better match to data than any other existing models.
933 We measure $SC(m, n)$ with the large statistics AMPT dataset which has flat ϕ distribu-
934 tion, and impose non-uniform ϕ distribution from data and calculate the difference be-
935 tween original AMPT and modified AMPT as systematic uncertainty from non-uniform
936 ϕ distribution.

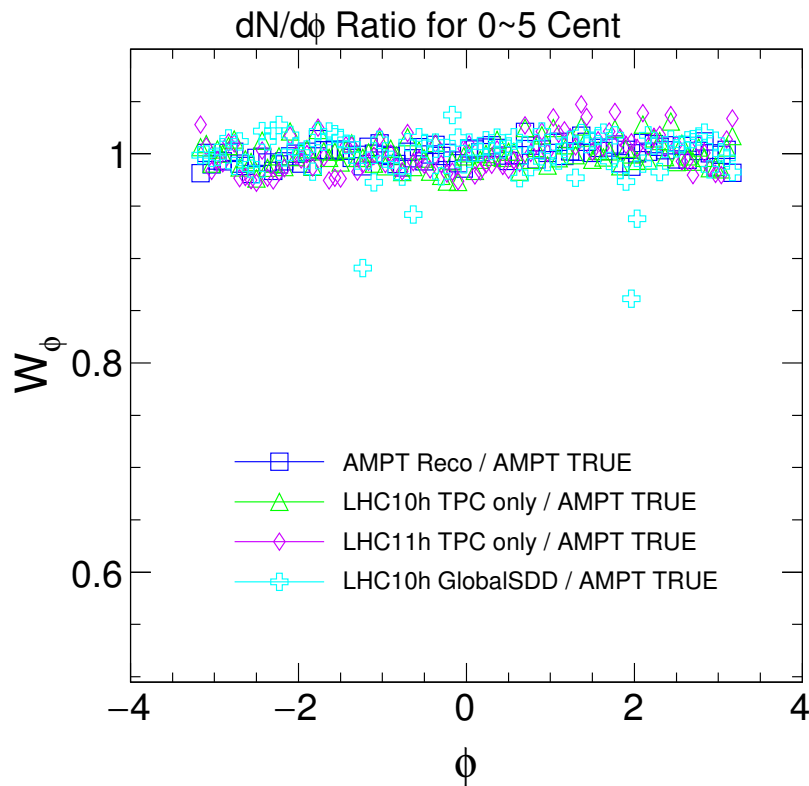


Figure 3.4: Scaled ratio of $dN/d\phi$ distribution of ALICE LHC10h dataset to flat distribution (AMPT True). The reconstructed AMPT, and LHC11h with TPC only track cut, and LHC10h with Global SSD track cut were also drawn together for comparison.

937 The non-uniform ϕ distribution which is taken from ALICE LHC10h data are shown
938 in Fig.3.4. We use TPC only track cut, which have better ϕ distribution, but also LHC10h

939 with Global SDD and LHC11h distribution were shown together for comparison. As
940 seen in figure, the data from LHC10h period have worse flatness than AMPT simulation.
941 It becomes even worse in GlobalSSD track cut or LHC11h period data because of some
942 detector problems. (Some of SDD clusters in ITS detector were dead in 2010, and there
943 was reconstruction efficiency issue with TPC detector in 2011 data taking) The results
944 with AMPT data and modified AMPT data were calculated together and the difference
945 between them was taken into systematic uncertainties.

946 **3.3.2 Systematics from Event selection**

947 Following is the list of item for systemic uncertainty study about event selections.

948 **Z-vertex cut**

949 Because of limited acceptance of ALICE detector, primary vertex position along the
950 longitudinal direction is important to ensure for the uniform pseudo-rapidity distribution
951 over all events. The z-vertex distribution of ALICE LHC10h events are shown in Fig.3.5.
952 As described in previous chapter, the reconstructed vertex position in beam axis (z-
953 vertex) is required to be located within 10 cm of interaction point (IP). Since the different
954 z-vertex position may have an effect on effective η range. So these Z-vertex cut criteria
955 are important to ensure for the flat η distribution over all events. Instead of using the
956 original vertex range cut ($|z| < 10$ cm), we tried to reduce $|z| < 8$ cm for systematic
957 study.

958 **Magnetic polarization**

959 The events which we analyzed were recorded with two settings of the magnetic field
960 polarities, namely (++) and (-). For the default, we used all the events from both polar-
961 ized magnetic fields. The configuration of magnetic polarizations consist of almost the
962 same number of events. We measured the $SC(m, n)$ results from (++) or (-) categorized
963 events and compare to the default one.

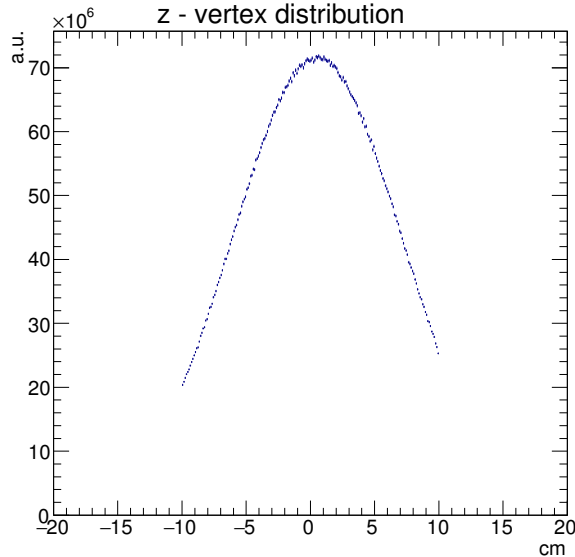


Figure 3.5: Z-vertex distribution of ALICE Pb + Pb $\sqrt{S_{NN}} = 2.76$ TeV with minimum bias triggered events

964 **Centrality determination**

965 The centrality of the given collision can be determined by various detectors and set-
 966 tings. By the default, the multiplicity of the VZERO detector(Both V0A and V0C) is
 967 used for centrality determinations with better than 2% of resolution. Another method of
 968 determine event centrality were using the multiplicity of tracks estimated by the stan-
 969 dalone TPC tracking or tracklet from SPD detector independently which have slightly
 970 worse resolution. We use these methods to study systematic uncertainty from centrality
 971 determination.

972 **Cut on outliers**

973 The outlier is an observation point that is different from other observations. In
 974 LHC10h datasets, there are some events which have many more TPC tracks than Global
 975 reconstructed tracks. These outliers is coming from pile-up like events or indicate ex-

976 experimental error. These kind of outliers usually are discarded from the data sets. In these
 977 case, we excluded the events which have Multiplicity of TPC except following criteria

$$32.1 + 1.59 \times M_{Global} < M_{TPC} < -40.3 + 1.22 \times M_{Global} \quad (3.15)$$

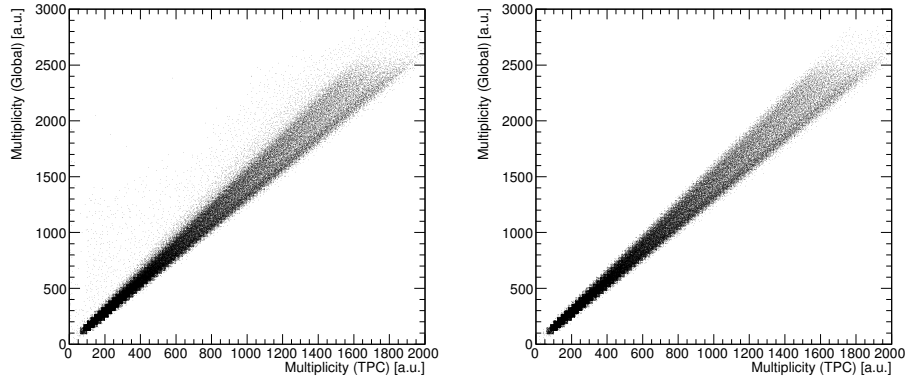


Figure 3.6: The 2-dim distribution of TPC multiplicity and Global multiplicity. Left is the before exclude outlier(left) and right figure is after exclude outlier(right) events.

978 3.3.3 Systematics from Track selection

979 Following is the list of item for systematic uncertainty study form track selections.

980 **Track filter bit**

981 As can see the Fig.3.7, ϕ flatness vary as track selection filter cuts, and it might
 982 affect the results of $SC(m, n)$ which is sensitive to ϕ distribution. This incompleteness
 983 of ϕ distribution comes from the limited precision with the detector performance. And
 984 each track filter cuts were evaluated by the thresholds on parameters used to select the
 985 tracks at the reconstruction level. Usually TPC only track cuts have relatively good(flat)
 986 ϕ distribution than GlobalSDD cut, but more fake and secondary tracks are included.
 987 Also GlobalSDD cut gives two small holes in ϕ distribution.

988 To estimate systematic uncertainty from the track selection filter cut, we measure the
 989 results from different track selections and compare with the default setting.

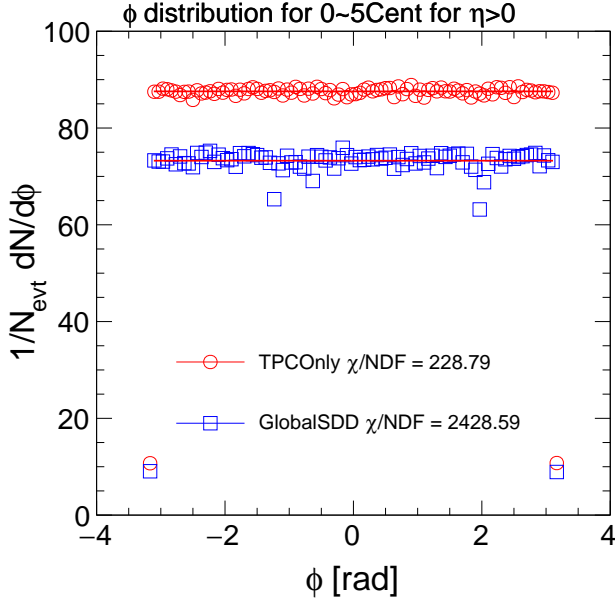


Figure 3.7: χ/NDF of $dN/d\varphi$ distribution from ALICE LHC10h data with TPC only track selection filter and Global SDD filter.

cut	filter bit	comments
TPCOnly	128 (7)	GetStandardTPCOnlyTrackCuts() + SetMinNClustersTPC(70)
GlobalSDD	96 (5 6)	GetStandardITSTPCTrackCuts2010() with requiring the first SDD cluster instead of an SPD cluster

Table 3.1: ALICE Track selection filter conditions

990 Charge combination

991 We used 4p- and 2p- correlation to measure $SC(m, n)$. The multiparticle cumu-
 992 lants are expected to remove non-flow effect by cancellation each other, however it is
 993 hard to prove there is perfectly absense of non-flow effects in $SC(m, n)$. To estimate
 994 remain non-flow effects, such as re-reinteraction with other particles in the system after

995 leaving the domain, the modification of the jet-like two-particle correlations, resonance
996 decays, and final state interactions (particularly Coulomb effects). Such flowing cluster
997 contributes to cumulants by definition as being genuine four particle correlations, how-
998 ever, due to charge conservation, we will have in the cluster always particles of opposite
999 charge. Therefore, by performing an independent analysis only with like-sign charges,
1000 we are estimating the contribution from flowing clusters.

1001 **Efficiency correction**

1002 The correction to p_T dependent efficiency were also tested, and taken into systematic
1003 uncertainty. Because of incompleteness of track reconstruction, correction steps are
1004 necessary to trace back from reconstructed tracks to the orignally generated particles
1005 from the collisions. Usually this study were conducted with a Monte Carlo simulation
1006 such as HIJING for Pb+Pb colisions and PYTHIA for the p - p collisions. The single
1007 track reconstruction efficiency, and contamination form the secondary particles were
1008 shown in FIg.3.8

1009 **3.3.4 Overall systematic uncertainty**

1010 All systematic uncertainty checks discussed in this analysis were included in the final
1011 systematic uncertainty. All individual checks are performed independently and these all
1012 systematics were combined in quadrature to obtain the final uncertainty. The tabulated
1013 systematic uncertainties are listed below tables.

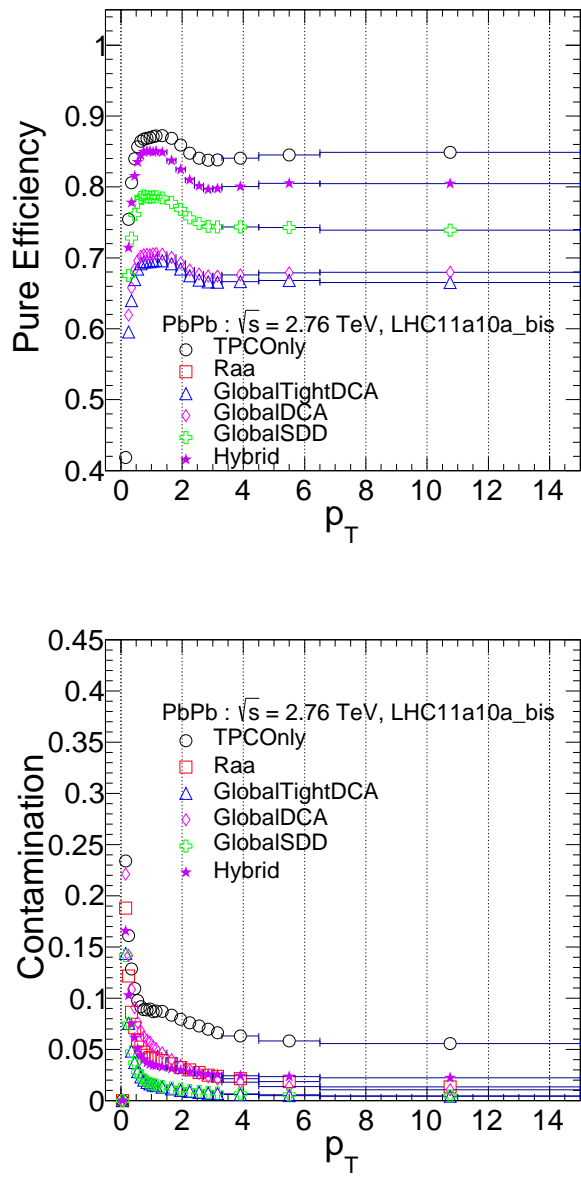


Figure 3.8: Tracking efficiency of single particle reconstruction as a function of p_T (left) and contamination of single particle as a function of p_T (right) for ALICE with various track selection filter

Type [%]	SC(3,2)	SC(4,2)	SC(5,2)	SC(5,3)	SC(4,3)
Non-uniform ϕ distribution	< 1	1.2	9.5	17.3	11.3
Track filter bit selection	8.4	4.9	9.1	9.1	11.9
Efficiency correction	3.1	4.4	1.5	1.7	1.3
Z-vertex cut	2.1	1.5	2.1	1.9	3.0
Charge combination	4.5	12.1	18.5	19.5	6.8
high multiplicity outliers	< 1	2	2.1	2.1	< 1
Magnetic field polarization	2.1	2.7	1.3	1.5	1.1
Centrality determination	< 1	< 1	3.1	7.6	1.5
Overall	10.8	17.9	22.8	28.8	18.4

Table 3.2: Systematic uncertainties of $SC(m, n)$. Overall systematics are quadratically merged results of each individual systematic error

Type [%]	NSC(3,2)	NSC(4,2)	NSC(5,2)	NSC(5,3)	NSC(4,3)
Non-uniform ϕ distribution	< 1	1.1	7.5	15.3	12.4
Track filter bit selection	7.3	4.9	8.4	12.1	11.1
Efficiency correction	3.1	3.4	1.5	1.7	1.3
Z-vertex cut	2.1	1.5	2.1	1.9	3.0
Charge combination	2.3	5.1	18.2	19.5	6.1
high multiplicity outliers	< 1	2	2.1	3.1	< 1
Magnetic field polarization	2.1	2.7	3.6	5.1	4.1
Centrality determination	< 1	< 1	1.4	1.5	< 1
Overall	9.1	8.1	22.2	28.3	18.5

Table 3.3: Systematic uncertainties of $NSC(m, n)$. Overall systematics are quadratically merged results of each individual systematic error

1014 **Chapter 4**

1015 **Results**

1016 **4.1 $SC(m, n)$ Results**

1017 **4.1.1 $SC(3, 2)$ and $SC(4, 2)$**

1018 The centrality dependence of $SC(4, 2)$ and $SC(3, 2)$ are presented in Fig.4.1. Positive values of $SC(4, 2)$ are observed for all measured centralities. This suggests a positive correlation between the event-by-event fluctuations of v_2 and v_4 . It also indicates that finding v_2 larger than average($\langle v_2 \rangle$) in an event enhances the probability of finding v_4 larger than average($\langle v_4 \rangle$) in that event. On the other hand, the negative results of $SC(3, 2)$ over all measured centralities show the anti-correlation between v_2 and v_3 flow harmonic magnitudes, which further implies that finding v_2 larger than average($v_2 > \langle v_2 \rangle$) enhancing the probability of finding smaller v_3 than average($v_3 < \langle v_3 \rangle$).

As discussed and evaluated order-by-order in [100], general cumulant formalism is applicable to any correlators eliminating non-flow correlations up to order $2k$ by means of a cumulant expansion. Also when compared with HIJING simulation data[101] does not include anisotropic collectivity, but has azimuthal correlations due to jet production (non-flow effects)[102]. It is found that both

$$\langle\langle \cos(m\varphi_1 + n\varphi_2 - m\varphi_3 - n\varphi_4) \rangle\rangle = \langle v_m^2 v_n^2 \rangle$$

and

$$\langle\langle \cos[m(\varphi_1 - \varphi_2)] \rangle\rangle \langle\langle \cos[n(\varphi_1 - \varphi_2)] \rangle\rangle = \langle v_m^2 \rangle \langle v_n^2 \rangle$$

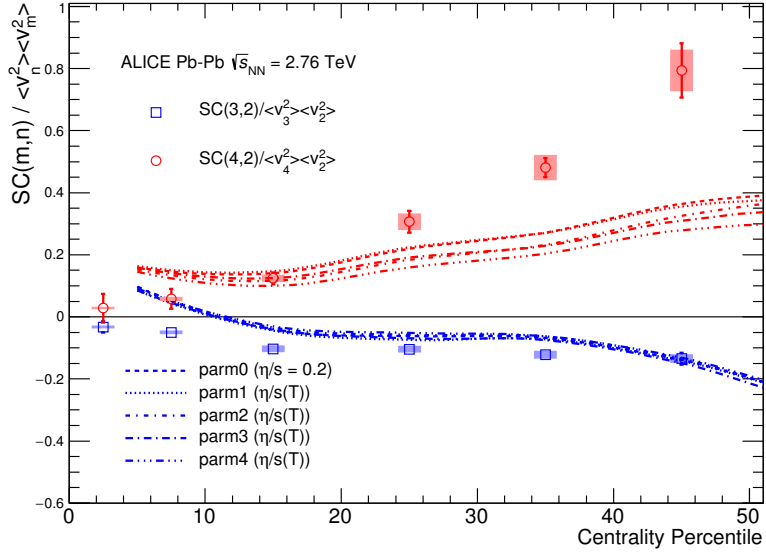
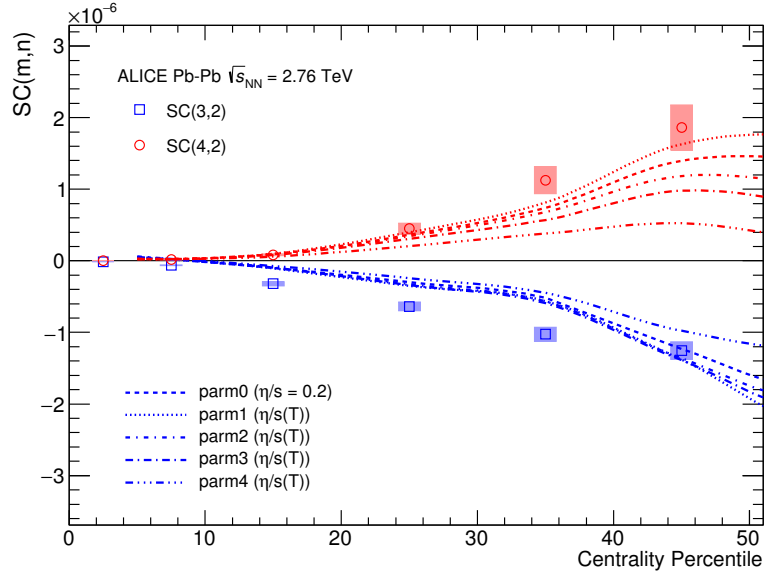


Figure 4.1: The results of $SC(3,2)$ (blue) and $SC(4,2)$ (red) with ALICE Pb+Pb $\sqrt{s_{NN}} = 2.76$ TeV as function of collision centrality (Top). The $NSC(m, n)$ results which scaled with $\langle v_m^2 \rangle \langle v_n^2 \rangle$ were placed in Bottom. The dashed lines are hydrodynamic prediction from H. Niemi with various η/s parametrizations [13]

1026 are not zero. However, the calculation of $SC(m, n)$ from HJING are compatible with
 1027 zero for all centralities (even for higher p_T as shown in Fig.4.2) and it suggest that the
 1028 $SC(m, n)$ are not coming from non-flow effects and insensitive to non-flow correlations.

1029 Moreover, systematics study using the same charge combination pair technique has
 1030 been done, which is another approach to estimate the non-flow effect. By using like-sign
 1031 track selection method, we can eliminate “flow cluster” effects due to charge conserva-
 1032 tion. As the result of systematic study, it was found that the difference between like-sign
 1033 and all charged measurements are only few% level and also we can found same trends
 1034 (positive and negative correlation for $SC(4, 2)$ and $SC(3, 2)$) in like-sign results. This
 1035 further illustrates that non-zero values of $SC(m, n)$ cannot be explained by non-flow
 1036 effect, but confirms the existence of correlation (and anti-correlations) between v_n and
 1037 v_m harmonics.

1038 The $SC(m, n)$ results show that the correlation strength in both $SC(m, n)$ and
 1039 $NSC(m, n)$ increase non-linearly up to centrality 50%.

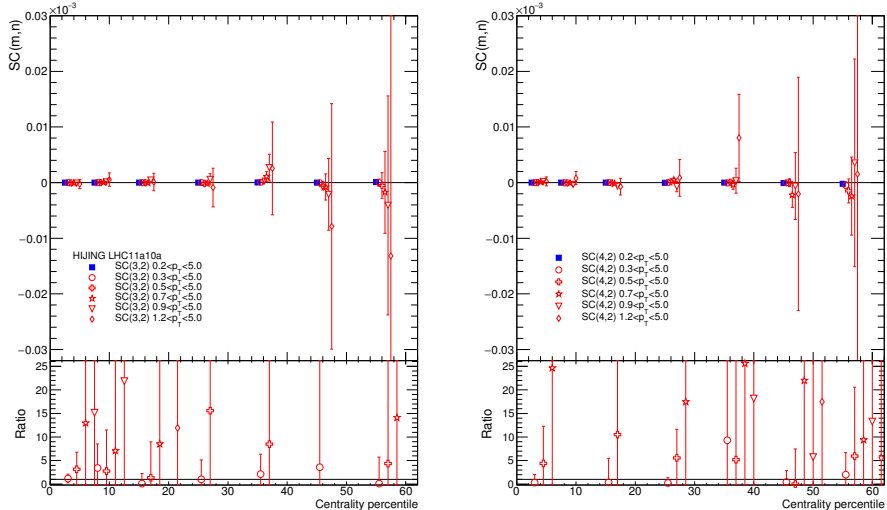


Figure 4.2: Result of $SC(3,2)$ and $SC(4,2)$ with HIJING simulations. Defaults($0.2 < p_T < 5.0 GeV/c$) are drawn as full square with blue color, and different minimum cut conditions are listed in legend. A small shifts along the x axis were applied for better visibility

1040 **4.1.2 Model Comparison**

1041 Various models have been used in this study. The HIJING model [88, 100] was
1042 used to estimate the strength of non-flow correlations (typically few-particle correlations
1043 insensitive to the collision geometry) as described in previous section.

1044 The $SC(m, n)$ from hydrodynamic prediction with pQCD, where the initial energy
1045 density profiles are calculated using a next-to-leading order perturbative-QCD+saturation
1046 model [103, 104] + various shared viscosity η/s parameterizations were performed by
1047 H. Niemi [13]. The subsequent spacetime evolution is described by relativistic dissipa-
1048 tive fluid dynamics with different parametrizations for the temperature dependence of
1049 the shear viscosity to entropy density ratio $\eta/s(T)$. Each of the $\eta/s(T)$ parametrizations
1050 is adjusted to reproduce the measured v_n from central to mid-peripheral collisions.

1051 The fluid hydrodynamic predictions with the different parameterizations for the tem-
1052 perature dependence of the shear viscosity to entropy ratio $\eta/s(T)$ are shown shown in
1053 Figure 4.1 as dashed line. Roughly the hydrodynamic calculations capture qualitatively
1054 the centrality dependence, but not quantitatively. Both $SC(3, 2)$ with data and hydro-
1055 dynamics have negative values for all centralities, while $SC(4, 2)$ results have positive
1056 values over all measured centralities. However, there is no single centrality for which
1057 a given $\eta/s(T)$ parameterization describes both $SC(3, 2)$ and $SC(4, 2)$ simultaneously.
1058 On the other hand, the same hydrodynamic calculations capture the centrality depen-
1059 dence of the individual v_n quantitatively [105].

1060 $NSC(3, 2)$ and $NSC(4, 2)$ are also compared to the same model on the right in
1061 Fig. 4.1. While $NSC(3, 2)$ does not show sensitivity to different $\eta/s(T)$ parameteri-
1062 zations, $NSC(4, 2)$ exhibit much better sensitivity than $NSC(3, 2)$ observable and the
1063 individual flow harmonics [13]. These findings indicate that $NSC(3, 2)$ observable is
1064 sensitive mainly to the initial conditions, while $NSC(4, 2)$ observable is sensitive to
1065 both the initial conditions and the system properties, which is consistent with the predic-
1066 tion from [90].

1067 However, the sign of $NSC(3, 2)$ is positive in the models in 0-10% central colli-
1068 sions while it is negative in data. In the most central collisions the anisotropies origi-
1069 nate mainly from fluctuations, i.e. the initial ellipsoidal geometry characteristic for mid-

1070 central collisions plays little role in this regime. Hence this observation will help to
1071 understand the fluctuations in initial conditions better.

1072 $NSC(4, 2)$ observable shows better sensitivity for different $\eta/s(T)$ parameteriza-
1073 tions, i.e. medium property but the model cannot describe the centrality dependence
1074 nor the absolute values. These observed distinct discrepancies between data and models
1075 might indicate that the current understanding of initial conditions used in the model need
1076 to be revisited to further constrain the $\eta/s(T)$, considering the difficulties on separating
1077 the role of the η/s from the initial condition to the final state particle anisotropies [29,
1078 55]. Hence the use of $SC(m, n)$ and $NSC(m, n)$ can provide new constraints on the
1079 detailed modeling of the initial-state condition and the fluctuations of the medium cre-
1080 ated in heavy ion collisions and the better constraints on the initial-state conditions will
1081 certainly improve the uncertainties of determining $\eta/s(T)$.

1082 The normalized $SC(m, n)$ were compared to MC-Glauber using wounded nucleon
1083 (WN) and binary collisions (BC) weights models to check linear and non-linear response
1084 from initial geometry. Assuming only linear response $v_n \propto \epsilon_n$, we expect that the nor-
1085 malized $SC(m, n)$ evaluated in coordinate space are able to capture the measurement of
1086 centrality dependence of normalized $SC(m, n)$ in the momentum space. In this case the
1087 correlation between the n th and m th order harmonics were estimated with calculation
1088 of $SC(m, n)$ in the coordinate space as define as

$$SC(m, n)_\epsilon / \langle \epsilon_n^2 \rangle \langle \epsilon_m^2 \rangle \equiv (\langle \epsilon_n^2 \epsilon_m^2 \rangle - \langle \epsilon_n^2 \rangle \langle \epsilon_m^2 \rangle) / \langle \epsilon_n^2 \rangle \langle \epsilon_m^2 \rangle \quad (4.1)$$

1089 Where the ϵ_n is the n th order coordinate space anisotropy as defined in [50]. Since
1090 there are two different scenarios of the MC-Glauber model, we tested with both wounded
1091 nucleon (WN) and binary collisions (BC) weights and results are shown in Fig.4.3.
1092 An increasing trend from central to peripheral collisions with different sign has been
1093 observed and there is a large deviation of $NSC(4, 2)$ between ALICE data and MC-
1094 Glauber model. This deviation increase from central to peripheral collision regions and
1095 this might indicate the contribution of the non-linear response of initial condition though
1096 hydrodynamic evolution. Moreover, the MC-Glauber model with $NSC(3, 2)$ describes
1097 better the data than $NSC(4, 2)$, because the $NSC(3, 2)$ appears to be sensitive only to

1098 initial conditions and not sensitive to hydrodynamic properties (η/s).

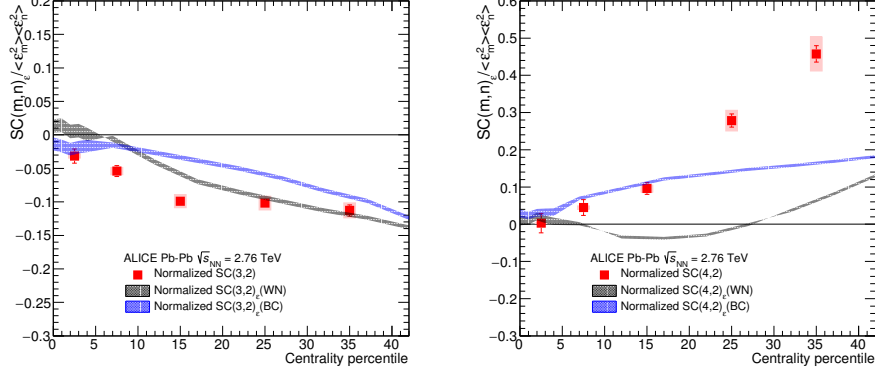


Figure 4.3: Normalized $SC(m, n)$ (red) with the comparison to MC-Glauber models using wounded nucleon (WN) and binary collisions (BC) weights.

1099 The $SC(m, n)$ with AMPT [106, 107, 108] simulation with various configurations
1100 was also tested. The configuration of AMPT are listed in Table.4.1.2. With changing
1101 configuration of AMPT simulations, we may estimate the effects of initial conditions
1102 and finite states effects.

1103 Even though thermalization could be achieved in collisions of very large nuclei
1104 and/or at extremely high energy, the dense matter created in heavy ion collisions may
1105 not achieve full thermal or chemical equilibrium as a result of its finite volume and
1106 energy. To address such non-equilibrium many-body dynamics, AMPT has been devel-
1107 oped, which includes both initial partonic and final hadronic interactions and the tran-
1108 sition between these two phases of matter. For the initial conditions, the AMPT model
1109 uses the spatial and momentum distributions of hard minijet partons and soft strings
1110 from the HIJING model [88, 100]. The AMPT model can be run in two main config-
1111 urations, the default and the string melting model. In the default version, partons are
1112 recombined with their parent strings when they stop interacting. The resulting strings
1113 are later converted into hadrons using the Lund string fragmentation model [109, 110].
1114 In the string melting version, all the excited strings that are not projectile and target
1115 nucleons not experiencing any interactions are converted to partons according to the fla-

vor and spin structures of their valence quarks. The advantage of this choice is that the AMPT model with string melting reduces to HIJING results in the absence of partonic and hadronic interactions as these partons would then find each other as closest partners at the same freeze-out time and thus coalesce back to the original hadron. In the AMPT model with string melting, the initial strings are melted into partons whose interactions are described by the ZPC parton cascade model [111]. These partons are then combined into the final-state hadrons via a quark coalescence model. [112]

In both configurations, the dynamics of the subsequent hadronic matter is described by a hadronic cascade based on a Relativistic Transport (ART) model [113] which also includes resonance decays. The third version presented in this article is based on the string melting configuration, in which the hadronic rescattering phase is switched off to study its influence to the development of anisotropic flow. The input parameters used in both configurations are: $\alpha_s = 0.33$, a partonic cross-section of 1.5 mb, while the Lund string fragmentation parameters were set to $\alpha = 0.5$ and $b = 0.9 \text{ GeV}^{-2}$. Even though the string melting version of AMPT [114, 108] reasonably reproduces particle yields, p_T spectra, and v_2 of low- p_T pions and kaons in central and mid-central Au-Au collisions at 200 GeV and Pb-Pb collisions at 2.76 TeV [115], it was seen clearly in the recent study [116] that it fails to quantitatively reproduce the measurements. It turns out that the radial flow in AMPT is 25% lower than the measured value at the LHC, which indicates that the unrealistically low radial flow in AMPT is responsible for the quantitative disagreement. The detail configurations on AMPT settings used for this article and the comparisons of p_T differential v_n for pions, kaons and protons to the data can be found in [116].

The results of comparison to AMPT are shown in Fig.4.4. As for $SC(3, 2)$, neither of the settings can describe the data and somewhat the setting with the default AMPT model follows the trend of the data closest. The same setting can describe $NSC(3,2)$ fairly well and also the sign of $NSC(3,2)$ is well reproduced by this setting while all the hydrodynamic calculations in this article failed to describe the sign of the observable in most central collisions.

Interestingly the string melting AMPT model can't capture the data well where the

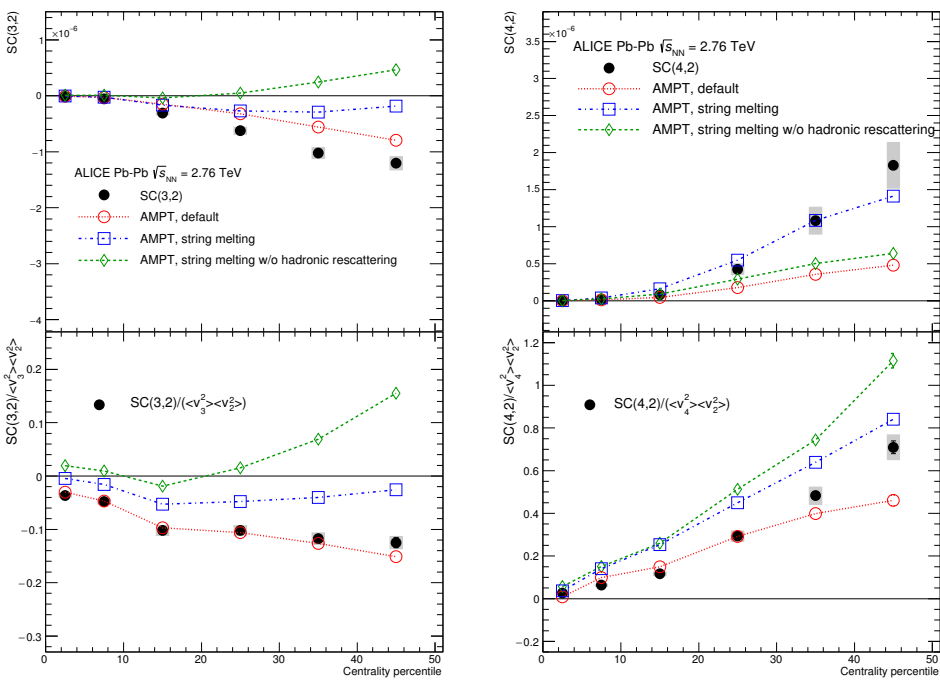


Figure 4.4: Result of $SC(3,2)$ and $SC(4,2)$ with LHC10h data and comparison to various AMPT simulations with different settings. The upper figures are the result of $SC(m,n)$ and the lower figures are the result of normalized $SC(m,n)$

Setting	String Melting	Rescattering
AMPT Default	OFF	ON
AMPT String melting	ON	ON
AMPT String melting w/o hadronic rescattering	ON	OFF

Table 4.1: Configurations of AMPT simulation dataset which correspond to ALICE LHC10h data with Pb+Pb $\sqrt{S_{NN}} = 2.76\text{TeV}$

strength of the correlation is weaker than the default model. The third version based on the string melting configuration with the hadronic rescattering phase off is also shown to study its influence. This late hadronic rescattering stage makes both $SC(3, 2)$ and $NSC(3, 2)$ stronger in the string melting AMPT model but it is not enough to describe the data.

Further we investigated why the default AMPT model can describe $NSC(3, 2)$ fairly well but underestimates $SC(3, 2)$. By taking the differences in the individual flow harmonics (v_2 and v_2) between the model and data into account, we was able to recover the data. The discrepancy in $SC(3, 2)$ can be explained by the overestimated individual v_n values reported in [116] in all the centrality ranges.

In case of $SC(4, 2)$, the string melting AMPT model can fairly describe the data while the default model underestimates it. $NSC(4, 2)$ is slightly overestimated by the same setting which can describe $SC(4, 2)$ but the default AMPT model can describe the data better. The influence of the hadronic rescattering phase for $NSC(4, 2)$ is opposite to other observables ($SC(3, 2)$, $NSC(3, 2)$ and $SC(4, 2)$), where the hadronic rescattering make $NSC(4, 2)$ slightly smaller. It should be noted that the better agreement for $SC(m, n)$ should not be overemphasized since there are discrepancies in the individual v_n between AMPT and data as it was demonstrated for $SC(3, 2)$. Hence the simultaneous description of $SC(m, n)$ and $NSC(m, n)$ should give better constrains to the parameters in AMPT.

The comparison to VISH2+1 calculation are shown in Fig.4.5. The VISH2+1 [117]

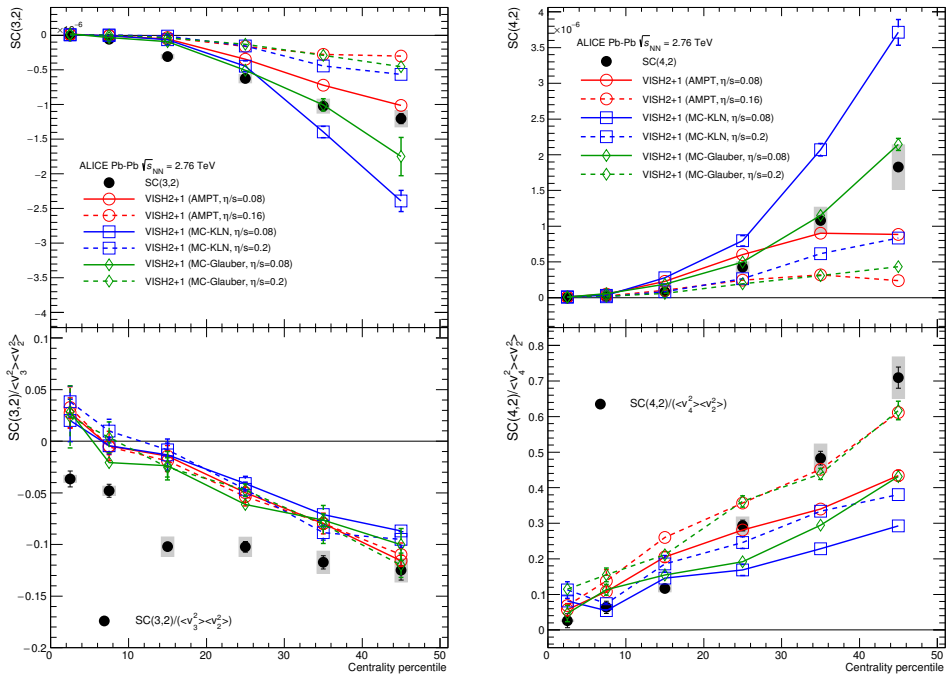


Figure 4.5: Result of $SC(3, 2)$ (left) and $SC(4, 2)$ (right) with LHC10h data and various VISH2+1 calculation with different settings. The three initial conditions from AMPT, KLN, and Glauber simulations are drawn as a different color. Furthermore, the hydrodynamic properties of η/s are shown as line style, the small share viscosity ($\eta/s=0.08$) are shown as solid line, and large share viscosity ($\eta/s=0.2$ for KLN and Glauber, 0.16 for AMPT) is drawn as dashed line. Upper figures are the result of $SC(m, n)$ and lower figures are results of normalized $SC(m, n)$

is an event-by-event theoretical framework model for relativistic heavy-ion collision based on (2+1)-dimensional viscous hydrodynamics which describes both the QGP fluid and the highly dissipative and even off-equilibrium late hadronic stage with fluid-dynamics. With well tuned transport coefficients, decoupling temperature and some well-chosen initial conditions (like AMPT [118, 119, 120] etc.), it could fit many related soft hadron data, such as the p_T spectra and different flow harmonics at RHIC and the LHC [121, 122, 24, 119]. Three different initial conditions (MC-Glauber, MC-KLN and AMPT) along with different constant η/s parametrizations are used in the model. Traditionally, the Glauber model constructs the initial entropy density of the QGP fireball from a mixture of the wounded nucleon and binary collision density profiles [123], and the KLN model assumes the initial entropy density is proportional to the initial gluon density calculated from the corresponding k_T factorization formula [124]. In the Monte-Carlo versions (MC-Glauber and MC-KLN) [5, 125, 126], additional initial state fluctuations are introduced through the position fluctuations of individual nucleons inside the colliding nuclei. For the AMPT initial conditions [119, 120, 118], the fluctuating energy density profiles are constructed from the energy decompositions of individual partons, which fluctuate in both momentum and position space. Compared with the MC-Glauber and MC-KLN initial conditions, the additional Gaussian smearing parameter in the AMPT initial conditions makes the typical initial fluctuation scales changeable which gives rise to non-vanishing initial local flow velocities [120].

As shown in the Fig.4.5, all the models with the large share viscosity regardless of the initial conditions ($\eta/s=0.2$ for MC-KLN and MC-Glauber initial conditions and $\eta/s = 0.16$ for AMPT initial condition) failed to capture the centrality dependence of $SC(3, 2)$ and $SC(4, 2)$. However, for the normalized case(NSC), all the results with different parameters do not have much difference as like original $SC(m, n)$. It may suggest that the η/s parametrization affects the single flow magnitude, (generally large share viscosity(η/s) leads short mean free path(λ_{mfp}) and it decreases the flow magnitudes) rather than affect on correlations between flow orders. And among the models with small shear viscosities ($\eta/s=0.08$), the one with the AMPT initial condition describes the data better both for $SC(3, 2)$ and $SC(4, 2)$ but they cannot describe the

1197 data quantitatively for most of the centrality ranges. As similarly as the above mentioned
1198 hydrodynamic calculations [13], the sign of the $NSC(3, 2)$ in these models is opposite
1199 to the data in 0-10% central collisions. $NSC(3, 2)$ don't show sensitivity to neither
1200 initial conditions nor η/s parametrizations and cannot be described by these models
1201 quantitatively. However, for $NSC(4, 2)$, it is sensitive both to initial conditions and η/s
1202 parametrizations. Even though $NSC(4, 2)$ is flavoured both by AMPT initial condition
1203 with $\eta/s=0.08$ and MC-Galuber initial condition with $\eta/s=0.20$, $SC(4, 2)$ can be only
1204 described by smaller η/s from AMPT and MC-Glauber initial conditions. Therefore
1205 the Galuber initial condition with $\eta/s=0.20$ model can be ruled out and we come to a
1206 conclusion based on the tested model parameters that η/s should be small and AMPT
1207 initial condition is flavoured by the data.

1208 4.2 Higher order flow harmonics results

1209 In this section, we will present the results of the correlation between higher order
1210 flow harmonics up to 5th order. The results with q-Cumulants method (SP method)
1211 with $|\eta| < 0.8$, $0.2 < p_T < 5.0\text{GeV}/c$ from ALICE data are shown. The lower order
1212 $SC(m, n)$ are scaled down and drawn together as colored band for comparison.

1213 As predicted as hydrodynamic calculation [99] the correlation between v_3^2 and v_4^2 is
1214 negative and the others are positive. The correlation between higher harmonics (v_3 and
1215 v_4 , v_2 and v_5 , v_3 and v_5) become smaller for more central collisions, and it suggests
1216 that the correlation is likely due to the non-linear contributions of higher order flow
1217 harmonics like v_4 and v_5 [127].

1218 However, unlike $SC(m, n)$, $NSC(m, n)$ results with the higher order flow harmon-
1219 ics show almost same order of the correlation strength as the lower order flow harmonic
1220 correlations ($NSC(3, 2)$ or $NSC(4, 2)$). $NSC(4, 3)$ is comparable to $NSC(3, 2)$ and
1221 one finds that a hierarchy $NSC(5, 3) > NSC(4, 2) > NSC(5, 2)$ holds for most of
1222 centrality ranges within the errors. These results indicate that the lower oder harmonic
1223 correlations ($SC(3, 2)$ and $SC(4, 2)$) are larger than higher order harmonic correlations
1224 ($SC(4, 3)$, $SC(5, 2)$, and $SC(5, 3)$), not only because of the correlation strength itself
1225 but also the individual flow strength. $SC(5, 2)$ is stronger than $SC(5, 3)$, however as for

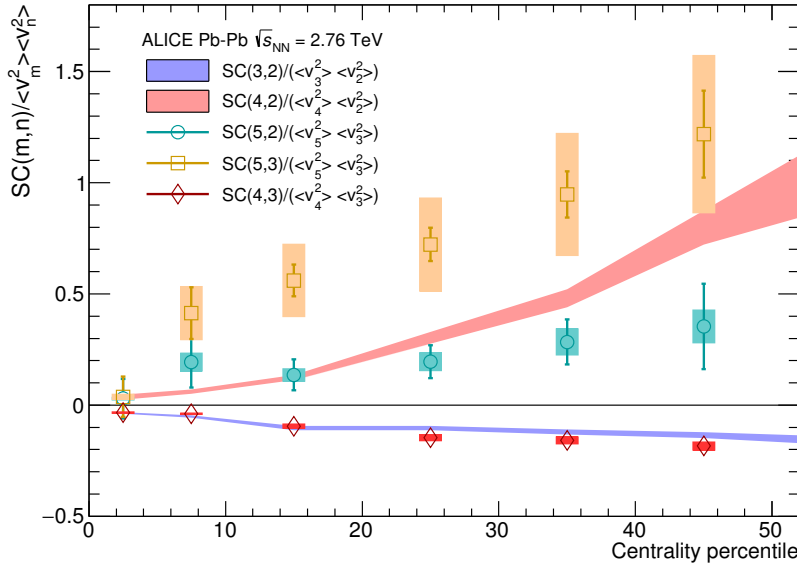
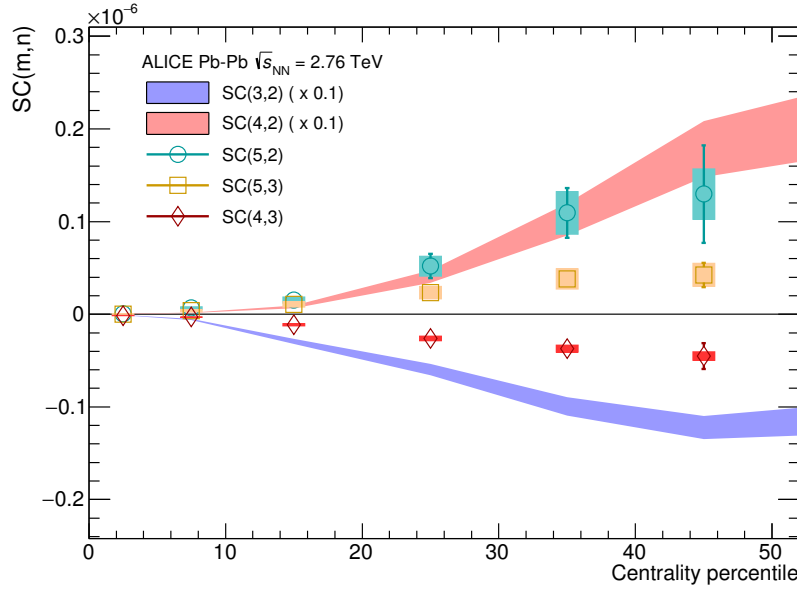


Figure 4.6: The result of $SC(m, n)$ (upper figure) and $NSC(m, n)$ (bottom figure) with higher order up to 5th flow harmonics with q-Cumulants method from ALICE Pb+Pb $\sqrt{s_{NN}} = 2.76\text{TeV}$. Note that The lower order $SC(m, n)$ are scaled down. Both $SC(m, n)$ and $NSC(m, n)$ with lower orders are drawn as colored band and statistical and systematical errors were quadratically merged.

1226 NSC , the correlation between v_5 and v_3 is stronger than the correlation between v_5 and
 1227 v_2 .

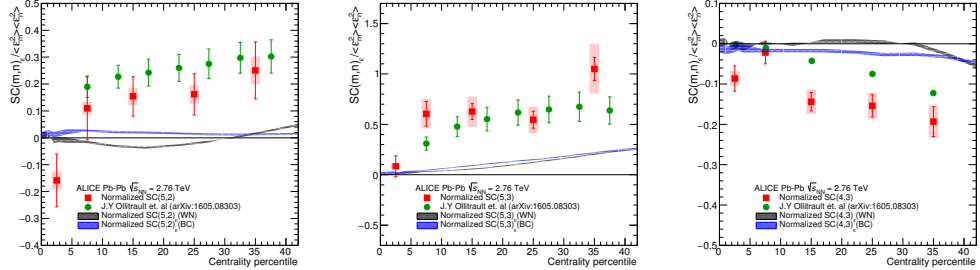


Figure 4.7: Result of higher order $NSC(m, n)$ and comparison to MC-Glauber models and prediction from J.Y Ollitraults[14]

1228 The $NSC(m, n)$ with higher order harmonics were compared to MC-Glauber to
 1229 check the response (both linear and non-linear) of initial geometry. The $NSC(m, n)$ in
 1230 coordinate space (as defined in Eq.4.1) with both WN and BC weights were compared
 1231 and shown in Fig.4.7. The large differences between MC-Glauber models (both WN and
 1232 BC) and data shows that the correlation between flow harmonics can not be explained
 1233 by only linear contribution of initial fluctuation. Also the prediction from J.Y Ollitraults
 1234 from ALICE lower order $SC(m, n)$ and EP(Event Plane) correlation from ATLAS with
 1235 few assumptions[14] were shown together as green marker in Fig.4.7. Although it pre-
 1236 dict better than any other existing theoretical models, however still have some deviation
 1237 between data for $NSC(4, 3)$ case.

1238 The extracted results from particle level AMPT simulations in the same way as for
 1239 the data are compared to the data in Fig.???. The string melting AMPT model describes
 1240 $SC(5,2)$ and $SC(5,3)$ well. The same setting describes only $NSC(5, 3)$. However, it
 1241 overestimates $NSC(5, 2)$. However the default AMPT model can describe $NSC(5, 3)$
 1242 and $NSC(5, 2)$ fairly well as similarly as $NSC(3, 2)$ and $NSC(4, 2)$. In case of
 1243 $SC(4, 3)$, neither of the settings can describe the data but the default AMPT model
 1244 follows the data closest. The string melting AMPT model fails to describe $SC(4, 3)$
 1245 and $NSC(4, 3)$. In summary, the default AMPT model describes the normalized SC

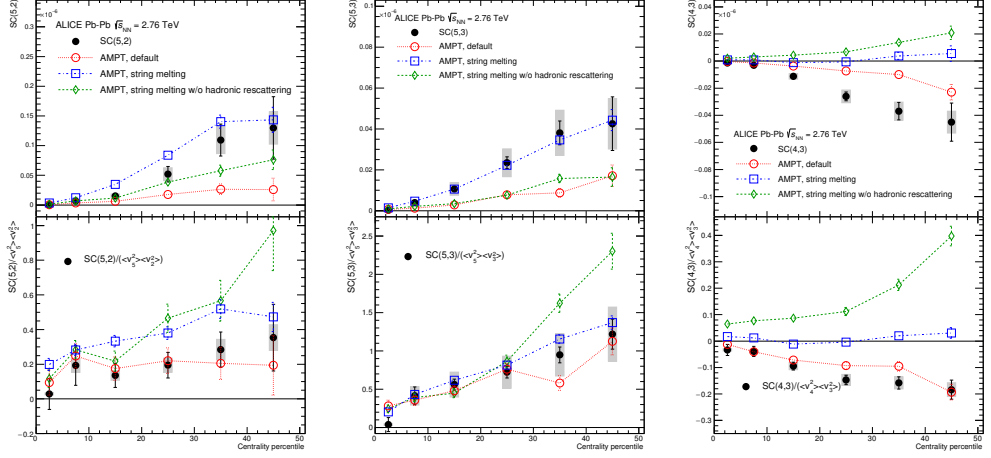


Figure 4.8: Result of $SC(5, 2)$, $SC(5, 3)$ and $SC(4, 3)$ and comparison to various AMPT simulations with different settings. Upper figures are the results of $SC(m, n)$ and the lower figures are the results of $NSC(m, n)$

1246 ($NSC(m, n)$) from lower to higher order harmonic correlation while the string melting
 1247 AMPT model overestimates $NSC(5, 2)$ and underestimates (or very weak correlations)
 1248 $NSC(4, 3)$.

1249 The event-by-event calculation from VISH by using a hybrid approach based on
 1250 (2+1)-dimensional viscous hydrodynamics(VISH2+1) were tested and shown in Fig.4.9.
 1251 All the models with the large share viscosity regardless of the initial conditions ($\eta/s=0.2$
 1252 for MC-KLN and MC-Glauber initial conditions, and $\eta/s = 0.16$ for AMPT) failed to
 1253 capture the centrality dependence of $SC(5, 2)$, $SC(5, 2)$, and $SC(5, 3)$ more clearly
 1254 than lower order harmonic correlations ($SC(3, 2)$, $SC(4, 2)$). And among the models
 1255 with small shear viscosity ($\eta/s=0.08$), the one from the AMPT initial condition de-
 1256 scribes the data much better than the other initial conditions. A quite clear separation
 1257 between different initial conditions is observed for these higher order harmonics corre-
 1258 lations compared to the lower order harmonic correlations. $NSC(5, 2)$ and $SC(5, 3)$ are
 1259 quite sensitive to both the initial conditions and the η/s parametrizations. As similarly
 1260 as the above mentioned hydrodynamic calculations [13], the sign of the $NSC(4, 3)$ in

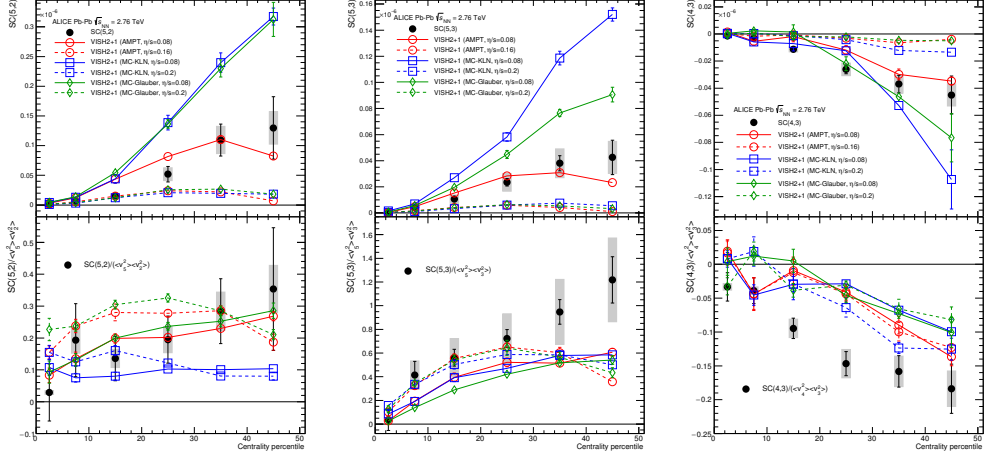


Figure 4.9: Result of $SC(5,2)$, $SC(5,3)$ and $SC(4,3)$ with ALICE data and comparison to various VISH2+1 calculation with different settings. The configurations are same as Fig.4.5

these models is opposite to the data in 0-10% central collisions. NSC(4,3) shows sensitivity to both initial conditions and η/s parameterizations while $NSC(3,2)$ didn't show sensitivity to neither initial conditions nor η/s parameterizations. $SC(4,3)$ data is clearly flavoured by smaller η/s but NSC(4,3) cannot be described by these models quantitatively.

4.3 p_T dependence of $SC(m, n)$ and normalized $SC(m, n)$

To analyze p_T dependence of $SC(m, n)$ and normalized $SC(m, n)$ result, we set various cut conditions for p_T of measuring particles, instead of using all charged hadrons with $0.2 < p_T < 5.0 \text{ GeV}/c$ in $|\eta| < 0.8$ region. The simplest approach to analyze p_T dependence is to apply different p_T bin windows when measuring $SC(m, n)$. But the number of particles in each p_T bin groups decreases rapidly as function of p_T and the number of combination for cumulants pair will decrease even more rapidly ($\sim \frac{1}{n^4}$) and this method causes large statistical fluctuations. Because the original $SC(m, n)$ has only the order of few 10^{-6} strength signal, it is not simple to get clear p_T dependence from different p_T window bins from a large statistical fluctuations. To prevent the statistical

1275 fluctuation issue, we apply minimum p_T cuts, instead of p_T bin-by-bin windows. In
1276 this analysis, we tested $SC(m, n)$ s (and also $NSC(m, n)$ s) with different p_T conditions
1277 from $0.2 \sim 5.0\text{GeV}/c$ to $1.5 \sim 5.0\text{GeV}/c$.

1278 The result of p_T dependence with $SC(3, 2)$ and $SC(4, 2)$ is shown in Fig.4.10. As
1279 seen in figure, the strength of $SC(m, n)$ correlation becoming larger as function of min-
1280 imum p_T . This indicates that the relationship between event-by-event fluctuation of two
1281 different flow harmonics v_m and v_n is stronger in high p_T region. This p_T dependence
1282 correlation is relatively small in central collision centralities and large in non-central col-
1283 lisions. However, this correlation between flow harmonics and p_T is not clearly shown
1284 in $NSC(m, n)$ s. The $NSC(m, n)$ results are aligned all together and consistent within
1285 errors. The ratio to default cut ($0.2 < p_T < 5.0\text{GeV}/c$) is nearly 1 for all centrality.
1286 This suggests that the p_T dependence of $SC(m, n)$ are not solely comes from the corre-
1287 lation between flow harmonics but comes from the strength dependence of p_T of single
1288 v_n values. Minimum p_T cuts are extended to $1.5\text{ GeV}/c$ and the results are shown in
1289 Fig.4.11. Even in higher minimum p_T cuts, there is no clear p_T dependence in nor-
1290 malized $SC(3, 2)$ or $SC(4, 2)$. For detail study of p_T dependence of $NSC(m, n)$, the
1291 $NSC(m, n)$ as function of minimum p_T cuts are prepared in Fig.4.12. Unlike AMPT
1292 prediction, the results from the data does not have clear p_T dependence up to 40% colli-
1293 sion centralities. In 40-50% collision centrality region, there is a slightly decreased slope
1294 in $NSC(3, 2)$ but it is not enough to say that there is p_T dependence for $NSC(3, 2)$. For
1295 AMPT simulations, AMPT with string melting configuration failed to capture data re-
1296 sult. These AMPT simulation predict that normalized $SC(m, n)$ increase as a function
1297 of minimum p_T and turns over to positive values around minimum $p_T \sim 1.0\text{GeV}/c$. But
1298 in LHC10h data, the results remains in negative values for all minimum p_T bins, and
1299 centrality bins. Also for $NSC(4, 2)$ cases, only AMPT default which has the configura-
1300 tion without string melting, has similar values with data. The others (AMTP with string
1301 melting) predict increase of $NSC(4, 2)$ from around $\sim 1\text{GeV}/c$ minimum p_T cuts, and
1302 failed to reproduce the data.

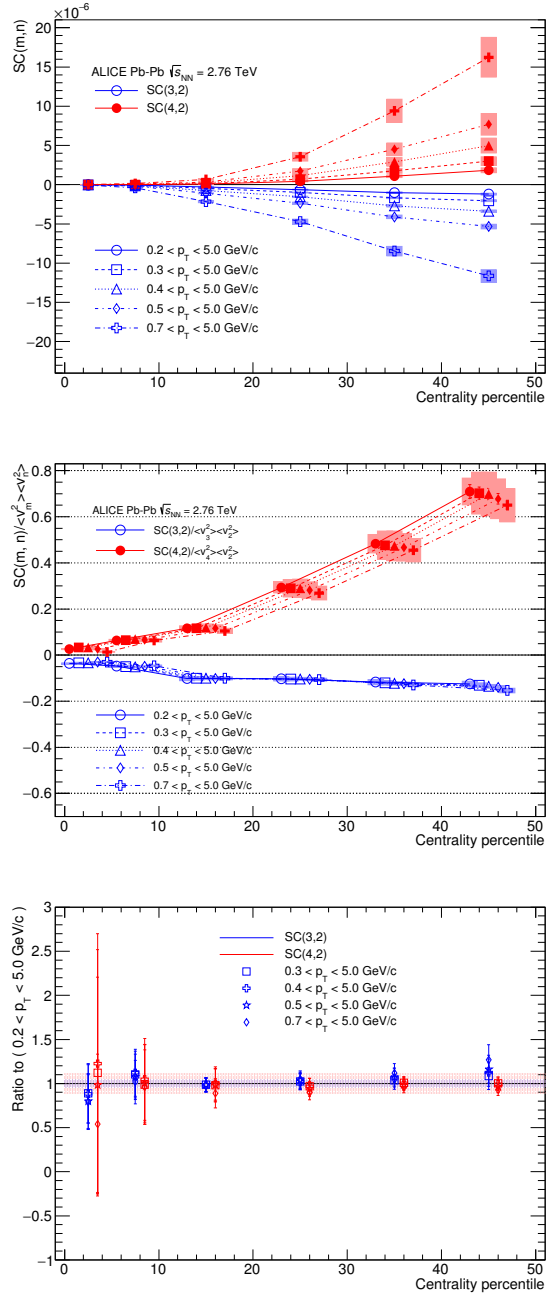


Figure 4.10: The results of $SC(3,2)$ and $SC(4,2)$ with various minimum p_T cut conditions (Top) and results of $NSC(3,2)$ and $NSC(4,2)$ (Middle). The ratio of $NSC(m, n)$ results with various minimum p_T cut conditions to default ($0.2 < p_T < 5.0 \text{ GeV}/c$) are shown in bottom figure.

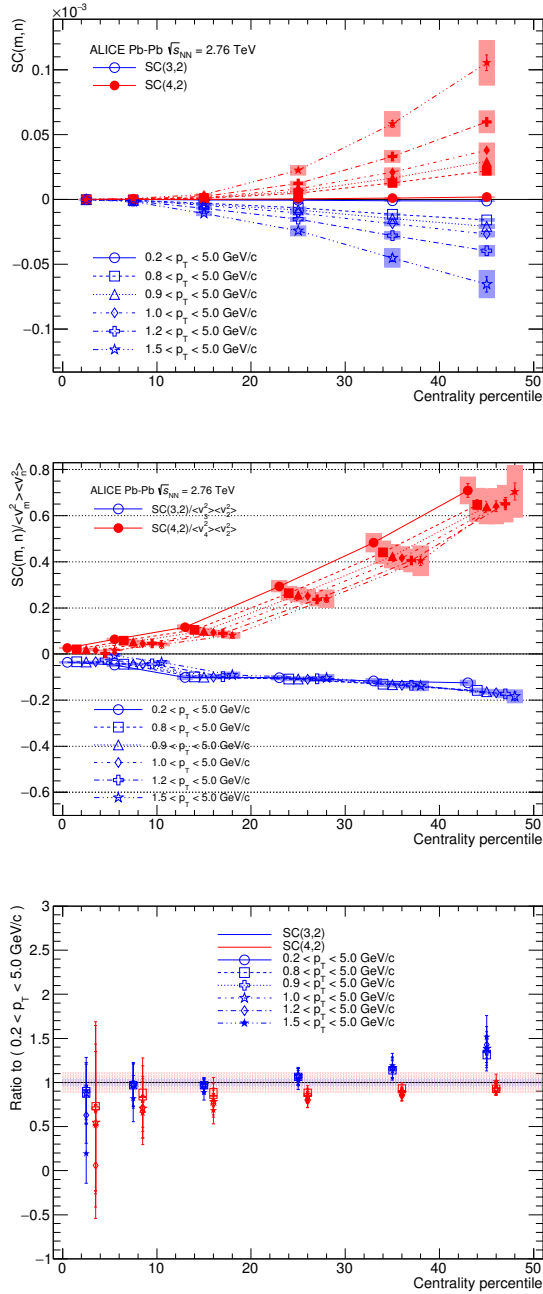


Figure 4.11: The results of $SC(3,2)$ and $SC(4,2)$ with various minimum p_T cut conditions (Top) and results of $NSC(3,2)$ and $NSC(4,2)$ (Middle). The ratio of $NSC(m, n)$ results with various minimum p_T cut conditions to default ($0.2 < p_T < 5.0 \text{ GeV}/c$) are shown in bottom figure.

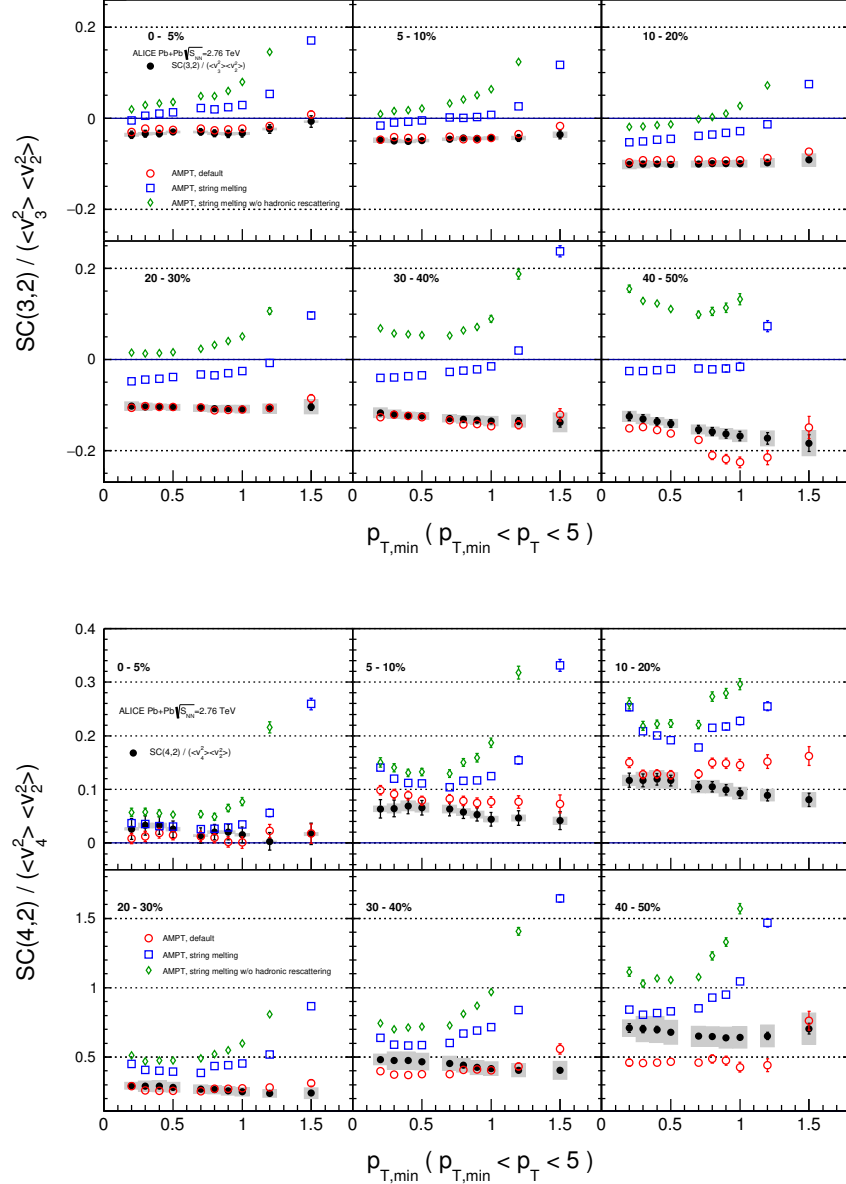


Figure 4.12: $NSC(3,2)$ (Top) and $NSC(4,2)$ (Bottom) as a function of minimum p_T cuts with ALICE Pb+Pb $\sqrt{S_{NN}} = 2.76$ TeV. The AMPT simulation results are drawn together as colored band for comparison. The corresponding AMPT configurations are shown in legend.

1303 **4.4 Method comparison**

1304 The Eq.3.2 is based on the multi-particle q-Cumulants method(i.e. QC method),
1305 but it can be also obtained by calculating moments [99] as discussed in the previous
1306 section3.2.

1307 As seen in Fig.4.13 in both methods, the flow harmonics with 2nd and 4th are corre-
1308 lated. On the other hand, 2nd and 3rd harmonics are anti-correlated. The strength of cor-
1309 relation is small in the central collision region and becomes stronger in non-central colli-
1310 sion in both q-Cumulant method(QC) and Scalar Product method(SP). Also $NSC(m, n)$
1311 which is divided by products $\langle v_m^2 \rangle \langle v_n^2 \rangle$, in order to obtain the normalized observables are
1312 shown and suggests the same trend but a large deviation especially for $SC(4, 2)$. HIJING
1313 simulations results from SP methods are shown together for comparison.

1314 The advantage of using the SP method is that calculations are much simpler and
1315 faster in estimating the correlation between flow harmonics. Instead of calculating par-
1316 ticle pair of 4- or 2- cumulants, the SP method needs only one calculation between mea-
1317 sured n^{th} order flow Q -vector. The other advantage of the SP method is that it can be
1318 applied for not only $SC(m, n)$ which observables for flow “magnitudes” correlation, but
1319 also for the flow ”direction” correlations like event-plane correlation. [9] or non-linear
1320 response of flow harmonics [128].

1321 However, the disadvantage of SP methods is (likely) under estimation of $SC(m, n)$
1322 in low multiplicity regions. This effects were discussed with ToyMC simulation in Ap-
1323 pendix A. Because of this issue of difference between two different methods and inaccu-
1324 racy(under estimation) of SP method in low multiplicity regions, we used all the result
1325 from QC method as the default in this analysis.

1326 **Method comparison of higher order harmonics**

1327 Also $SC(m, n)$ and $NSC(m, n)$ results with higher order flow harmonics (up to
1328 5th order) were measured by the SP method, and the results are shown in Fig.4.14. For
1329 the higher order, because of statistical fluctuation for peripheral collisions, results were
1330 only taken from the 0% to 40% collision centrality regions. As a result, the two methods
1331 shows the consistent values within errors.

1332 **p_T dependence of $SC(m, n)$ with SP method**

1333 The p_T dependence of $SC(m, n)$ and $NSC(m, n)$ were checked with the SP method.
1334 The results of $SC(m, n)$ and $NSC(m, n)$ with different minimum p_T cuts are shown
1335 in Fig.4.15(up to 0.7 GeV/c minimum p_T cuts) and Fig.4.16(up to 1.5 GeV/c) min-
1336 imum p_T cuts. As seen in Fig.4.15, there is certain p_T dependence for $SC(m, n)$, but
1337 not clear p_T dependence for $NSC(m, n)$ as like QC method. However, in even higher
1338 p_T region(Fig.4.16), unlike the results with QC methods, we could see weak p_T depen-
1339 dence in $NSC(m, n)$. In the $SC(m, n)$ results, as the minimum p_T cuts goes higher, the
1340 strength of the correlation becomes stronger in both $SC(3, 2)$ and $SC(4, 2)$. However,
1341 in $NSC(m, n)$ with the SP method, when the minimum p_T cuts increase, the strength
1342 of correlation for $NSC(3, 2)$ is (negatively) stronger, but the strength of correlation of
1343 $NSC(4, 2)$ becomes weaker. As a result, in higher p_T range, the $NSC(m, n)$ values
1344 always getting smaller.

1345 For the better comparison, the ratio of normalized $SC(m, n)$ with various minimum
1346 p_T cuts to default is shown in Fig.4.17. Up to 0.7 GeV/c, the ratio of $NSC(m, n)$ values
1347 are consistent with a default cut within errors, but the minimum p_T exceeds 0.8GeV/c,
1348 the ratio of $NSC(3, 2)$ moving above the 1, and the ratio of $NSC(4, 2)$ goes down
1349 below the 1. The reason why these trends are only shown in the SP method, and not in
1350 the QC is not yet fully explained. However, the disadvantage of the SP method is that
1351 we lose almost half of the statistics because of a large η gap around $\eta = 0$ and also the
1352 number of combinations for the track pair is $\frac{1}{3}$ when compared to QC methods. This is
1353 one possible option to explain these p_T dependence behavior of SP method, and tested
1354 in ToyMC simulation in Appendix A.

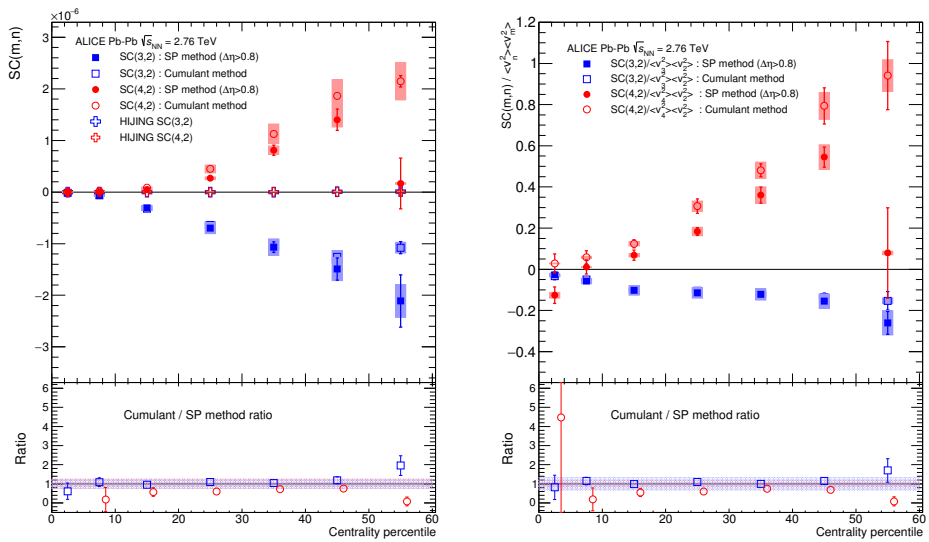


Figure 4.13: Comparison of $SC(m, n)$ (Top) and normalized $SC(m, n)$ (Bottom) results for $SC(3, 2)$ (blue) and $SC(4, 2)$ (red) with the SP and QC method up to 60% centralities. The different ratios are shown in lower pads, and systematic uncertainty is drawn as a band around 1

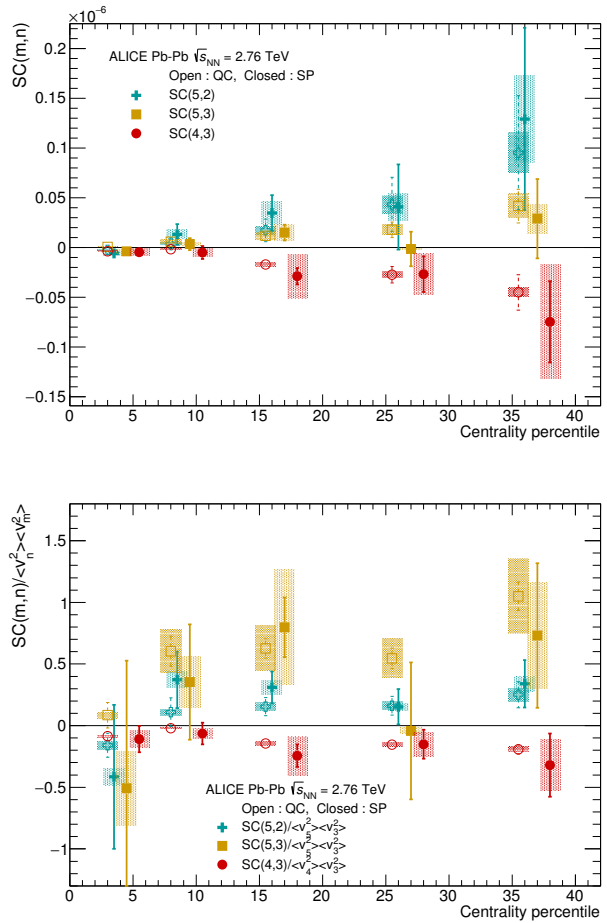


Figure 4.14: Result of higher order $SC(m, n)$ and $NSC(m, n)$ with two different method QC and SP. Along x-axis offset was applied for better visibility. For the QC method $|\eta| < 0.8$ cut was applied, while SP method takes $0.4 < |\eta| < 0.8$.

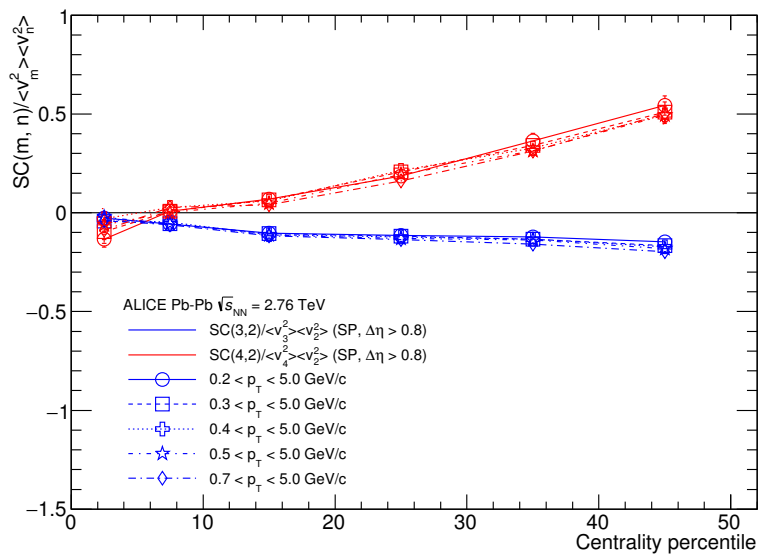
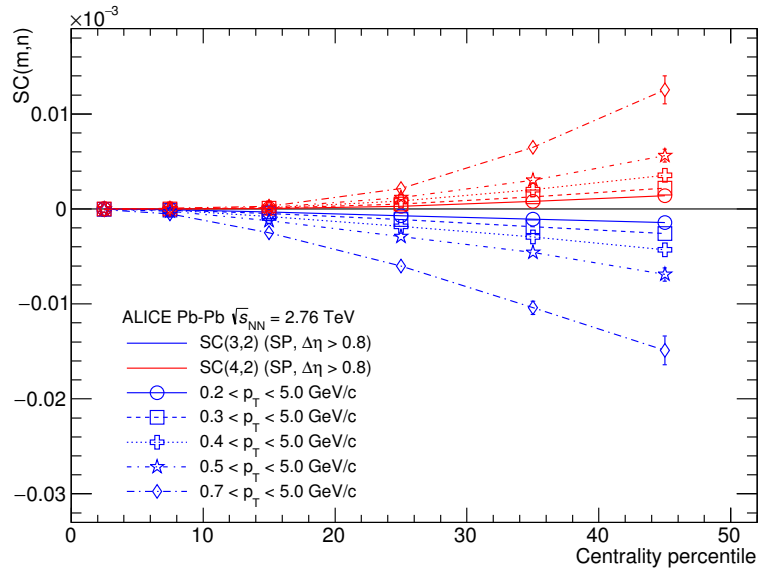


Figure 4.15: $SC(m, n)$ and $NSC(m, n)$ with SP method with default cuts ($0.2 < p_T < 5.0$ GeV/c) and various minimum p_T cuts up to 0.7 GeV/c

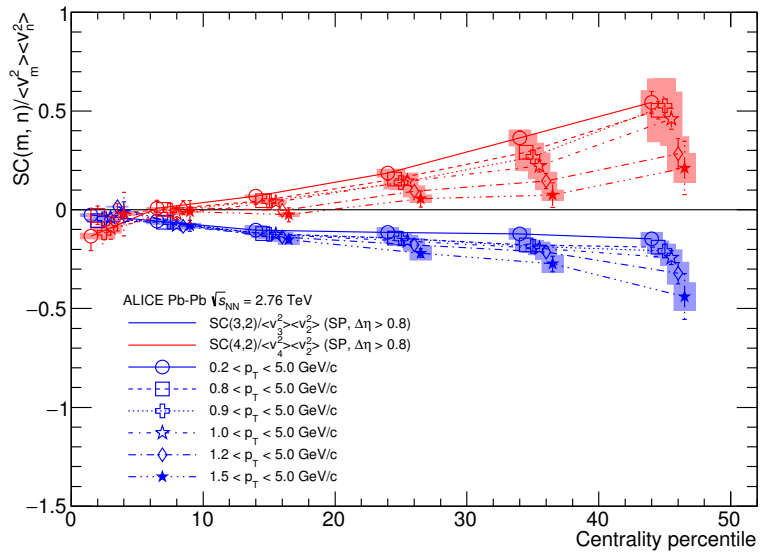
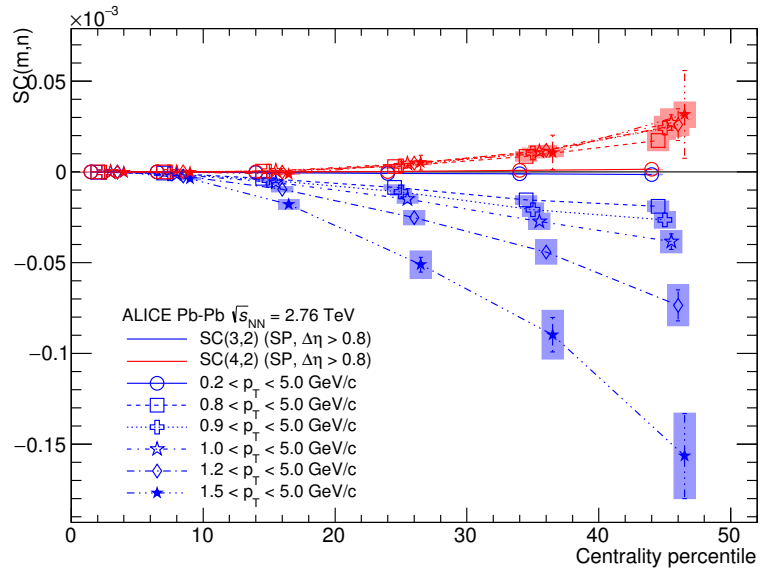


Figure 4.16: $SC(m, n)$ and $NSC(m, n)$ with SP method with default cuts ($0.2 < p_T < 5.0$ GeV/c) and various minimum p_T cuts up to 1.5 GeV/c)

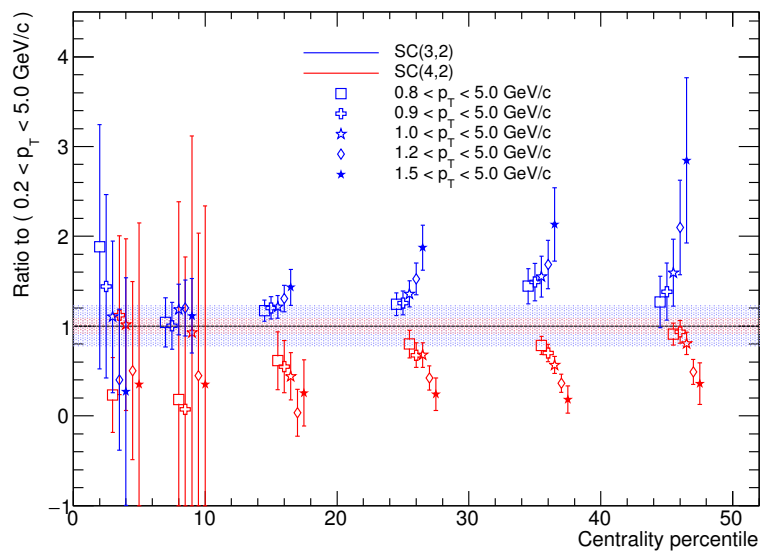
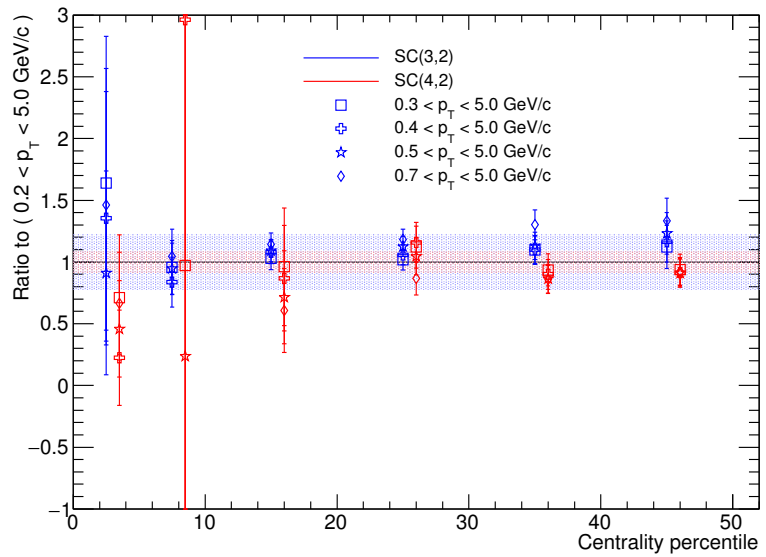


Figure 4.17: The ratio of $NSC(m, n)$ with SP method to the default cuts

₁₃₅₅ **Chapter 5**

₁₃₅₆ **Conclusion and Outlook**

₁₃₅₇ As the strong evidence of QGP, flow has been studied in detail during the past few
₁₃₅₈ decades. But only a few studies have been done about correlation between flow harmon-
₁₃₅₉ ics and leads to the following questions; How do v_n and ϵ_n fluctuate and what is the
₁₃₆₀ underlying probability density function (*p.d.f*) of their distribution? How are the initial
₁₃₆₁ geometry fluctuations reflected in differential flow measurements? What is the relation-
₁₃₆₂ ship between different harmonic event plane angle? What is the relationship between the
₁₃₆₃ flow coefficient of different harmonics? The answers to above questions (especially for
₁₃₆₄ the last) *SymmetricCumulants* ($SC(m, n)$) have been introduced as the first and only
₁₃₆₅ observable to measure correlation between flow harmonic “magnitudes” v_m and v_n .

₁₃₆₆ As the result of $SC(m, n)$, we found that the correlation between v_2 and v_4 is posi-
₁₃₆₇ tive(correlated), and the correlation between v_2 and v_3 is negative(anti-correlated). The
₁₃₆₈ various hydrodynamic calculations and model simulations were studied together as a
₁₃₆₉ reference. The large differences between data and MC-Glauber studies confirmed that
₁₃₇₀ the correlation were not able to explained by only linear response of initial conditions,
₁₃₇₁ and there is certain non-linear contribution of initial fluctuations.

₁₃₇₂ None of the existing models and hydrodynamic calculation with the different parametriza-
₁₃₇₃ tions of the temperature dependence of η/s couldn't exactly capture the data quantita-
₁₃₇₄ tively. Furthermore, the sign of v_3-v_2 correlation in most central collision range(0-10%)
₁₃₇₅ was found to be different between the data and hydrodynamic model calculations. In the
₁₃₇₆ most central collisions the anisotropies originate mainly from fluctuations, i.e. the ini-

1377 tial ellipsoidal geometry characteristic for mid-central collisions plays little role in this
1378 regime. It is suggested that the $SC(m, n)$ is more sensitive to both initial conditions and
1379 hydrodynamic property η/s than single flows.

1380 The analysis with higher order flow harmonics provides that the correlation between
1381 higher order flow harmonics and lower order harmonics is likely due to the non-linear
1382 contributions. It also indicates that the higher order flow can be understood as the su-
1383 perposition of the lower order flow harmonics. This analysis will help constrain the
1384 theoretical description of the fluid close the freeze-out temperature which is probably
1385 the least understood part of hydrodynamic calculation. [59] [128]

1386 We introduce the Scalar Product method (SP method) to measure $SC(m, n)$ and
1387 $NSC(m, n)$, and checked with the results from QC method. Basically, most of the re-
1388 sults are consistent in errors. However at some points, there are some deviations between
1389 the SP and QC methods. These differences are most pronounced in peripheral collision
1390 centrality regions. We investigate the reason of difference between two methods by test-
1391 ing and measuring $SC(m, n)$ with ToyMC, and PYTHIA jet implementation, but not
1392 able to fully explain the differences.

1393 In the study about p_T dependence, we found clear p_T dependence in original $SC(m, n)$.
1394 But although there were many theoretical predictions (with Hydrodynamic and AMPT
1395 simulation), we were unable to find p_T dependence in $NSC(m, n)$ (with QC method).
1396 The recent study about p_T dependence of flow and its direction point out that there are
1397 certain correlation between flow origin and the its p_T . Even though we see both p_T de-
1398 pendence of $SC(m, n)$ and $NSC(m, n)$ with scalar product method we are not able to
1399 say that p_T dependence are come the correlation itself or the other effects at this moment.

1400 At this point, we are not sure whether different methods respond differently to flow
1401 fluctuations or if we can rule out non-flow effects in the end. The answer might provide
1402 a hint for different sensitivities to flow fluctuations and non-flow effect. This might be a
1403 nice piece of material by itself in further study.

1404 Even though, there are some missing parts on this analysis, such as no clear p_T
1405 dependence of $NSC(m, n)$ and absence of explanation for different method response,
1406 it provides quantitative hints for the comprehensive understanding of hydrodynamical

1407 behavior of collide system evolution. Also new observables $SC(m, n)$ promise to pro-
1408 vide additional constraints on the initial state phenomena and dynamical evolution and
1409 its fluctuation without event-by-event shape engineering. Since Run2 data from LHC
1410 is approaching with a new highest record of center-of-mass energy and much higher
1411 amount of events, more interesting analysis including correlations and fluctuations will
1412 be studied again.

Appendices

1413

¹⁴¹⁴ **Appendix A**

¹⁴¹⁵ **Toy MC simulation**

¹⁴¹⁶ **A.0.1 Toy Monte Carlo simulation**

¹⁴¹⁷ In this appendix, we will use the Monte Carlo simulation to check the correlation be-
¹⁴¹⁸ tween two different flow harmonics and check the systematic response to Q -Cumulant
¹⁴¹⁹ method(QC) and Scalar Product method(SP).

Since, $SC(m, n)$ is defined as like

$$\langle v_n^2 v_m^2 \rangle - \langle v_n^2 \rangle \langle v_m^2 \rangle$$

¹⁴²⁰ it is not easy to calculate directly $SC(m, n)$ from arbitrary v_n and v_m which fluctuate
¹⁴²¹ event by event. So, in this Toy Monte Carlo simulation, we consider simplest case. i.e
¹⁴²² the uniform flow distribution. The uniform flow distribution is defined as like

$$f(v_n) = const, \quad v_{min} < v_n < v_{max} \quad (\text{A.1})$$

¹⁴²³ In this configuration, we can easily assume that the function of flow v_n can be nor-
¹⁴²⁴ malized with

$$1 = \int_{-\infty}^{\infty} f(v_n) dv \quad (\text{A.2})$$

$$= \int_{v_{min}}^{v_{max}} const dv \quad (\text{A.3})$$

$$= cont(v_{max} - v_{min}) \quad (\text{A.4})$$

1425 SO,

$$const = \frac{1}{v_{max} - v_{min}} \quad (A.5)$$

1426

1427 Then the final normalized uniform flow distribution is

$$f(v_n) = \frac{1}{v_{max} - v_{min}} \quad (A.6)$$

1428

1429 And if we assume the mean value of given order flow harmonics as μ_v , then it follows

$$1 = \int_{-\infty}^{\infty} vf(v)dv \quad (A.7)$$

$$= \int_{v_{min}}^{v_{max}} v \frac{1}{v_{max} - v_{min}} dv \quad (A.8)$$

$$= \frac{1}{v_{max} - v_{min}} \frac{v_{max}^2 - v_{min}^2}{2} \quad (A.9)$$

1430 and finally we have

$$\mu_v = \frac{v_{max} - v_{min}}{2} \quad (A.10)$$

1431

1432 To calculate standard deviation(σ_v) for event fluctuations, use the definition of
1433 expectation value of a random variables.

$$\mu_x = E[x] = \int_{-\infty}^{\infty} xf(x)dx \quad (A.11)$$

1434

$$\sigma_x^2 = V[x] = E[(x - E[x])^2] = \int_{-\infty}^{\infty} (x - \mu_x)^2 f(x)dx \quad (A.12)$$

1435

1436 So, we can get straightforwardly

$$\sigma_v^2 = \frac{1}{12} (v_{max} - v_{min})^2 \quad (A.13)$$

1437 or,

$$\sigma_v = \frac{1}{2\sqrt{3}}(v_{max} - v_{min}) \quad (\text{A.14})$$

1438

1439 So, for the uniform distribution Toy models, we can express the flow v_n and its
1440 fluctuation with events(σ_v) as term as uniform flow distribution (v_{max} and v_{min})

$$\langle v \rangle = \frac{v_{max} + v_{min}}{2} \quad (\text{A.15})$$

1441

$$\langle v^2 \rangle = \frac{v_{max}^2 + v_{max}v_{min} + v_{min}^2}{3} \quad (\text{A.16})$$

1442

$$\langle v^3 \rangle = \frac{1}{4}(v_{max} + v_{min})(v_{max}^2 + v_{min}^2) \quad (\text{A.17})$$

1443

$$\langle v^4 \rangle = \frac{1}{5}(v_{max}^4 + v_{max}^3 v_{min} + v_{max}^2 v_{min}^2 + v_{max} v_{min}^3 + v_{min}^4) \quad (\text{A.18})$$

1444

1445 With above equations, we now can express the $SC(m, n)$ as term of v_{max} and v_{min}
1446 only. For example, if we set v_2 and v_3 to have uniform distribution such as

1447 • $v_2 = \text{Uniform}[0.05, 0.08]$

1448 • $v_3 = 0.1 - v_2$

1449 then the $SC(3, 2)$ will be express as like

$$SC(3, 2) = \langle v_3^2 v_2^2 \rangle - \langle v_3^2 \rangle \langle v_2^2 \rangle \quad (\text{A.19})$$

$$= \langle x^2 (0.1 - x)^2 \rangle - \langle x^2 \rangle \langle (0.1 - x)^2 \rangle \quad (\text{A.20})$$

$$= \langle x^2 (0.01 - 0.2x + x^2) \rangle - \langle x^2 \rangle \langle (0.01 - 0.2x + x^2) \rangle \quad (\text{A.21})$$

$$= \langle 0.01x^2 \rangle - \langle 0.2x^3 \rangle + \langle x^4 \rangle - \langle x^2 \rangle (0.01 - \langle 0.2x \rangle + \langle x^2 \rangle) \quad (\text{A.22})$$

$$= -(0.2) \langle x^3 \rangle + \langle x^4 \rangle + 0.2 \langle x \rangle \langle x^2 \rangle - \langle x^2 \rangle^2 \quad (\text{A.23})$$

$$\begin{aligned} &= -(0.2) \frac{1}{4} (v_{max} + v_{min})(v_{max}^2 + v_{min}^2) \\ &\quad + \frac{1}{5} (v_{max}^4 + v_{max}^3 v_{min} + v_{max}^2 v_{min}^2 + v_{max} v_{min}^3 + v_{min}^4) \\ &\quad 0.2 \frac{v_{max}^2 + v_{max} v_{min} + v_{min}^2}{3} \frac{v_{max} + v_{min}}{2} \\ &\quad - \frac{v_{max}^2 + v_{max} v_{min} + v_{min}^2}{3} \frac{v_{max}^2 + v_{max} v_{min} + v_{min}^2}{3} \quad (\text{A.24}) \end{aligned}$$

1450 As a results $SC(3, 2) \simeq -6.78 \times 10^{-7}$, Also $SC(4, 2)$ can be obtained by similar
1451 calculations.

1452 In this analysis, we tested with ToyMC simulation for $SC(m, n)$ with both uniform
1453 fluctuation case (which is simplest case), and 2-Dim Gaussian fluctuation case (which is
1454 more realistic case) For the uniform fluctuation case, we set v_n as like

1455 • $v_2 = \text{Uniform}[0.04, 0.09]$

1456 • $v_3 = 0.1 - v_2$

1457 • $v_4 = v_2 - 0.02$

1458 These settings are based on the real flow measurements to have $\langle v_2 \rangle \sim 0.065$ which
1459 is similar v_2 in mid-central collisions, and setting v_3 to have negative correlation with
1460 similar as what it is measured. Also v_4 have been setted to have positive correlation but
1461 a little bit higher than what is measured.

1462 We performed ToyMC simulations with various multiplicity and run over 1M events
1463 per each multiplicity bins. The results are shown in Fig.A.2 and A.3. As seen in results,
1464 both Q-cumulants (QC) and Scalar Product (SP) method were able to capture input value

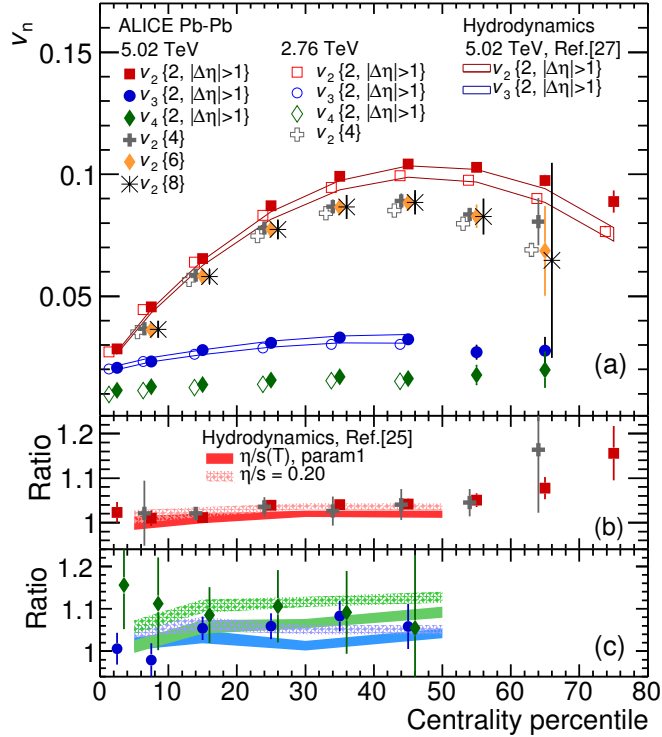


Figure A.1: Flow measurement with ALICE at $\sqrt{S_{NN}} = 2.76 \text{TeV}/c$ and $5.02 \text{TeV}/c$ with various measurement methods, also hydrodynamic predictions are drawn as bands

in high multiplicity regions with $\sim 1\%$ errors, but in low multiplicity region, we observe discrepancy between two methods and these effects are most pronounced in lowest multiplicity (corresponding to values for peripheral collisions over 60% centrality). Neither QC nor SP methods were fully free from these effects. However, because of η gap, SP method has disadvantages for the number of combinations(or multiplicity). As the result, QC methods recover better the input value than SP method, and SP method results are always smaller than QC for all multiplicity bins.

Also we tested with 2-dim Gaussian like flow fluctuations to try a realistic flow fluctuation taken from a measured distribution.

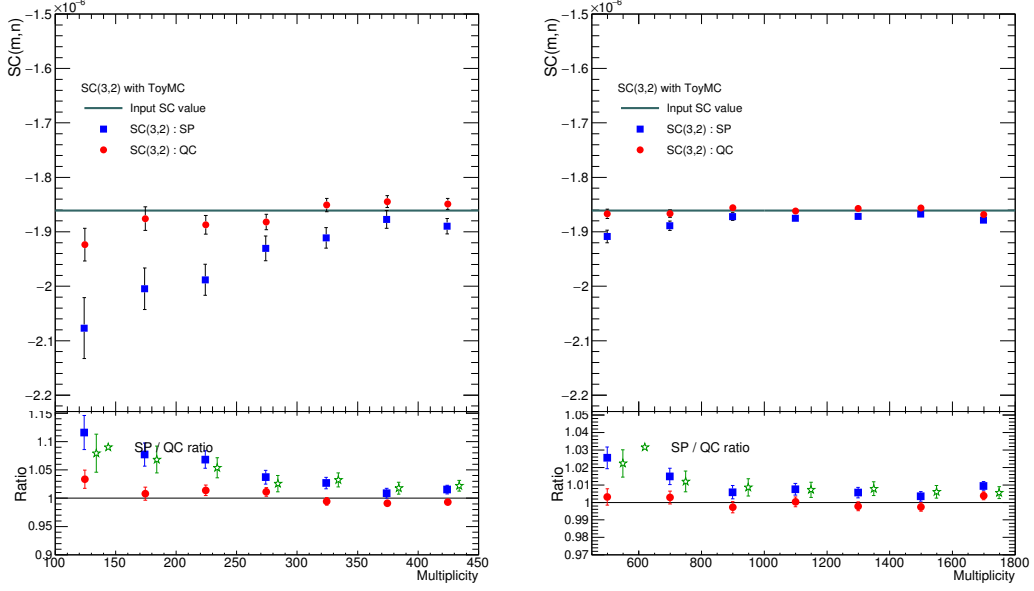


Figure A.2: Results of ToyMC simulation for SC(3,2) with random uniform distribution of v_n with various multiplicity. The left figure is the result from 50 to 450 multiplicity, and right figure is the result from 500 to 1800 multiplicity. Both Q-cumulatns(QC) and Scalar Product(SP) mehtods are tested and drawn with red and blue color marker. Also ratio to input values are drawn in bottom pad, and the ratio of SP / QC methods are drawn with green marker

$$p(v_n) = \frac{v_n}{\sigma^2} e^{-\frac{v_n^2}{2\sigma^2}}, \quad (\text{A.25})$$

1474 This is the radial projection of a 2 dimensional Gaussian distribution in \bar{v}_n . The σ
 1475 parameter is given by $\sigma = \sqrt{2/\pi} \langle v_n \rangle$
 1476 then the settings are as like followings

1477 • v_2 = Bessel Gaussian (mean 0.065)

1478 • $v_3 = 0.04 - (v_2/8)$

1479 • $v_4 = v_2/6$

1480 We set v_n to have similar values in real flow values and to have $\sim SC(m, n)$ in
 1481 mid centralities in ALICE data. The results are shown in Fig.A.5. As same as uniform

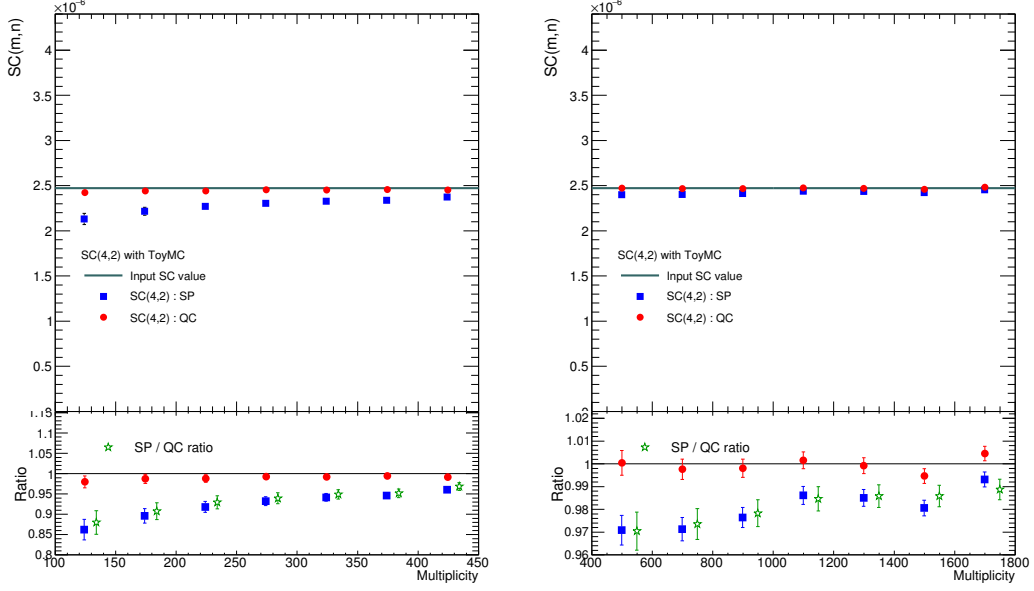


Figure A.3: Results of ToyMC simulation for $SC(4,2)$ with random uniform distribution of v_n with various multiplicity. The left figure is the result from 50 to 450 multiplicity, and right figure is the result from 500 to 1800 multiplicity. Both Q-cumulatns(QC) and Scalar Product(SP) mehtods are tested and drawn with red and blue color marker. Also ratio to input values are drawn in bottom pad, and the ratio of SP / QC methods are drawn with green marker

1482 flow distribution case both method recover input values well and consistent in 1% levels.
 1483 However when we see the details, we can check that the results from SP methods are
 1484 always lower than QC methods as like previous results. As the results, the ratio of SP
 1485 over QC results are above 1 in $SC(3, 2)$ case because it' is negative correlation. And
 1486 ratio of SP over QC are below than 1 in $SC(4, 2)$ case.

1487 A.0.2 Test non-flow effects by impose jets from PYTHIA into ToyMC

1488 $SC(m, n)$ results with HIJING are zero for all centralities for both methods, and
 1489 also even with the high p_T bins. These suggested that $SC(m, n)$ is not the results from
 1490 non-flow effects, and it is not sensitive to non-flows. In additional to HIJING results,
 1491 we now have studied it explicitly with PYTHIA jet particles on $SC(m, n)$. This implies

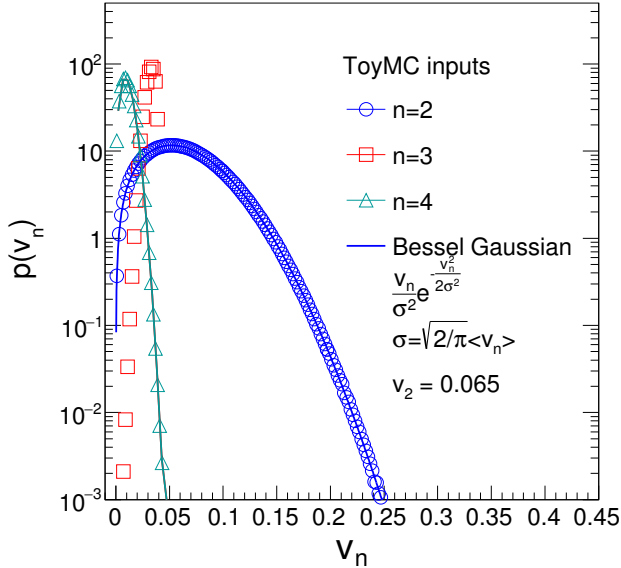


Figure A.4: Event by Event Flow harmonics distributions from Bessel Gaussian function based on [?]

1492 the largest effect from the particles which stem from jets in PYTHIA in mid central col-
 1493 lisions. To check these study, we setup ToyMC as previous section. And use PYTHIA8
 1494 to impose jet into ToyMC. To see the maximized effects on $SC(m, n)$ we use PYTHIA
 1495 setting as like followings

- 1496 • $\sqrt{S_{NN}} = 2.76 \text{ TeV}$
- 1497 • Phase Space $p_T > 5 \text{ GeV}/c$
- 1498 • Other settings use default of PYTHIA8

1499 and implement jet particles for every events. The p_T spectra and it's ratio to number of
 1500 particles in corresponding centralities are drawn in Figure. A.6. Straitforwadly the jet
 1501 effects are most pronounced in peripheral collisions and p_T regions more than $1 \text{ GeV}/c$
 1502 The results of $SC(m, n)$ with ToyMC with jets from PYTHIA is shown in Fig.A.7.
 1503 When we do not implement the PYTHIA Jet, as we expected, the results of $SC(m,n)$

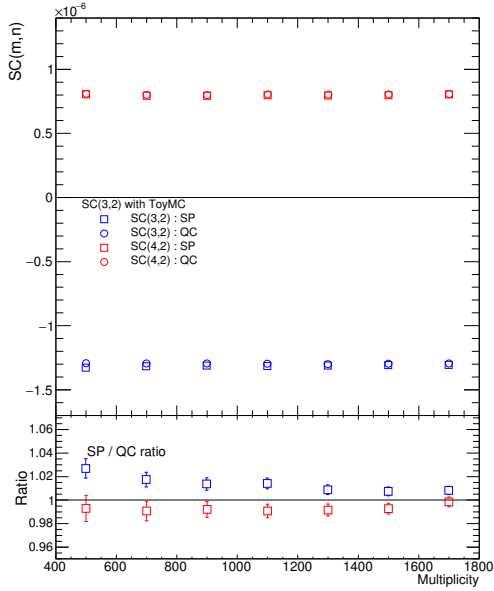


Figure A.5: Results of ToyMC simulation for $SC(m,n)$ with Bessel Gaussian like distribution, Both SP and QC results were performed and the ratio of two different methods are show in bottom pad

well capture the input values with around few % of differences. Also as we saw in
 previous section, $SC(m, n)$ with QC results have better accuracy than SP method. When
 we embed PYTHIA jet into ToyMC the both SP and QC results are suffer from the jet
 and, the strength of correlation from both methods are getting smaller. The response to
 particles from jet are quite similar for both QC and SP methods. There are few % of
 difference in central collisions and around 10% effect in 50% \sim 60% centrality bin and
 these observations hold both for $SC(3, 2)$ and $SC(4, 2)$. When we consider that these
 PYTHIA settings are almost maximized non-flow effects, and the behavior of both SP
 and QC response are same, we can conclude that the $SC(m,n)$ is insensitive to Non-flow
 effects.

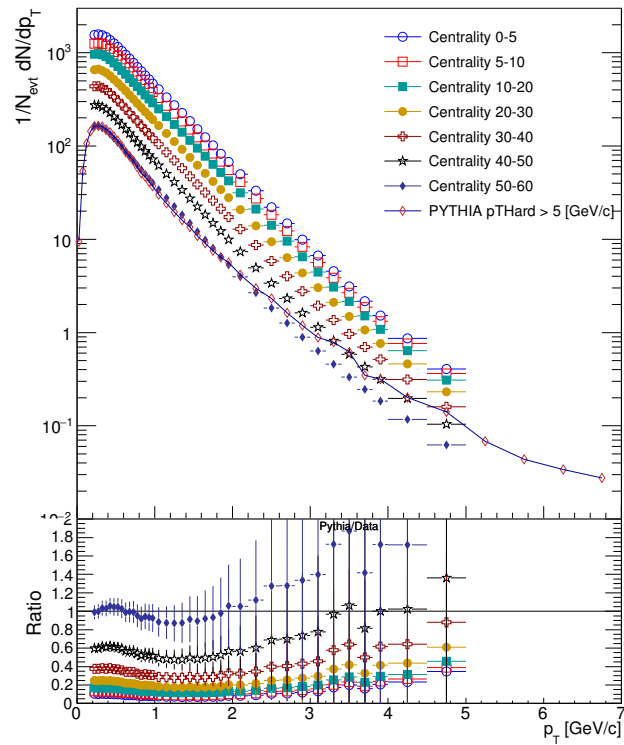


Figure A.6:

1514

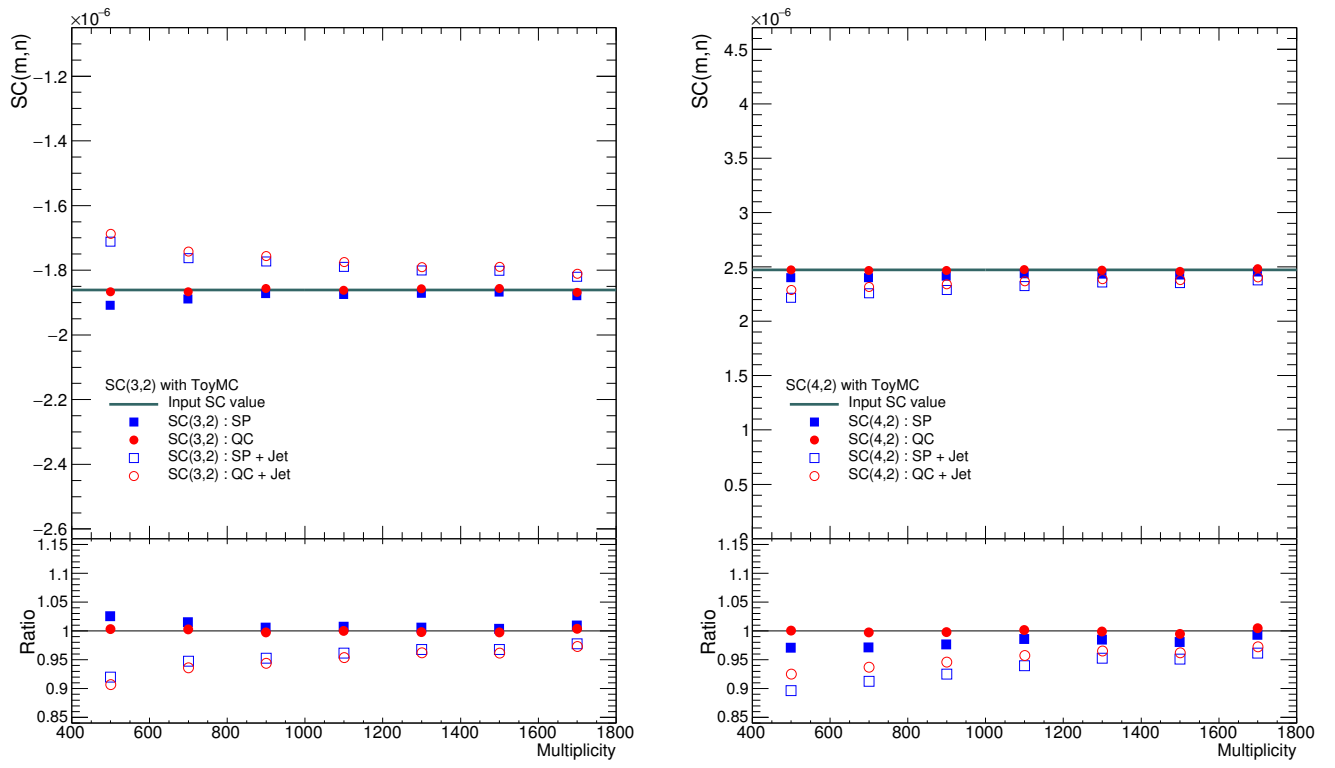


Figure A.7: The ToyMC results of $SC(3,2)$ (left) and $SC(4,2)$ (right) from 400 to 1800 multiplicity. The input values are drawn as green line. Closed markers are the results with SP and QC results without jet implementation(as same as previous results) and open markers are the results after PYTHIA jet embedding. The ratio to the input values are drawn in bottom pad

₁₅₁₅ **Appendix B**

₁₅₁₆ **Choosing weight for event average**

₁₅₁₇ The double angular brackets in flow analysis means usually means that one for aver-
₁₅₁₈ age over all particles, and the other for the average over all events.

$$\langle\langle \dots \rangle\rangle = \langle\langle \dots \rangle_{\text{particles}} \rangle_{\text{events}}$$

₁₅₁₉ And for the average over events, the finding proper event weights are important to
₁₅₂₀ get the results without bias.

₁₅₂₁ One approach to get event averaged results, is set the all event weights as 1 (equal
₁₅₂₂ weights). For example, measure the flow coefficient(v_n) in given centrality, we measure
₁₅₂₃ v_n for each events, and calculate mean v_n as average of measured v_n with uniform
₁₅₂₄ weights(or materially no weights). But this approach is not correct in case of multi-
₁₅₂₅ particle correlations.

₁₅₂₆ In this analysis of $SC(m, n)$, the measurement performed in two procedure, first
₁₅₂₇ over all distinct particle quadruplets in an event, and then in the second step the single-
₁₅₂₈ event averages were weighted with "number of combinations" for correct event weight.

₁₅₂₉ To prove this, let's think a set of N events, where the multiplicity of each event is M_i
₁₅₃₀ where the i denote for i th event.

₁₅₃₁ Then the equation for 2-particle correlation Eq.3.3 can be written as like

$$\langle\langle 2 \rangle\rangle \equiv \frac{\sum_{i=1}^N \sum_{a,b=1}^{M_i} e^{in(\phi_{i,a} - \phi_{i,b})}}{\sum_{i=1}^N \sum_{a,b=1}^{M_i}} \quad (\text{B.1})$$

1532 with the constraints $a \neq b$. The equation B.1 implies that, we calculated every possi-
 1533 ble pairs of particle in an events and by using constraints, we eliminated all contributions
 1534 from self-correlations. If we take two distinct pairs of particles, one formed in event A
 1535 and another formed in event B, then the above definition ensures that these two distinct
 1536 pairs of particles will be taken into account at equal footing (i.e. a unit weight has being
 1537 assigned to each distinct pair of particles in any event in Eq.B.1). The denominator in
 1538 definition simply constant the total number of all such distinct pairs in all events. In
 1539 general form, for the definition of the i th event

$$\langle 2 \rangle_i \equiv \frac{\sum_{a,b=1}^{M_i} e^{in(\phi_{i,a} - \phi_{i,b})}}{\sum_{a,b=1}^{M_i}} \quad (\text{B.2})$$

1540

1541 And the total number the distinct pairs in the i th events will be evaluated as follows

$$\sum_{a,b=1}^{M_i} = \left(\sum_{a=1}^{M_i} \right) \left(\sum_{b=1}^{M_i} \right) - \sum_{a=b=1}^{M_i} = M_i^2 - M_i = M_i(M_i - 1) \quad (\text{B.3})$$

1542

1543 Extend to all event sets,

$$\langle\langle 2 \rangle\rangle = \frac{\sum_{i=1}^N \sum_{a,b=1}^{M_i} e^{in(\phi_{i,a} - \phi_{i,b})}}{\sum_{i=1}^N M_i(M_i - 1)} \quad (\text{B.4})$$

1544 and

$$\langle 2 \rangle_i \equiv \frac{\sum_{a,b=1}^{M_i} e^{in(\phi_{i,a} - \phi_{i,b})}}{M_i(M_i - 1)} \quad (\text{B.5})$$

1545 Then, we immediately get the following results by insert above equation to the orig-
 1546 inal Eq. B.1

$$\langle\langle 2 \rangle\rangle = \frac{\sum_{i=1}^N M_i(M_i - 1) \times \frac{\sum_{a,b=1}^{M_i} e^{in(\phi_{i,a} - \phi_{i,b})}}{M_i(M_i - 1)}}{\sum_{i=1}^N M_i(M_i - 1)} \quad (\text{B.6})$$

1547 and finally we get,

$$\langle\langle 2 \rangle\rangle = \frac{\sum_{i=1}^N M_i(M_i - 1) \times \langle 2 \rangle_i}{\sum_{i=1}^N M_i(M_i - 1)} \quad (\text{B.7})$$

1548 As seen in Eq. B.7, the event weight number of combinations has to be used to
1549 weight single event average $\langle 2 \rangle$ to obtain exactly the all event average $\langle\langle 2 \rangle\rangle$. The prof of
1550 4-particle correlation can be done in similar way.

₁₅₅₁ **Appendix C**

₁₅₅₂ **Jet energy loss as function of
₁₅₅₃ path-length**

₁₅₅₄ **C.1 Basic motivation**

₁₅₅₅ The nuclear modification factor, which is called R_{AA} , is one of the strong evidence
₁₅₅₆ of created medium in heavy ion collisions compare to $p+p$ collisions [129]. In Quantum
₁₅₅₇ Chromodynamics(QCD), the suppression of high p_T hadrons was predicted as the result
₁₅₅₈ of the energy loss of hard-scatters quarks and gluons in the hot and dense medium.

₁₅₅₉ **C.2 Analysis**

₁₅₆₀ **C.2.1 Inclusive R_{AA}**

₁₅₆₁ To compare heavy ion collisions to $p-p$ collision, the nuclear modification factor
₁₅₆₂ R_{AA} is defined.

$$R_{AA}(p_T) = \frac{(1/N_{AA}^{evt})dN^{AA}/dp_T}{\langle N_{coll} \rangle (1/N_{pp}^{evt})dN^{pp}/dp_T} \quad (\text{C.1})$$

₁₅₆₃

₁₅₆₄ where dN^{AA}/dp_T and dN^{pp}/dp_T are the yields in heavy ion collisions and $p-p$ col-
₁₅₆₅ lisions, respectively. $\langle N_{coll} \rangle$ is the average number of binary nucleon-nucleon collisions
₁₅₆₆ in one heavy ion collision event.

₁₅₆₇ Without medium effect, the nuclear modification factor R_{AA} should be 1. However,

1568 in heavy ion collision the nuclear modification factor is usually smaller than 1 [8, 45, 46].
 1569 These suppression for the high p_T hadrons can be explained by “jet quenching”, and this
 1570 is the one of probe for the existence of QGP medium. Compare with RHIC, LHC show
 1571 a stronger modification [8]. This indicate an enhanced energy loss and hence a denser
 1572 medium was produced at the LHC.

1573 C.2.2 Elliptic flow

1574 Anisotropic flow is the well known feature in both theoretical and experiment in
 1575 heavy ion collision. It provides the hints to understand collision evolution and thermal-
 1576 ization process. (See section.1.4 for the details)

$$\frac{dN}{d\Delta\phi} = \frac{x_0}{2\pi} + \frac{1}{2\pi} \sum_{n=1} (2v_n \cos n(\phi - \psi_n)) \quad (\text{C.2})$$

1577

1578 The function of $\frac{dN}{d\Delta\phi}$ shows the particle distribution in transverse direction. This
 1579 anisotropy particle production is known as flow effect. Especially, elliptical flow, which
 1580 is second order flow v_2 is well explained by almond shape initial geometry. But the
 1581 shape of the collision geometry is not a perfect almond shape because the collision nu-
 1582 cleon is not uniform sphere. Therefore, the created medium is not homogenous and has
 1583 complex shape. These are the reason of flow fluctuation and cause of higher order flow.
 1584 This higher order flow which comes from fluctuation and is not strongly affected by the
 1585 centrality of the collision. Because the distribution of the participating nucleons in col-
 1586 lision is totally random, so fluctuation is depends on event by event geometry and these
 1587 effect will be minimized in average over events.

1588 C.2.3 R_{AA} as function of $\Delta\phi$

As the nuclear modification factor represent the ratio of yield of particle produced in heavy ion and p - p collision, one can make R_{AA} as a function of p_T and $\Delta\phi$, where

$$\Delta\phi = \phi - \psi_n$$

1589 by using definition of flow. Since, the yield of p - p collision does not have reaction
 1590 plane, we can estimate the ratio of particle produced in ϕ angle is uniform over the event

1591 average. Therefore, the definition of R_{AA} as function of p_T and $\Delta\phi$ can be written as
 1592 [130, 131]

$$R_{AA}(p_T, \Delta\phi) = \frac{(1/N_{AA}^{evt})d^2N^{AA}/dp_T d\Delta\phi}{\langle N_{coll} \rangle (1/N_{pp}^{evt})dN^{pp}/dp_T} \quad (\text{C.3})$$

$$= R_{AA}(p_T) \frac{dN^{AA}}{d\Delta\phi} \quad (\text{C.4})$$

$$= R_{AA}(p_T)(1 + \sum_{n=1} (2v_n \cos n(\Delta\phi))) \quad (\text{C.5})$$

1593

1594 If we neglect high order flow which comes from fluctuations, above equation can be
 1595 simplified like

$$R_{AA}(p_T, \Delta\phi) \sim R_{AA}(p_T)(1 + 2v_2 \cos 2\Delta\phi) \quad (\text{C.6})$$

1596

1597 C.2.4 Path-length calculation with Glauber model

1598 If we assume all particles are produced from the center of collision region, then it
 1599 is possible to represent path-length as function of centrality and $\Delta\phi$ which is transverse
 1600 angle with respect to the reaction plane. To analyze the path-length dependence of R_{AA} ,
 1601 we estimate the path lengths of partons in the medium as the distance from the center
 1602 to the edge of the elliptical overlap zone of the heavy ion collision(See Fig.C.1). To
 1603 calculate this length, TGlauber Monte Carlo simulation has been used to evaluate for all
 1604 variations as function of impact parameter(centrality). of medium to the edge.

1605 However, in real situation, hard scattering happens in any collision point, also the
 1606 direction where the parton travels is random. One would calculate a weight factor for
 1607 the parton to travel into the divided region we set. In this case, proper path length is the
 1608 average value of length from the collision points to the edge of collision region for given
 1609 angle, such as

$$L(\Delta\phi) = \frac{\sum_{n=1}^N L_n(\Delta\phi)}{N} \quad (\text{C.7})$$

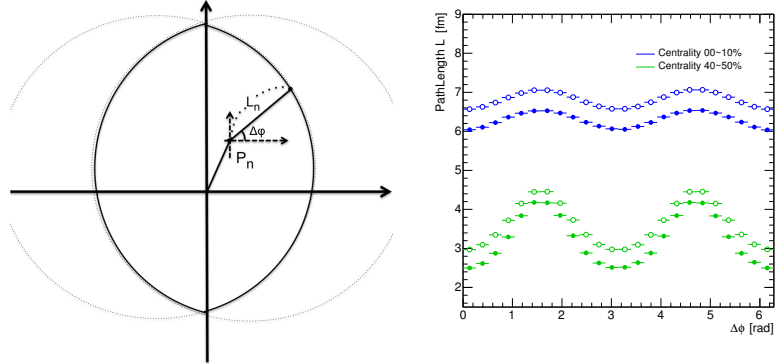


Figure C.1: Basic concept of definition of path-length for given angle $\Delta\phi$ (top), and results for centrality 00-10% and 40-50%(bottom). Open symbols are path-length which is calculated from Eq.C.7. Closed symbols are length from center to edge of region.

1610 where N is number of binary collisions, and $L_n(\Delta\phi)$ is length from n_{th} collision point(P_n
 1611 in Fig.C.1) to edge of collision shape for given angle $\Delta\phi$. This length is always longer
 1612 then length from center to edge of collision region.

1613 C.3 Result

1614 C.3.1 $R_{AA}(p_T, \Delta\phi)$

1615 For LHC experiment, the Nuclear modification factor, R_{AA} , of the Pb-Pb values
 1616 has been published by ALICE collaboration[132]. In Central collisions the field is most
 1617 suppressed with $R_{AA} \sim 0.13$ at $p_T = 6 \sim 7 \text{ GeV}/c$. Above $p_T > 7 \text{ GeV}/c$, there is
 1618 a significant rise in the nuclear modification factor for $p_T > 30 \text{ GeV}/c$. In peripheral
 1619 collisions, the suppression is weaker with $R_{AA} \sim 0.7$ and not much dependence of
 1620 p_T . Also the flow values v_n has been measured by CMS collaboration[133] up to $p_T =$
 1621 $20 \text{ GeV}/c$ for each centrality for same collision energy for Pb-Pb. They measured elliptic
 1622 flow(in terms of Fourier components of the azimuthal distribution, the $n=2$) with using
 1623 unidentified charged particles in $|\eta| < 2.4$. The anisotropic flow values are maximized
 1624 around intermediately $p_T \sim 4 \text{ GeV}/c$. To facilitate a quantitative comparison of there
 1625 result, the CMS measurements are fitted with a combination of a fifth-order polynomial

function (for $p_T < 4.2\text{GeV}/c$) and a Landau distribution (for $p_T > 4.2\text{GeV}/c$). The Results are shown in Fig.C.2, there is almost a factor of 2 or more suppression out-of-plane(where $\Delta\phi = \pi/2$) than in-plane($\Delta\phi = 0$) near $p_T = 3\text{GeV}/c$ in Centrality 20% to 30%. This suppression goes down when p_T moves higher. For RHIC experiment, the R_{AA} values as function of $\Delta\phi$ of neutral pion with respect to centrality in Au+Au collisions at $\sqrt{S_{NN}} = 200\text{GeV}$ has been Published by PHENIX collaboration. [134]

1632 C.3.2 Convert $\Delta\phi$ to path-length

1633 By using TGlauber simulation[135], for each Pb+Pb with collision energy 2.76TeV
1634 and Au+Au with collision energy 200GeV, the path length estimation has been done.
1635 To get average values of length between collision point to outside of shape, divide by 6
1636 bins(0~15, 15~30, 30~45, 45~60, 60~75, 75~90 degree) and find outermost wounded
1637 nucleon for each bins. Then histograms are filled with length from collision point to
1638 outermost nucleon and its transverse angle. The averaged values as path length for given
1639 angles are shown in Fig.C.3

1640 Based on Glauber simulations, there is no apparent path-length change in central
1641 collision. In peripheral regions, the path length has been changed more then 10% and,
1642 Path-length of out-of-plane is even longer then path-length of in-plane in more central
1643 collisions. For example, the path-length of out-of-plane in 30%~40% is approximately
1644 equal to the path-length of in-plane in 20%~30% centrality classes. The ALICE simula-
1645 tion result has always slightly longer path-length then PHENIX because of size of heavy
1646 ion species

1647 C.3.3 Path-length dependence of R_{AA}

1648 As a result, the R_{AA} values as function of $\Delta\phi$ are converted to as function of path
1649 length for each centralities. For given centrality, variation of $\Delta\phi$ gives a variation of the
1650 path length transversed for fixed initial conditions. Fig.C.4 shows the nuclear modifi-
1651 cation factor R_{AA} as a function of path-length for each p_T bins for LHC experiment.
1652 The results indicate that the suppression depends on the path-length for high p_T region
1653 particles. For the $p_T > 5\text{GeV}/cbins$, the slopes in the individual centralities are aligned

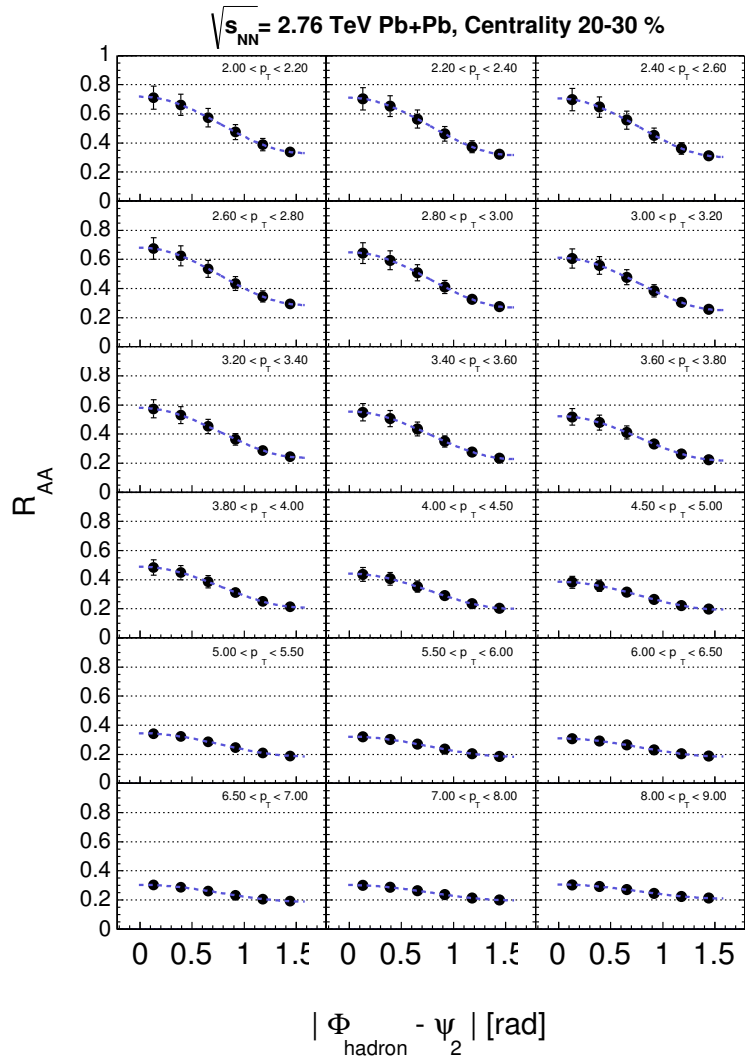


Figure C.2: R_{AA} versus $\Delta\phi$ for LHC experiment for given p_T bins. Statistical errors and systematical errors are evaluated quadratic.

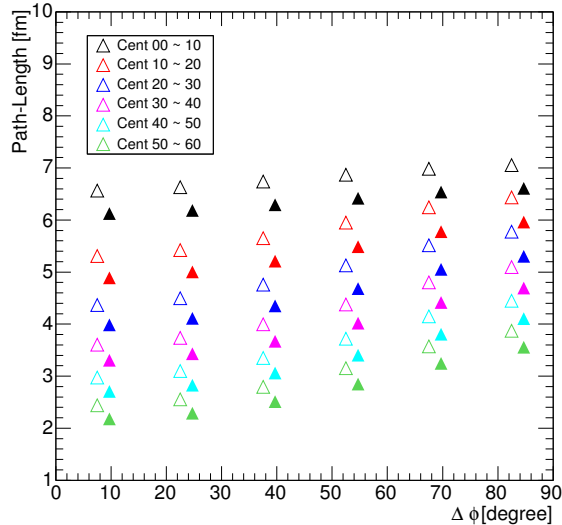


Figure C.3: Geometrical simulation result of path length calculation vs angle with respect to reaction plane by using TGlauber simulation for ALICE(open symbols) and PHENIX(closed symbols), plotted for the six centralities as shown in legend. The angle respect to reaction plane, $\Delta\phi$ is for the center of the bins(7.5, 22.5, 37.5, 52.5, 67.5 and 82.5) and centrality dependent offset is introduced for visual clarity

1654 together. And R_{AA} seems universal function with path length L for all centrality classed
 1655 for $p_T > 5GeV/c$ ranges within errors. To compare with PHENIX result, the same p_T
 1656 bin has been chosen and shows in Fig.C.5. Both result are fitted by following function

$$\frac{a}{a + L^n} \quad (C.8)$$

1657 where, a is arbitrary constant and L is path length. With this function we expect $R_{AA} = 1$
 1658 at path-length L = 0, and $R_{AA} = 0$ at path length $L = \infty$. For all centralities with more
 1659 then $p_T > 5GeV/c$, the function works well with $n \sim 2$ for both result.

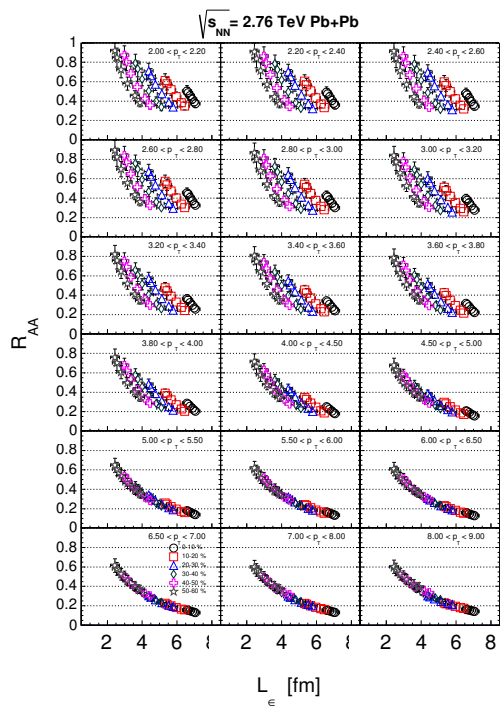


Figure C.4: R_{AA} versus Path-length correspond to $\Delta\phi$ for LHC experiment for given p_T bins. Statistical errors and systematical errors are evaluated quadratic.

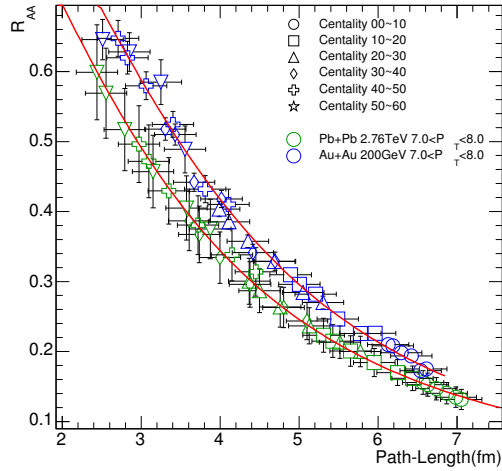


Figure C.5: Comparison of R_{AA} as function of path length for ALICE and PHENIX with $7\sim 8$ GeV/c p_T bin

1660 C.4 Summary

1661 One of the prediction of parton energy loss calculation is the average energy loss can
 1662 be represent as a function of the mean free path in medium. And energy loss in medium
 1663 can be indirectly evaluated from nuclear modification factor, R_{AA} . With combination
 1664 of using inclusive R_{AA} and flow, we can estimate the dependence of suppression on
 1665 geometry which related to mean free path length. we presented result of path-length
 1666 dependence of R_{AA} by using flow harmonics and calculation of path length from glauber
 1667 simulation. As the results, in high p_T ranges ($p_T > 5.0 \text{ GeV}/c$), the R_{AA} seems universal
 1668 function with path length. Moreover the decrease slope of R_{AA} as function of path-
 1669 length were well fitted by 2nd order inverse function.

¹⁶⁷⁰ **Appendix D**

¹⁶⁷¹ **Software and Data Information**

¹⁶⁷² **D.0.1 Software Information**

¹⁶⁷³ ROOT version v5-v34-36, AliROOT v5-08-15-1, AliPYHSICS vAN-20160801-1
¹⁶⁷⁴ are used for this analysis

¹⁶⁷⁵ **D.0.2 Data Information**

¹⁶⁷⁶ The list of good run number of LHC10h data are following:

¹⁶⁷⁷ **LHC10h data**

```
1678        runlist(Pb-Pb Data : LHC10h AOD086 (LHC10h_AOD86_MgFpMgFm runlist3))  
1679  
1680        139510, 139507, 139505, 139503, 139465, 139438, 139437, 139360, 139329, 139328,  
1681        139314, 139310, 139309, 139173, 139107, 139105, 139038, 139037, 139036, 139029,  
1682        139028, 138872, 138871, 138870, 138837, 138732, 138730, 138666, 138662, 138653,  
1683        138652, 138638, 138624, 138621, 138583, 138582, 138579, 138578, 138534, 138469,  
1684        138442, 138439, 138438, 138396, 138364, 138275, 138225, 138201, 138197, 138192,  
1685        138190, 137848, 137844, 137752, 137751, 137724, 137722, 137718, 137704, 137693,  
1686        137692, 137691, 137686, 137685, 137639, 137638, 137608, 137595, 137549, 137546,  
1687        137544, 137541, 137539, 137531, 137530, 137443, 137441, 137440, 137439, 137434,  
1688        137432, 137431, 137430, 137366, 137243, 137236, 137235, 137232, 137231, 137230,  
1689        137162, 137161, 137135
```

1690 **HIJING**

1691 HIJING_PbPb_LHC10h with minimum bias production (LHC11a10abis)

1692

1693 139510, 139507, 139505, 139503, 139465, 139438, 139437, 139360, 139329, 139328,
1694 139314, 139310, 139309, 139173, 139107, 139105, 139038, 139037, 139036, 139029,
1695 139028, 138872, 138871, 138870, 138837, 138732, 138730, 138666, 138662, 138653,
1696 138652, 138638, 138624, 138621, 138583, 138582, 138579, 138578, 138469, 138442,
1697 138439, 138438, 138396, 138364, 138275, 138225, 138201, 138197, 138192, 138190,
1698 137848, 137844, 137752, 137751, 137724, 137722, 137718, 137704, 137693, 137692,
1699 137691, 137686, 137685, 137639, 137638, 137608, 137595, 137549, 137544, 137541,
1700 137539, 137443, 137441, 137440, 137439, 137434, 137432, 137431, 137430, 137366,
1701 137243, 137236, 137235, 137232, 137231, 137230, 137162, 137161, 137135

1702 **AMPT**

1703 AMPT simulation for ALICE with different settings : AMPT13f3a, AMPT13f3b

1704 and AMPT13f3c.

1705

Setting	String Melting	Rescattering
AMPT13f3b (Default)	OFF	ON
AMPT13f3a (String melting)	ON	ON
AMPT13f3c (String melting w/o hadronic rescattering)	ON	OFF

Table D.1: List of AMPT datasets and configuration

1706 References

- 1707 [1] “Closing in on the border between primordial plasma and ordinary matter.”
- 1708 [2] R. Snellings, “Elliptic Flow: A Brief Review,” *New J. Phys.*, vol. 13, p. 055008,
1709 2011.
- 1710 [3] P. F. Kolb and U. W. Heinz, “Hydrodynamic description of ultrarelativistic heavy
1711 ion collisions,” 2003.
- 1712 [4] S. A. Voloshin, A. M. Poskanzer, and R. Snellings, “Collective phenomena in
1713 non-central nuclear collisions,” 2008.
- 1714 [5] M. L. Miller, K. Reygers, S. J. Sanders, and P. Steinberg, “Glauber modeling in
1715 high energy nuclear collisions,” *Ann. Rev. Nucl. Part. Sci.*, vol. 57, pp. 205–243,
1716 2007.
- 1717 [6] A. Bzdak, “Heavy ion collisions in the used nucleon model,” *Phys. Lett.*,
1718 vol. B647, pp. 358–360, 2007.
- 1719 [7] K. Aamodt *et al.*, “Elliptic flow of charged particles in Pb-Pb collisions at 2.76
1720 TeV,” *Phys. Rev. Lett.*, vol. 105, p. 252302, 2010.
- 1721 [8] G. Roland, K. Šafařík, and P. Steinberg, “Heavy-ion collisions at the {LHC},”
1722 *Progress in Particle and Nuclear Physics*, vol. 77, pp. 70 – 127, 2014.
- 1723 [9] G. Aad *et al.*, “Measurement of event-plane correlations in $\sqrt{s_{NN}} = 2.76$
1724 TeV lead-lead collisions with the ATLAS detector,” *Phys. Rev.*, vol. C90, no. 2,
1725 p. 024905, 2014.

- 1726 [10] S. Chatrchyan *et al.*, “Measurement of higher-order harmonic azimuthal
1727 anisotropy in PbPb collisions at $\sqrt{s_{NN}} = 2.76$ TeV,” *Phys. Rev.*, vol. C89, no. 4,
1728 p. 044906, 2014.
- 1729 [11] “Cern document server.”
- 1730 [12] “Aliroot documentation.”
- 1731 [13] H. Niemi, K. J. Eskola, and R. Paatelainen, “Event-by-event fluctuations in a
1732 perturbative QCD + saturation + hydrodynamics model: Determining QCD mat-
1733 ter shear viscosity in ultrarelativistic heavy-ion collisions,” *Phys. Rev.*, vol. C93,
1734 no. 2, p. 024907, 2016.
- 1735 [14] G. Giacalone, L. Yan, J. Noronha-Hostler, and J.-Y. Ollitrault, “Symmetric cu-
1736 mulants and event-plane correlations in Pb + Pb collisions,” *Phys. Rev.*, vol. C94,
1737 no. 1, p. 014906, 2016.
- 1738 [15] H. D. Politzer, “Reliable perturbative results for strong interactions?,” *Phys. Rev.*
1739 *Lett.*, vol. 30, pp. 1346–1349, Jun 1973.
- 1740 [16] D. J. Gross and F. Wilczek, “Ultraviolet behavior of non-abelian gauge theories,”
1741 *Phys. Rev. Lett.*, vol. 30, pp. 1343–1346, Jun 1973.
- 1742 [17] K. G. Wilson, “Confinement of quarks,” *Phys. Rev. D*, vol. 10, pp. 2445–2459,
1743 Oct 1974.
- 1744 [18] J. Adams *et al.*, “Experimental and theoretical challenges in the search for the
1745 quark gluon plasma: The STAR Collaboration’s critical assessment of the evi-
1746 dence from RHIC collisions,” *Nucl. Phys.*, vol. A757, pp. 102–183, 2005.
- 1747 [19] J. C. Collins and M. J. Perry, “Superdense matter: Neutrons or asymptotically
1748 free quarks?,” *Phys. Rev. Lett.*, vol. 34, pp. 1353–1356, May 1975.
- 1749 [20] N. Cabibbo and G. Parisi, “Exponential hadronic spectrum and quark liberation,”
1750 *Physics Letters B*, vol. 59, no. 1, pp. 67 – 69, 1975.
- 1751 [21] F. Karsch *PoSCPOD*, vol. 07, no. 026, (2007).

- 1752 [22] J. D. Bjorken, “Highly relativistic nucleus-nucleus collisions: The central rapidity
1753 region,” *Phys. Rev. D*, vol. 27, pp. 140–151, Jan 1983.
- 1754 [23] R. Rapp, B. Kämpfer, A. Andronic, D. Blaschke, C. Fuchs, M. Harada, T. Hilger,
1755 M. Kitazawa, T. Kunihiro, P. Petreczky, F. Riek, C. Sasaki, R. Thomas, L. To-
1756 los, P. Zhuang, H. van Hees, R. Vogt, and S. Zschocke, *In-Medium Excitations*,
1757 pp. 335–529. Berlin, Heidelberg: Springer Berlin Heidelberg, 2011.
- 1758 [24] C. Shen, U. Heinz, P. Huovinen, and H. Song, “Radial and elliptic flow in Pb+Pb
1759 collisions at the Large Hadron Collider from viscous hydrodynamic,” *Phys. Rev.*,
1760 vol. C84, p. 044903, 2011.
- 1761 [25] A. Bazavov *et al.*, “Equation of state in (2+1)-flavor QCD,” *Phys. Rev.*, vol. D90,
1762 p. 094503, 2014.
- 1763 [26] S. Voloshin and Y. Zhang, “Flow study in relativistic nuclear collisions by fourier
1764 expansion of azimuthal particle distributions,” *Zeitschrift für Physik C Particles
1765 and Fields*, vol. 70, no. 4, pp. 665–671, 1996.
- 1766 [27] K. H. Ackermann *et al.*, “Elliptic flow in Au + Au collisions at $(S(NN))^{**}(1/2) =$
1767 130 GeV,” *Phys. Rev. Lett.*, vol. 86, pp. 402–407, 2001.
- 1768 [28] J. Adam *et al.*, “Anisotropic flow of charged particles in Pb-Pb collisions at
1769 $\sqrt{s_{NN}} = 5.02 \text{ TeV}$,” *Phys. Rev. Lett.*, vol. 116, no. 13, p. 132302, 2016.
- 1770 [29] P. Romatschke and U. Romatschke, “Viscosity Information from Relativistic Nu-
1771 clear Collisions: How Perfect is the Fluid Observed at RHIC?,” *Phys. Rev. Lett.*,
1772 vol. 99, p. 172301, 2007.
- 1773 [30] B. Schenke, S. Jeon, and C. Gale, “Elliptic and triangular flows in 3 + 1D viscous
1774 hydrodynamics with fluctuating initial conditions,” *J. Phys.*, vol. G38, p. 124169,
1775 2011.
- 1776 [31] P. Bozek and I. Wyskiel-Piekarska, “Particle spectra in Pb-Pb collisions at
1777 $\sqrt{S_N N} = 2.76 \text{ TeV}$,” *Phys. Rev.*, vol. C85, p. 064915, 2012.

- 1778 [32] C. Gale, S. Jeon, B. Schenke, P. Tribedy, and R. Venugopalan, ‘‘Event-by-event
1779 anisotropic flow in heavy-ion collisions from combined Yang-Mills and viscous
1780 fluid dynamics,’’ *Phys. Rev. Lett.*, vol. 110, no. 1, p. 012302, 2013.
- 1781 [33] T. Hirano, P. Huovinen, and Y. Nara, ‘‘Elliptic flow in Pb+Pb collisions at
1782 $\sqrt{s_{NN}} = 2.76$ TeV: hybrid model assessment of the first data,’’ *Phys. Rev.*,
1783 vol. C84, p. 011901, 2011.
- 1784 [34] P. Kovtun, D. T. Son, and A. O. Starinets, ‘‘Viscosity in strongly interacting quan-
1785 tum field theories from black hole physics,’’ *Phys. Rev. Lett.*, vol. 94, p. 111601,
1786 2005.
- 1787 [35] R. A. Lacey, N. N. Ajitanand, J. M. Alexander, P. Chung, W. G. Holzmann, M. Is-
1788 sah, A. Taranenko, P. Danielewicz, and H. Stoecker, ‘‘Has the QCD Critical Point
1789 been Signaled by Observations at RHIC?,’’ *Phys. Rev. Lett.*, vol. 98, p. 092301,
1790 2007.
- 1791 [36] P. Danielewicz and M. Gyulassy, ‘‘Dissipative phenomena in quark-gluon plas-
1792 mas,’’ *Phys. Rev. D*, vol. 31, pp. 53–62, Jan 1985.
- 1793 [37] A. M. Poskanzer and S. A. Voloshin, ‘‘Methods for analyzing anisotropic flow in
1794 relativistic nuclear collisions,’’ *Phys. Rev. C*, vol. 58, pp. 1671–1678, Sep 1998.
- 1795 [38] M. Luzum and H. Petersen, ‘‘Initial State Fluctuations and Final State Correlations
1796 in Relativistic Heavy-Ion Collisions,’’ *J. Phys.*, vol. G41, p. 063102, 2014.
- 1797 [39] B. Alver *et al.*, ‘‘Importance of correlations and fluctuations on the initial source
1798 eccentricity in high-energy nucleus-nucleus collisions,’’ *Phys. Rev.*, vol. C77,
1799 p. 014906, 2008.
- 1800 [40] S. Wang, Y. Z. Jiang, Y. M. Liu, D. Keane, D. Beavis, S. Y. Chu, S. Y. Fung,
1801 M. Vient, C. Hartnack, and H. Stoecker, ‘‘Measurement of collective flow in heavy
1802 ion collisions using particle pair correlations,’’ *Phys. Rev.*, vol. C44, pp. 1091–
1803 1095, 1991.

- 1804 [41] M. B. Tsang, R. T. de Souza, Y.-d. Kim, D. R. Bowman, N. Carlin, C. K. Gelbke,
1805 W. G. Gong, W. G. Lynch, L. Phair, and F. Zhu, “Reaction plane determination for
1806 Ar-36 + Au-197 collisions at E/A=35 MeV,” *Phys. Rev.*, vol. C44, pp. 2065–2081,
1807 1991.
- 1808 [42] D. d’Enterria, “Jet quenching,” *Landolt-Bornstein*, vol. 23, p. 471, 2010.
- 1809 [43] X.-N. Wang and M. Gyulassy, “Gluon shadowing and jet quenching in A + A
1810 collisions at $\sqrt{s} = 200 \text{ GeV}$,” *Phys. Rev. Lett.*, vol. 68, pp. 1480–1483, Mar 1992.
- 1811 [44] M. Aggarwal et al., “Transverse mass distributions of neutral pions from pb-
1812 induced reactions at 158 gev,” *The European Physical Journal C - Particles and
1813 Fields*, vol. 23, no. 2, pp. 225–236, 2002.
- 1814 [45] A. e. a. Adare, “Suppression pattern of neutral pions at high transverse momentum
1815 in Au + Au collisions at $\sqrt{s_{NN}} = 200 \text{ GeV}$ and constraints on medium transport
1816 coefficients,” *Phys. Rev. Lett.*, vol. 101, p. 232301, Dec 2008.
- 1817 [46] J. a. e. Adams, “Transverse-momentum and collision-energy dependence of high-
1818 p_T hadron suppression in Au + Au collisions at ultrarelativistic energies,” *Phys.
1819 Rev. Lett.*, vol. 91, p. 172302, Oct 2003.
- 1820 [47] P. Christiansen, “Event-Shape Engineering and Jet Quenching,” *J. Phys. Conf.
1821 Ser.*, vol. 736, no. 1, p. 012023, 2016.
- 1822 [48] M. Miller and R. Snellings, “Eccentricity fluctuations and its possible effect on
1823 elliptic flow measurements,” 2003.
- 1824 [49] B. Alver *et al.*, “System size, energy, pseudorapidity, and centrality dependence
1825 of elliptic flow,” *Phys. Rev. Lett.*, vol. 98, p. 242302, 2007.
- 1826 [50] B. Alver and G. Roland, “Collision geometry fluctuations and triangular flow in
1827 heavy-ion collisions,” *Phys. Rev.*, vol. C81, p. 054905, 2010. [Erratum: *Phys.
1828 Rev.*C82,039903(2010)].

- 1829 [51] K. Aamodt *et al.*, “Higher harmonic anisotropic flow measurements of charged
1830 particles in Pb-Pb collisions at $\sqrt{s_{NN}}=2.76$ TeV,” *Phys. Rev. Lett.*, vol. 107,
1831 p. 032301, 2011.
- 1832 [52] M. Luzum and J.-Y. Ollitrault, “Extracting the shear viscosity of the quark-gluon
1833 plasma from flow in ultra-central heavy-ion collisions,” *Nucl. Phys.*, vol. A904-
1834 905, pp. 377c–380c, 2013.
- 1835 [53] T. Renk and H. Niemi, “Constraints from v_2 fluctuations for the initial-state ge-
1836 ometry of heavy-ion collisions,” *Phys. Rev.*, vol. C89, no. 6, p. 064907, 2014.
- 1837 [54] L. Yan, J.-Y. Ollitrault, and A. M. Poskanzer, “Azimuthal Anisotropy Distribu-
1838 tions in High-Energy Collisions,” *Phys. Lett.*, vol. B742, pp. 290–295, 2015.
- 1839 [55] C. Shen, S. A. Bass, T. Hirano, P. Huovinen, Z. Qiu, H. Song, and U. Heinz, “The
1840 QGP shear viscosity: Elusive goal or just around the corner?,” *J. Phys.*, vol. G38,
1841 p. 124045, 2011.
- 1842 [56] P. Bozek, “Flow and interferometry in 3+1 dimensional viscous hydrodynamics,”
1843 *Phys. Rev.*, vol. C85, p. 034901, 2012.
- 1844 [57] J.-B. Rose, J.-F. Paquet, G. S. Denicol, M. Luzum, B. Schenke, S. Jeon, and
1845 C. Gale, “Extracting the bulk viscosity of the quark?gluon plasma,” *Nucl. Phys.*,
1846 vol. A931, pp. 926–930, 2014.
- 1847 [58] S. Ryu, J. F. Paquet, C. Shen, G. S. Denicol, B. Schenke, S. Jeon, and C. Gale,
1848 “Importance of the Bulk Viscosity of QCD in Ultrarelativistic Heavy-Ion Colli-
1849 sions,” *Phys. Rev. Lett.*, vol. 115, no. 13, p. 132301, 2015.
- 1850 [59] D. Teaney and L. Yan, “Non linearities in the harmonic spectrum of heavy ion col-
1851 lisions with ideal and viscous hydrodynamics,” *Phys. Rev.*, vol. C86, p. 044908,
1852 2012.
- 1853 [60] L. V. Bravina, B. H. Brusheim Johansson, G. K. Eyyubova, V. L. Korotkikh, I. P.
1854 Lokhtin, L. V. Malinina, S. V. Petrushanko, A. M. Snigirev, and E. E. Zabrodin,

- 1855 “Hexagonal flow v6 as a superposition of elliptic v2 and triangular v3 flows,”
 1856 *Phys. Rev.*, vol. C89, no. 2, p. 024909, 2014.
- 1857 [61] M. Luzum and J.-Y. Ollitrault, “Constraining the viscous freeze-out distribution
 1858 function with data obtained at the BNL Relativistic Heavy Ion Collider (RHIC),”
 1859 *Phys. Rev.*, vol. C82, p. 014906, 2010.
- 1860 [62] H. Niemi, G. S. Denicol, H. Holopainen, and P. Huovinen, “Event-by-event distri-
 1861 butions of azimuthal asymmetries in ultrarelativistic heavy-ion collisions,” *Phys.*
 1862 *Rev. C*, vol. 87, p. 054901, May 2013.
- 1863 [63] A. Bilandzic, C. H. Christensen, K. Gulbrandsen, A. Hansen, and Y. Zhou,
 1864 “Generic framework for anisotropic flow analyses with multiparticle azimuthal
 1865 correlations,” *Phys. Rev. C*, vol. 89, p. 064904, Jun 2014.
- 1866 [64] J. Adam *et al.*, “Correlated event-by-event fluctuations of flow harmonics in Pb-
 1867 Pb collisions at $\sqrt{s_{\text{NN}}} = 2.76 \text{ TeV}$,” *Phys. Rev. Lett.*, vol. 117, p. 182301, 2016.
- 1868 [65] *The CERN Large Hadron Collider: Accelerator and Experiments, LHC Machine*.
 1869 JINST, 2008.
- 1870 [66] “Alice public web page.”
- 1871 [67] “Atlas public web pages.”
- 1872 [68] “Cms public web page.”
- 1873 [69] P. Cortese, C. W. Fabjan, L. Riccati, K. Safarík, and H. de Groot, *ALICE*
 1874 *physics performance: Technical Design Report*. Technical Design Report AL-
 1875 ICE, Geneva: CERN, 2005. revised version submitted on 2006-05-29 15:15:40.
- 1876 [70] F. Meddi, “The {ALICE} silicon pixel detector (spd),” *Nuclear Instruments and*
 1877 *Methods in Physics Research Section A: Accelerators, Spectrometers, Detectors*
 1878 *and Associated Equipment*, vol. 465, no. 1, pp. 40 – 45, 2001. {SPD2000}.
- 1879 [71] B. Alessandro *et al.*, “Charge collection in the Silicon Drift Detectors of the AL-
 1880 ICE experiment,” *JINST*, vol. 5, p. P02008, 2010.

- 1881 [72] G. Contin, “The ALICE Silicon Strip Detector performance during the first LHC
1882 data taking,” *Conf. Proc.*, vol. C100901, pp. 257–260, 2010.
- 1883 [73] G. Contin, *The Silicon Strip Detector (SSD) for the ALICE experiment at LHC: construction, characterization and charged particles multiplicity studies*. PhD
1884 thesis, Trieste U., 2009.
- 1885 [74] “Upgrade of the ALICE Time Projection Chamber,” Tech. Rep. CERN-LHCC-
1886 2013-020. ALICE-TDR-016, Oct 2013.
- 1887 [75] A. Collaboration, “Performance of the alice vzero system,” *arXiv preprint arXiv:1306.3130*, 2013.
- 1888 [76] P. Cortese, *ALICE transition-radiation detector: Technical Design Report*. Technical
1889 Design Report ALICE, Geneva: CERN, 2001.
- 1890 [77] A. Alici, A. Collaboration, *et al.*, “The mrpc-based alice time-of-flight detector:
1891 status and performance,” *Nuclear Instruments and Methods in Physics Research Section A: Accelerators, Spectrometers, Detectors and Associated Equipment*,
1892 vol. 706, pp. 29–32, 2013.
- 1893 [78] L. Molnar, “The ALICE HMPID detector ready for collisions at the LHC,” *Nucl.
1894 Instrum. Meth.*, vol. A595, pp. 27–30, 2008.
- 1895 [79] H. Torii and the ALICE-PHOS Collaborations, “The alice phos calorimeter,”
1896 *Journal of Physics: Conference Series*, vol. 160, no. 1, p. 012045, 2009.
- 1897 [80] R. B. for the ALICE EMCAL Collaboration *et al.*, “Alice emcal physics perfor-
1898 mance report,” *arXiv preprint arXiv:1008.0413*, 2010.
- 1899 [81] P. Cortese, V. Chambert, R. Simon, J. Contreras, P. Van de Vyvre, A. Di Bar-
1900 tolomeo, V. Petrov, A. De Haas, F. Navach, A. Kolojvari, *et al.*, “Alice forward
1901 detectors: Fmd, to and vo,” tech. rep., ALICE-TDR-011, 2004.
- 1902 [82] C. Oppedisano, R. Arnaldi, E. Chiavassa, C. Cicalò, P. Cortese, A. De Falco,
1903 G. Dellacasa, N. De Marco, A. Ferretti, M. Floris, *et al.*, “Physics performance of
1904

- 1907 the alice zero degree calorimeter,” *Nuclear Physics B-Proceedings Supplements*,
 1908 vol. 197, no. 1, pp. 206–210, 2009.
- 1909 [83] D. Adamová, J. Chudoba, T. Kouba, P. M. Lorenzo, P. Saiz, J. Švec, and J. Hampl,
 1910 “Status of the grid computing for the alice experiment in the czech republic,”
 1911 *Journal of Physics: Conference Series*, vol. 219, no. 7, p. 072023, 2010.
- 1912 [84] K. Aamodt *et al.*, “The ALICE experiment at the CERN LHC,” *JINST*, vol. 3,
 1913 p. S08002, 2008.
- 1914 [85] P. Cortese *et al.*, “ALICE: Physics performance report, volume I,” *J. Phys.*,
 1915 vol. G30, pp. 1517–1763, 2004.
- 1916 [86] P. Cortese *et al.*, “ALICE: Physics performance report, volume II,” *J. Phys.*,
 1917 vol. G32, pp. 1295–2040, 2006.
- 1918 [87] K. Aamodt *et al.*, “Centrality dependence of the charged-particle multiplicity den-
 1919 sity at mid-rapidity in Pb-Pb collisions at $\sqrt{s_{NN}} = 2.76$ TeV,” *Phys. Rev. Lett.*,
 1920 vol. 106, p. 032301, 2011.
- 1921 [88] X.-N. Wang and M. Gyulassy, “HIJING: A Monte Carlo model for multiple jet
 1922 production in p p, p A and A A collisions,” *Phys. Rev.*, vol. D44, pp. 3501–3516,
 1923 1991.
- 1924 [89] “GEANT Detector Description and Simulation Tool,” 1994.
- 1925 [90] H. Niemi, G. S. Denicol, H. Holopainen, and P. Huovinen, “Event-by-event distri-
 1926 butions of azimuthal asymmetries in ultrarelativistic heavy-ion collisions,” *Phys.*
 1927 *Rev.*, vol. C87, no. 5, p. 054901, 2013.
- 1928 [91] A. Bilandzic, C. H. Christensen, K. Gulbrandsen, A. Hansen, and Y. Zhou,
 1929 “Generic framework for anisotropic flow analyses with multiparticle azimuthal
 1930 correlations,” *Phys. Rev.*, vol. C89, no. 6, p. 064904, 2014.
- 1931 [92] A. Adare *et al.*, “Measurements of Higher-Order Flow Harmonics in Au+Au Col-
 1932 lisions at $\sqrt{s_{NN}} = 200$ GeV,” *Phys. Rev. Lett.*, vol. 107, p. 252301, 2011.

- 1933 [93] G. Aad *et al.*, “Measurement with the ATLAS detector of multi-particle azimuthal
 1934 correlations in p+Pb collisions at $\sqrt{s_{NN}} = 5.02$ TeV,” *Phys. Lett.*, vol. B725,
 1935 pp. 60–78, 2013.
- 1936 [94] B. B. Abelev *et al.*, “Multiparticle azimuthal correlations in p -Pb and Pb-Pb colli-
 1937 sions at the CERN Large Hadron Collider,” *Phys. Rev.*, vol. C90, no. 5, p. 054901,
 1938 2014.
- 1939 [95] V. Khachatryan *et al.*, “Evidence for Collective Multiparticle Correlations in p-Pb
 1940 Collisions,” *Phys. Rev. Lett.*, vol. 115, no. 1, p. 012301, 2015.
- 1941 [96] L. Adamczyk *et al.*, “Long-range pseudorapidity dihadron correlations in d+Au
 1942 collisions at $\sqrt{s_{NN}} = 200$ GeV,” *Phys. Lett.*, vol. B747, pp. 265–271, 2015.
- 1943 [97] A. Adare *et al.*, “Measurements of elliptic and triangular flow in high-multiplicity
 1944 $^3\text{He}+\text{Au}$ collisions at $\sqrt{s_{NN}} = 200$ GeV,” *Phys. Rev. Lett.*, vol. 115, no. 14,
 1945 p. 142301, 2015.
- 1946 [98] C. Loizides, “Experimental overview on small collision systems at the LHC,”
 1947 in *Proceedings, 25th International Conference on Ultra-Relativistic Nucleus-
 1948 Nucleus Collisions (Quark Matter 2015): Kobe, Japan, September 27-October
 1949 3, 2015*, 2016.
- 1950 [99] R. S. . Bhalerao, J.-Y. Ollitrault, and S. Pal, “Characterizing flow fluctuations with
 1951 moments,” *Physics Letters B*, vol. 742, pp. 94–98, Mar. 2015.
- 1952 [100] M. Gyulassy and X.-N. Wang, “HIJING 1.0: A Monte Carlo program for parton
 1953 and particle production in high-energy hadronic and nuclear collisions,” *Comput.
 1954 Phys. Commun.*, vol. 83, p. 307, 1994.
- 1955 [101] X.-N. Wang and M. Gyulassy, “hijing: A monte carlo model for multiple jet pro-
 1956 duction in pp, pA, and AA collisions,” *Phys. Rev. D*, vol. 44, pp. 3501–3516, Dec
 1957 1991.

- 1958 [102] N. Borghini, P. M. Dinh, and J.-Y. Ollitrault, “A New method for measuring azimuthal distributions in nucleus-nucleus collisions,” *Phys. Rev.*, vol. C63,
 1959
 1960 p. 054906, 2001.
- 1961 [103] R. Paatelainen, K. J. Eskola, H. Holopainen, and K. Tuominen, “Multiplicities and
 1962 p_T spectra in ultrarelativistic heavy ion collisions from a next-to-leading order
 1963 improved perturbative QCD + saturation + hydrodynamics model,” *Phys. Rev.*,
 1964 vol. C87, no. 4, p. 044904, 2013.
- 1965 [104] R. Paatelainen, K. J. Eskola, H. Niemi, and K. Tuominen, “Fluid dynamics with
 1966 saturated minijet initial conditions in ultrarelativistic heavy-ion collisions,” *Phys.*
 1967 *Lett.*, vol. B731, pp. 126–130, 2014.
- 1968 [105] K. J. Eskola, H. Niemi, and R. Paatelainen, “Pinning down QCD-matter shear vis-
 1969 cosity in ultrarelativistic heavy-ion collisions via EbyE fluctuations using pQCD
 1970 + saturation + hydrodynamics,” in *Proceedings, 7th International Conference*
 1971 *on Hard and Electromagnetic Probes of High-Energy Nuclear Collisions (Hard*
 1972 *Probes 2015): Montréal, Québec, Canada, June 29-July 3, 2015*, 2016.
- 1973 [106] B. Zhang, C. M. Ko, B.-A. Li, and Z.-w. Lin, “A multiphase transport model for
 1974 nuclear collisions at RHIC,” *Phys. Rev.*, vol. C61, p. 067901, 2000.
- 1975 [107] Z.-w. Lin, S. Pal, C. M. Ko, B.-A. Li, and B. Zhang, “Charged particle rapidity
 1976 distributions at relativistic energies,” *Phys. Rev.*, vol. C64, p. 011902, 2001.
- 1977 [108] Z.-W. Lin, C. M. Ko, B.-A. Li, B. Zhang, and S. Pal, “A Multi-phase transport
 1978 model for relativistic heavy ion collisions,” *Phys. Rev.*, vol. C72, p. 064901, 2005.
- 1979 [109] B. Andersson, G. Gustafson, and B. Nilsson-Almqvist, “A Model for Low p(t)
 1980 Hadronic Reactions, with Generalizations to Hadron - Nucleus and Nucleus-
 1981 Nucleus Collisions,” *Nucl. Phys.*, vol. B281, pp. 289–309, 1987.
- 1982 [110] B. Nilsson-Almqvist and E. Stenlund, “Interactions Between Hadrons and Nuclei:
 1983 The Lund Monte Carlo, Fritiof Version 1.6,” *Comput. Phys. Commun.*, vol. 43,
 1984 p. 387, 1987.

- 1985 [111] B. Zhang, “ZPC 1.0.1: A Parton cascade for ultrarelativistic heavy ion collisions,”
 1986 *Comput. Phys. Commun.*, vol. 109, pp. 193–206, 1998.
- 1987 [112] Z.-W. Lin, C. M. Ko, B.-A. Li, B. Zhang, and S. Pal, “Multiphase transport model
 1988 for relativistic heavy ion collisions,” *Physical Review C*, vol. 72, pp. 064901–29,
 1989 Dec. 2005.
- 1990 [113] B. Li, A. T. Sustich, B. Zhang, and C. M. Ko, “Studies of superdense hadronic
 1991 matter in a relativistic transport model,” *Int. J. Mod. Phys.*, vol. E10, pp. 267–352,
 1992 2001.
- 1993 [114] Z.-w. Lin and C. M. Ko, “Partonic effects on the elliptic flow at RHIC,” *Phys.
 1994 Rev.*, vol. C65, p. 034904, 2002.
- 1995 [115] Z.-W. Lin, “Evolution of transverse flow and effective temperatures in the parton
 1996 phase from a multi-phase transport model,” *Phys. Rev.*, vol. C90, no. 1, p. 014904,
 1997 2014.
- 1998 [116] J. Adam *et al.*, “Higher harmonic flow coefficients of identified hadrons in Pb-Pb
 1999 collisions at $\sqrt{s_{\text{NN}}} = 2.76 \text{ TeV}$,” *JHEP*, vol. 09, p. 164, 2016.
- 2000 [117] X. Zhu, Y. Zhou, H. Xu, and H. Song, “Correlations of flow harmonics in 2.76A
 2001 TeV Pb–Pb collisions,” 2016.
- 2002 [118] H.-j. Xu, Z. Li, and H. Song, “High-order flow harmonics of identified hadrons in
 2003 2.76A TeV Pb + Pb collisions,” *Phys. Rev.*, vol. C93, no. 6, p. 064905, 2016.
- 2004 [119] R. S. Bhalerao, A. Jaiswal, and S. Pal, “Collective flow in event-by-event par-
 2005 tonic transport plus hydrodynamics hybrid approach,” *Phys. Rev.*, vol. C92, no. 1,
 2006 p. 014903, 2015.
- 2007 [120] L. Pang, Q. Wang, and X.-N. Wang, “Effects of initial flow velocity fluctuation in
 2008 event-by-event (3+1)D hydrodynamics,” *Phys. Rev.*, vol. C86, p. 024911, 2012.
- 2009 [121] Z. Qiu, C. Shen, and U. Heinz, “Hydrodynamic elliptic and triangular flow in
 2010 Pb-Pb collisions at $\sqrt{s} = 2.76 \text{ ATeV}$,” *Phys. Lett.*, vol. B707, pp. 151–155, 2012.

- 2011 [122] C. Shen, U. Heinz, P. Huovinen, and H. Song, “Systematic parameter study
2012 of hadron spectra and elliptic flow from viscous hydrodynamic simulations of
2013 Au+Au collisions at $\sqrt{s_{NN}} = 200$ GeV,” *Phys. Rev.*, vol. C82, p. 054904, 2010.
- 2014 [123] P. F. Kolb, J. Sollfrank, and U. W. Heinz, “Anisotropic transverse flow and the
2015 quark hadron phase transition,” *Phys. Rev.*, vol. C62, p. 054909, 2000.
- 2016 [124] D. Kharzeev and M. Nardi, “Hadron production in nuclear collisions at RHIC and
2017 high density QCD,” *Phys. Lett.*, vol. B507, pp. 121–128, 2001.
- 2018 [125] H. J. Drescher and Y. Nara, “Effects of fluctuations on the initial eccentricity
2019 from the Color Glass Condensate in heavy ion collisions,” *Phys. Rev.*, vol. C75,
2020 p. 034905, 2007.
- 2021 [126] T. Hirano and Y. Nara, “Eccentricity fluctuation effects on elliptic flow in rela-
2022 tivistic heavy ion collisions,” *Phys. Rev.*, vol. C79, p. 064904, 2009.
- 2023 [127] F. G. Gardim, F. Grassi, M. Luzum, and J.-Y. Ollitrault, “Mapping the hydro-
2024 dynamic response to the initial geometry in heavy-ion collisions,” *Phys. Rev. C*,
2025 vol. 85, p. 024908, Feb 2012.
- 2026 [128] L. Yan and J.-Y. Ollitrault, “ v_4, v_5, v_6, v_7 : nonlinear hydrodynamic response
2027 versus LHC data,” *arXiv.org*, pp. 82–87, Feb. 2015.
- 2028 [129] K. Adcox *et al.*, “Suppression of hadrons with large transverse momentum in cen-
2029 tral Au+Au collisions at $\sqrt{s_{NN}} = 130$ -GeV,” *Phys. Rev. Lett.*, vol. 88, p. 022301,
2030 2002.
- 2031 [130] J. Liao and V. Koch, “Exposing the non-collectivity in elliptic flow,” *Phys. Rev.*
2032 *Lett.*, vol. 103, p. 042302, 2009.
- 2033 [131] S. Adler *et al.*, “A Detailed Study of High-p(T) Neutral Pion Suppression and Az-
2034 imuthal Anisotropy in Au+Au Collisions at $s(\text{NN})^{**}(1/2) = 200$ -GeV,” *Phys. Rev.*,
2035 vol. C76, p. 034904, 2007.

- 2036 [132] B. Abelev *et al.*, ‘‘Centrality Dependence of Charged Particle Production at Large
2037 Transverse Momentum in Pb–Pb Collisions at $\sqrt{s_{NN}} = 2.76$ TeV,’’ *Phys.Lett.*,
2038 vol. B720, pp. 52–62, 2013.
- 2039 [133] S. Chatrchyan *et al.*, ‘‘Measurement of the elliptic anisotropy of charged parti-
2040 cles produced in PbPb collisions at nucleon-nucleon center-of-mass energy = 2.76
2041 TeV,’’ *Phys.Rev.*, vol. C87, p. 014902, 2013.
- 2042 [134] A. Adare *et al.*, ‘‘Neutral pion production with respect to centrality and reac-
2043 tion plane in Au+Au collisions at $\sqrt{s_{NN}}=200$ GeV,’’ *Phys.Rev.*, vol. C87, no. 3,
2044 p. 034911, 2013.
- 2045 [135] B. Alver, M. Baker, C. Loizides, and P. Steinberg, ‘‘The PHOBOS Glauber Monte
2046 Carlo,’’ 2008.